

In Vitro and In Vivo Analysis of DGC-specific RHOA Mutations on Tumor Development

January 2020

Takashi NISHIZAWA

In Vitro and In Vivo Analysis of DGC-specific RHOA Mutations on Tumor Development

A Dissertation Submitted to

the Graduate School of Life and Environmental Sciences,

the University of Tsukuba

in Partial Fulfillment of the Requirements

for the Degree of Doctor of Philosophy in Biological Science

(Doctoral Program in Biological Sciences)

Takashi NISHIZAWA

Table of Contents

Abstract	5
Abbreviations.....	10
General Introduction.....	14
Chapter 1: DGC-specific RHOA mutations maintained cancer cell survival and promoted cell migration via ROCK inactivation	
Abstract	22
Introduction.....	24
Materials and Methods.....	26
Results.....	32
Discussion.....	38
Tables and Figures.....	42
Chapter 2: Difference in morphology and interactome profiles between orthotopic and subcutaneous gastric cancer xenograft models	
Abstract	67

Introduction.....	68
Materials and Methods.....	70
Results and Discussion.....	75
Tables and Figures.....	80
Chapter 3: In vivo effects of mutant RHOA on tumor formation in an orthotopic inoculation model	
Abstract	88
Introduction.....	90
Materials and Methods.....	93
Results.....	100
Discussion.....	105
Tables and Figures.....	109
General Discussion.....	135
Acknowledgements.....	142
References.....	144

Abstract

Diffuse type gastric cancer (DGC) is one of the cancers that have the highest unmet medical needs. *Ras homolog family member A (RHOA)* missense mutations exist specifically in DGC but not intestinal type gastric cancer (IGC). Therefore, mutated *RHOAs* are considered as one of the DGC driver genes, but it is not fully understood how *RHOA* mutations contribute to DGC development. To solve this problem, I evaluated *in vitro* and *in vivo* function of *RHOA* mutations for DGC development.

Firstly, I examined how *RHOA* mutations affect cancer cell survival and cell motility *in vitro*. When I knocked down the expression of *RHOA* in various *RHOA* mutated cancer cell lines, several cancer cells showed remarkable cell death. Interestingly, the downregulation of mutated *RHOAs* induced ROCK signaling activation through the feedback upregulation of *RHOB*. Next, I introduced several *RHOA* mutations in *RHOA* wild type (WT) gastric cancer cell line to evaluate cell motility. Mutated-*RHOAs* promoted cell migration decreasing the stress fiber formation, that is a major event following ROCK signaling activation, but not cell invasion. These results indicated that *RHOA* mutations contributed cell survival and cell migration by keeping ROCK inactive. The fusion proteins of CLDN18 and ARHGAP (CLGs) are known to be mutually exclusive to *RHOA* mutations in DGC, therefore I evaluated the relationship between CLGs and RHO-ROCK signaling. I revealed that *CLGs* contributed cell survival and also cell migration via GAP domain, that is a functional domain to promote RHO proteins to inactive form. I summarized a series of evidence for the mechanism related cell survival and migration induced by *RHOA* mutations and *CLG* fusions in Figure 0-1. These findings

show that the inactivation of ROCK would be a key step in DGC development.

Secondly, I established *in vivo* model to evaluate the contribution of *RHOA* mutations for tumor development. I attempted to characterize the biological difference between subcutaneous (SC) and orthotopic (ORT) models of the *RHOA*-mutated gastric cancer cell line OE19 by pathological analysis and CASTIN (CAncer-STromal INteractome) analysis, which is a novel method developed to analyze the tumor-stroma interactome framework. Histopathologically, the SC tumors were well circumscribed from the adjacent tissue, with scant stroma and the formation of large ductal structures. In contrast, the ORT tumors were less circumscribed, with small ductal structures invading into abundant stroma. With CASTIN analysis, I successfully identified several interactions that are known to affect the tumor microenvironment as being selectively enhanced in the ORT model. The pathological analysis and CASTIN analysis revealed that ORT models have a more invasive character and enhanced interaction with stromal cells compared with SC models, therefore, ORT model would be suitable *in vivo* DGC model for the functional evaluation of *RHOA* mutations.

Finally, I examined the contribution of *RHOA* mutations to DGC development using the ORT model of the gastric cancer cell line MKN74, in which wild type (WT)- or mutated (Y42C and Y42S)-*RHOA* had been introduced. When I confirmed the ROCK signaling in tumor with RNA sequencing, the gene set related to ROCK signaling inhibition was enriched in the *RHOA*-mutated group as well as *in vitro*. Also, inflammation- and hypoxia-related pathways were enriched in

mock/WT, however cell metabolism- and cell cycle-related pathways were enriched in Y42C/Y42S. Next, I conducted histopathological analysis to evaluate the relationship between the enriched pathways and tumor histology, and also the similarity between mouse model and clinical DGC. I revealed that small tumor nests were more frequent in *RHOA* mutants than in mock or WT. In addition, increased blood vessel formation and infiltration of macrophages within the tumor mass were observed in *RHOA* mutants. Furthermore, unlike mock/WT, the *RHOA*-mutated tumor cells had little antitumor host reaction in the invasive front, which is similar to the pattern of mucosal invasion in clinical *RHOA*-mutated DGC. A series of futures in *RHOA*-mutated group showed the partial similarity of clinical DGCs. Therefore, mutated *RHOA* functionally contributed to the acquisition of DGC features.

A series of evidence will accelerate understanding of the contribution of *RHOA* mutations in DGC biology and the development of further therapeutics.

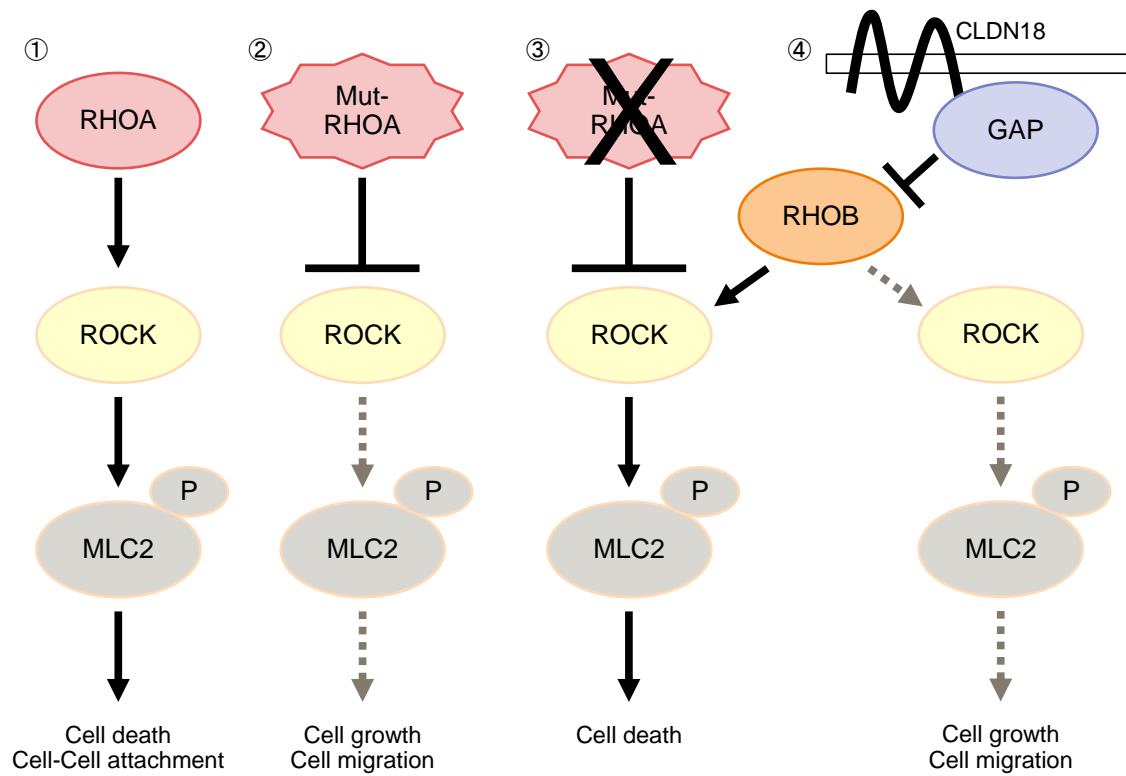


Figure 0-1: The summary of *in vitro* signal mechanism in *RHOA* mutants

The illustration of the *in vitro* signaling mechanism in WT (1), mutated-*RHOAs* (2), mutated-*RHOAs* after knockdown (3) and *CLG* fusions (4).

Abbreviations

ACTB	Beta-actin
AITL	angio-immunoblastic T-cell lymphoma
ATCC	American Type Culture Collection
ATL	adult T-cell leukemia-lymphoma
CAF	cancer associated fibroblasts
CASTIN	CAnker-STromal INteractome
CFL1	Cofilin-1
CLDN	Claudin
CLG	CLDN18-ARHGAP
DEGs	differentially expressed genes
DGC	diffuse type gastric cancers
DLBCL	diffuse large B-cell lymphoma
ECACC	European Collection of Animal Cell Cultures
ECM	extracellular matrix
EMT	epithelial-mesenchymal transition
ES	enrichment score
FDA	Food and Drug Administration
GAP	GTPase-activating protein

GEF	guanine nucleotide exchange factor
GSEA	Gene Set Enrichment Analysis
HE	hematoxylin and eosin
IGC	intestinal gastric cancer
JCRB	Japanese Collection of Research Bioresources
KCLB	Korean Cell Line Bank
KEGG	Kyoto Encyclopedia of Genes and Genomes
LIMK	LIM domain kinase
LoF	loss-of-function
MAPK	Mitogen-activated Protein Kinase
MLC2	Myosin regulatory light chain 2
MYPT1	myosin phosphatase targeting subunit 1
NES	normalized enrichment score
NGS	Next generation sequencing
n.s.	no significant difference
ORT	orthotopic
PPI	protein-protein interaction
PTCL-NOS	peripheral T-cell lymphoma not otherwise specified

RHOA	Ras homolog family member A
RHO-GDI	RHO GDP-dissociation inhibitor
ROCK	Rho-associated protein kinase
SC	subcutaneous
SCID	severe combined immune- deficient
TCGA	The Cancer Genome Atlas
TM	transmembrane
WT	wild type.

General Introduction

According to the investigation of the World Health Organization, cancer is the major cause of death in worldwide countries [1]. Based on the report of Cancer Statics in Japan 2017 [2], cancer is also the leading cause of death in Japan for more than 30 years, and mortality rate is further increasing year by year. The mortality is cancer type dependent, but gastric cancer is second mortality in male following lung cancer, and forth in female [2]. Therefore, the development of effective drug for gastric cancer is earnestly desired.

Cancer is known as a disease of gene. Cancer cells arises from the transformation of normal cells through the accumulation of genetic alterations like mutations and fusions. Genetic alterations are induced by various carcinogens. The risk of carcinogens is evaluated and reported by the International Agency for Research on Cancer [3], and carcinogens are roughly categorized in 3 groups. First group is the physical carcinogens, such as ultraviolet and radiation [4-6]. Second group is the chemical carcinogens, such as asbestos and components of cigarette smoke like nitrosamines and so on [7-10]. Third group is the biological carcinogens, such as infections from certain viruses or bacteria [11-13]. One of major carcinogens of gastric cancer is *Helicobacter pylori* infection [14, 15], and other carcinogens such as alcohol consumption and smoking are also reported [16-18]. These carcinogens injure normal genes, and some of injured genes contribute cancer developments through mainly classified into two patterns [19-22]. One is oncogenes that accelerate abnormal cell growth. Well known oncogenes are *KRAS*, *BRAF*, *PIK3CA*, *HER2*, *EGFR* and *ALK*. The other is tumor suppressor

genes that repress cell growth and induce apoptosis. *TP53*, *PTEN* and *RB* are representatives of tumor suppressor genes. It is reported that either or both overactivation of oncogenes and inactivation of tumor suppressor genes induce cancer development. Therefore, the identification of disease specific oncogenes or tumor suppressor genes are quite important to reveal the mechanism of tumorigenesis and the development of future therapeutics which target the genetic features.

Molecular target agents are drugs that target cancer specific molecules involved in the growth and spread of cancer cells. Food and Drug Administration (FDA) approved molecular target agents in gastric cancer are only three in Sep 2019. First is Trastuzumab, which is a humanized monoclonal antibody to the HER2 receptor [23-25]. Second is Ramucirumab, which is a monoclonal antibody that binds to the VEGFR2 [23, 26-28]. Third is Pembrolizumab, which is a humanized monoclonal antibody that targets for the PD1 [29-31]. Because these target genes are amplified or overexpressed in gastric cancer, it would be effective to focus on genetic alteration or transcriptome abnormality to identify novel target genes. Trastuzumab, Ramucirumab and Pembrolizumab prolonged overall survival of gastric cancer patients, however the five years survival rate of gastric cancer in US is only 31.5% [32], so the unmet medical needs of gastric cancer are still high.

Gastric cancer has two main histologic subtypes, intestinal gastric cancer (IGC) and diffuse gastric cancer (DGC), as classified by Lauren [33]. The relative frequencies are approximately 54% for IGC, 32% for DGC, and 15% for the mix type [34]. WHO also classified gastric cancer into four

major histologic patterns: tubular, papillary, mucinous and poorly cohesive including signet ring cell carcinoma [35]. Compared with Lauren and WHO, tubular and papillary type are mainly included in IGC, and DGC covers mucinous and poorly cohesive types [36]. It is indicated that IGC is a well differentiated type carcinoma, and DGC has poorly differentiated features. DGC is common in younger patients and shows worse prognosis than IGC [33, 37]. IGC is more often associated with *Helicobacter pylori* infection, but less in DGC [38]. Moreover, the rate of HER2 positivity is much lower than IGC [39], it means that the DGC patients are less applicable to Trastuzumab. Therefore, DGC is one of the cancers that have the highest unmet medical needs.

Next generation sequencing (NGS) is effective methods to identify novel genomic or transcriptomic abnormality because it is possible to conduct comprehensive screening simultaneously. Actually, novel oncogenes or tumor suppressor genes has been identified with NGS [40-42]. The comprehensive analysis focus on DGC was not reported in 2014, so I collected 87 DGC patients and conducted genomic screening. As a result, Kakiuchi et al. identified novel DGC specific missense mutation in *Ras homolog family member A (RHOA)* gene [43]. Other groups also reported that frequent *RHOA* mutation were observed in DGC [44, 45]. Around the same periods, it was reported that *RHOA* was more often mutated in hematopoietic cancers such as angio-immunoblastic T-cell lymphoma (AITL) and peripheral T-cell lymphoma not otherwise specified (PTCL-NOS) [46-50]. A series of evidence indicated that mutated *RHOA* might be the novel target gene in some type of cancers

including DGC.

RHOA is a member of RAS GTPase super family, which comprise over 150 members in human [51]. RHOA is only 22 kDa small monomeric G protein and shows high homology with RHOB and RHOC: 85% amino acid sequence identity each [52-53]. RHOA exhibit high-affinity binding for GDP and GTP. When bound to GTP, RHOA can bind to effector proteins and modulate cell behavior and cell morphology, therefore GTP-bound state is called active form. Because the intrinsic GTP hydrolysis and GDP/GTP exchange activities are low, GDP/GTP cycling is regulated by guanine-nucleotide-exchange factors (GEFs) and GTPase-activating proteins (GAPs). GEFs promote formation of the GTP-bound active form, on the other hands, GAPs accelerate the intrinsic GTPase activity and exchange active form to GDP-bound inactive form [54]. Though RHOA is stabilized by Rho (guanine nucleotide dissociation inhibitor)-GDI in cytoplasm via protein-lipid interaction, after extracellular stimulation, RHOA is recruited and anchored in cellular membrane and GTP/GDP exchange is occurred by GEFs and GAPs [55].

RHOA has various biological functions such as cytoskeleton organization, cell motility, tissue development and cytokinesis [51, 56, 57]. Its cellular functions are dependent on several effector proteins including Rho-associated protein kinase (ROCK), Protein kinase N (PKN), Phospholipase D2 (PLD2), Myosin phosphatase target subunit 1 (MYPT1), mDia, Citron, Rhotekin, and RhoGILIN [58, 59]. Within these effector molecules, it is reported that ROCK is a key regulatory protein of the

cellular functions such as cytoskeleton and cell polarity [60]. The relationship between RHOA and cancer have been investigated since long ago. It was reported that overexpression of RHOA was observed in various cancers such as colorectal, breast, liver, cervical and esophageal cancers, and its relationship to cell motility [61-63]. On the other hands, *RHOA* mutations were found in 2014. These mutations were accumulated in R5, G17 and Y42. G17 is located in GTP/GDP binding domain and Y42 is in effector protein binding region [43]. Therefore, *RHOA* mutations would contribute to DGC development in some form or other, however, the biological functions of mutated *RHOA* in DGC were poorly understood.

The fusion proteins between claudin 18 (CLDN18) and GAP6 or GAP26 (CLG) were found in DGC specific manner [45, 64, 65]. Interestingly, *RHOA* mutations and *CLG* fusions were mutually exclusive [45]. CLDN18 is tetraspan transmembrane protein and involved in the cellular tight junction. It is reported that CLDN18 has 2 isoform, isoform 1 are mainly expressed in the lung [66], on the other hand, the expression of isoform 2 is restricted to the stomach mucosa [67]. Yasui et al. showed that CLDN18 was downregulated in gastric cancer with Serial Analysis of Gene Expression analysis [68]. Both GAP6 and GAP26 are member of RhoGAP proteins [54]. GAPs have multiple domain structures such as SH2, SH3, RHOGAP, BAR and PH. GAP domain is the key regulator to hydrolysis of GTP-RHO and negatively regulate RHO-ROCK signaling. To control the GAP hydrolysis activity, BAR domain interacts with the GAP domain and inhibit its GAP activity [69]. It was reported that the

upregulation of GAP6 inhibited lung cancer cell growth, migration and invasion [70], but the relationship between GAP6 and gastric cancer is unknown. As for GAP26, the circulating GAP26 RNA was over-expressed in gastric cancer cells and its downregulation inhibited cancer cell growth [71], however there is no report to indicate the contribution to DGC development of GAP26.

The objective in this study is to evaluate the contribution of mutated *RHOA* in DGC development and reveal the mechanism with *in vitro* and *in vivo* model. In chapter 1, I demonstrated that *RHOA* mutations maintained cell survival and increased cell migration through the mechanism of ROCK signaling inactivation *in vitro*. I also revealed whether *CLG* fusions had the similar function with *RHOA* mutations or not. In chapter 2, I established *in vivo* model to evaluate the contribution of *RHOA* mutations for tumor development. I showed the transcriptome and pathological difference between orthotopic (ORT) engraftment and subcutaneous (SC) engraftment, and ORT model was suitable for exploring DGC biology. In chapter 3, I evaluated *in vivo* function of *RHOA* mutations with ORT model and observed the pathological similarity to clinical *RHOA*-mutated DGC. A series of evidence revealed the novel biological insights of *RHOA* mutations in DGC. Further studies targeting *RHOA* mutations are expected to develop future effective therapeutics in DGC.

Chapter 1

DGC-specific RHOA mutations maintained cancer cell survival and promoted cell migration

via ROCK inactivation

Abstract

RHOA missense mutations exist specifically in DGC and are considered one of the DGC driver genes, but it is not fully understood how *RHOA* mutations contribute to DGC development. Here I examined how *RHOA* mutations affect cancer cell survival and cell motility *in vitro*. I revealed that cell survival was maintained by specific mutation sites, namely G17, Y42, and L57. These mutations are located in functional domains of RHOA, so I evaluated the relationship between *RHOA* mutations and the major downstream ROCK signaling. When the expression of mutated *RHOA* was knocked down, the expression of RHOB and RHOC were increased. Additionally, the phosphorylation of Myosin regulatory light chain 2 (MLC2), that is one of the substrates of ROCK, and following actin stress fiber formation were clearly promoted. When I suppressed the expression of RHOB simultaneously with *RHOA* knockdown, MLC2 was not phosphorylated and cell death was not induced. Through the same ROCK inactivating mechanism, *RHOA* mutations increased cell migration activity. Therefore, I realized that *RHOA* mutations act in a dominant-negative fashion against the ROCK signaling and contributed cell survival and cell migration. Also, ROCK reactivation via RHOB is the key step of cell death after mutated *RHOAs* knockdown. GAPs negatively regulate the functions of RHO proteins including RHOA and inhibit following ROCK signaling. The fusion proteins of CLDN18 and ARHGAP (CLGs) are known to be mutually exclusive to *RHOA* mutations in DGC. I

revealed that CLGs contributed cell survival and migration via GAP domain, that is the key domain to hydrolysis RHO proteins. Taken together, these findings show that the inactivation of ROCK would be a key step in DGC development, so ROCK activation might provide novel therapeutic opportunities.

Introduction

DGC account for approximately 30% of all gastric cancers and are characterized by poorly differentiated adenocarcinoma with a worse prognosis than the intestinal type [36, 37, 72]. DGC infiltrate into adjacent stromal tissues, spread without clear polyps or ulcers, and frequently show intraperitoneal metastasis [73, 74]. Comprehensive genomic sequencing studies to identify DGC-specific genetic alterations, including my previous study, have shown that 14–25% DGC patients carry *RHOA* missense mutations, such as R5W, G17E, Y42C, and L57V [43–45].

RHOA is a small GTPase that belongs to the RHO family and has various biological functions, such as cytokinesis, cell motility, and tissue development [51, 56, 57]. RHOA cycles between the GDP-bound inactive form and the GTP-bound active form under the control of regulatory proteins like GEFs and GAPs. These regulatory proteins induce conformational change in RHOA to allow binding to substrates named effector proteins, one of which is ROCK. ROCK-LIMK-CFL1 signaling contributes to actin filament stabilization, while ROCK-MLCP-MLC signaling promotes actomyosin formation [75, 76].

In my previous work, I observed that a knockdown of *RHOA* in *RHOA*-mutated cancer cell lines represses cell survival significantly. Wang et al. also reported that introducing *RHOA* mutations, Y42 and L57V, to a murine intestinal organoid promotes cell survival [44]. Moreover, a comprehensive

investigation of The Cancer Genome Atlas (TCGA) revealed that negative regulators of RHOA, *GAP6* and *GAP26*, fused with the tight junction membrane protein *CLDN18* in a DGC-specific manner [45]. The frequency of *CLG* fusions is 15% in DGC and, interestingly, *RHOA* mutations and *CLG* fusions are mutually exclusive. Although these results suggest that a dysregulated RHOA signal is related to DGC development, the details remain to be understood. In this chapter, I explored the contribution of *RHOA* mutations to DGC development, focusing on cell survival and also on cell motility, which is one of the features of DGC. Furthermore, I evaluated the functional relationship between *RHOA* mutations and *CLG* fusions.

Materials and Methods

Cell lines

The human cancer cell lines SK-UT-1, SNU-16, SW948, and BT474 were obtained from the American Type Culture Collection (ATCC); HCC95, SNU-719, SNU-484 and SNU-638 from Korean Cell Line Bank (KCLB); GP2D and OE19 from the European Collection of Animal Cell Cultures (ECACC); CCK81, KNS-62, MKN45 and MKN74 from the Japanese Collection of Research Bioresources (JCRB); CJM from Riken; and QG-56 from IBL. Each cell line was cultured using the medium recommended by the suppliers and maintained in a humidified incubator at 37°C with 5% CO₂, except for SW948 cells, which were cultured without CO₂.

Generation of SW948 and MKN74 cell lines expressing *RHOA* mutants or *CLG* fusion genes

For the rescue studies, silencing mutations were introduced into the *RHOA* coding sequence (NCBI RefSeq Sequence: NM_001664.3) so that introduced *RHOA* were resistant to *RHOA*-siRNAs. cDNA of *CLDN18* (NCBI RefSeq Sequence: NM_001002026.2), *GAP6* (NCBI RefSeq Sequence: NM_013423.2), and *GAP26* (NCBI RefSeq Sequence: NM_001135608.1) coding sequences was amplified in mutation-negative cancer cell lines or a cDNA library of normal human tissue (Ambion). cDNA of *CLG26* fusion gene was amplified by RT-PCR from a fusion-positive gastric cancer clinical

specimen. The synthesis of *CLG6* fusion genes that combined cDNAs of *CLDN18* and *GAP6* was referred from a published report [45]. *CLDN18* was fused to *GAP6* and *GAP26* that included the GAP domain. These sequences were inserted into the pLVSIN-CMV vector (Takara). Expression plasmids for each *RHOA* mutant and for *CLG26* mutant with GAP domain were generated using site-directed mutagenesis PCR and the In-Fusion HD Cloning system (Clontech). The mixture of expression vector and ViraPower Lentiviral Packaging Mix (Thermo Fisher) was introduced into Lenti-X 293T cells (Takara) using FuGENE HD Transfection Reagent (Promega). After 48 hrs, the culture medium was harvested and virus particles were concentrated with Lenti-X Concentrator (Takara). Prepared lentivirus was transfected into each cell line with hexadimethrine bromide (final 8 $\mu\text{g}/\text{mL}$). Hygromycin was added to establish stable transfectants at a final concentration of 500 $\mu\text{g}/\text{mL}$ for SW948 and 25 $\mu\text{g}/\text{mL}$ for MKN74.

Inhibition and rescue assays of cell survival in 3D conditions

An assay to evaluate the inhibition of cell survival in siRNA-treated cells and a function rescue assay were performed as described previously [43]. In brief, cells were seeded in 96-well ultra-low attachment plates (Corning) in triplicate wells. At the same time, mixtures of siRNA and Lipofectamine RNAiMAX reagent (Thermo Fisher) were added to each well as 0.5 or 1 or 5 nM of siRNA solutions. The sequences of siRNAs are listed in Table 1-1A. As a non-targeting negative

control siRNA, Silencer Select Negative Control No.1 siRNA (Thermo Fisher) was used. The investigation of *RHOA* mutated cancer cell lines was utilized public database; CCLE; <https://portals.broadinstitute.org/ccle/home> and COSMIC; <http://cancer.sanger.ac.uk/cosmic>. The 12 cell lines shown in Figure 1-1 were selected based on three criteria; namely, knockdown efficiency of *RHOA*-siRNA (over 75%), cell survival inhibition activity by *KIF11*-siRNA (over 70%), and mutation status, which was confirmed in-house. Each cell line had heterogeneous mutated and WT *RHOA*. In *RHOA* double-mutated cells (KOSC-2, CCK-81, and SNU-16), each mutation existed on different alleles. The viable cells were measured 7 days after siRNA transfection using the CellTiter-Glo 3D Cell Viability Assay (Promega). In the rescue assay, cell survival inhibition assays were performed in SW948 cell lines using siRNA-resistant *RHOA* or treatment with Y-27632 or *RHOB/RHOC*-siRNAs. For transient expression, I inserted each mutated *RHOA* into a pEBMulti-Neo vector (Wako). Each plasmid was transfected into SW948 cells by electroporation with the Nucleofector system (Lonza). Then the procedure described above was followed.

qRT-PCR

Cells were seeded in 6-well ultra-low attachment plates (Corning). Total RNA was extracted using the RNeasy Mini Kit (Qiagen). To evaluate *RHOA*, RNAs were extracted after 2 days of *RHOA*-siRNA treatment, and to evaluate *CLG* fusion genes, RNAs were extracted after 2 days of cell seeding.

qRT-PCR was performed with Power SYBR Green PCR Master Mix (Applied Biosystems), using the primers. The sequences of primers are listed in Table 1-1B. PCR reactions were performed at 48°C for 30 min and 95°C for 10 min, followed by 40 cycles of 95°C for 15 sec and 60°C for 1 min. Values obtained in qRT-PCR were normalized with *RPS18*.

Western blot analysis

Two days after transfection, cells were also lysed in RIPA buffer (Wako) supplemented with a protease inhibitor cocktail (Roche) and the phosphatase inhibitor PhosSTOP (Roche), and concentrations of the extracts were estimated with a DC protein assay (Bio-Rad). Total cell extract (3–5 µg of protein per lane) was subjected to sodium dodecyl sulfate polyacrylamide gel electrophoresis, and the separated proteins were electrophoretically transferred to Immobilon-P membranes (Millipore). After blocking in Blocking One (Nacalai Tesque), the membranes were incubated in primary antibodies against RHOA (Cell Signaling, #2117), RHOB (Cell Signaling, #2098), RHOC (Cell Signaling, #3430), phospho-CFL1 (Ser3) (Cell Signaling, #3313), CFL1 (Cell Signaling, #5175), phospho-MLC2 (Thr18/Ser19) (Cell Signaling, #3674), MLC2 (Cell Signaling, #8505), phospho-LIMK1 (Thr508)/LIMK2 (Thr505) (Cell Signaling, #3841), LIMK1 (Cell Signaling, #3842), LIMK2 (Cell Signaling, #3845), phospho-MYPT1 (Thr696) (Cell Signaling, #5163), phospho-MYPT1 (Thr853) (Cell Signaling, #4563), MYPT1 (Cell Signaling, #8574), and ACTB (Sigma-Aldrich,

A1978). ACTB was used as an internal control.

Structural analysis

The homology modelling of RHOA-GAP26 was constructed from an X-ray crystallographic structure of the RHOA-GAP1 complex (PDB: 1TX4; <https://www.rcsb.org/pdb/home/home.do>) using MOE2014 software (Chemical Computing Group). The figure of the RHOAGAP26 complex was drawn using PyMol v4.2.0 software (Schrödinger).

Migration and invasion assay

The MKN74 cell line was selected because it originated as differentiated gastric cancer, had *RHOA*-WT with no clear oncogenes (e.g. *KRAS*, *FGFR2*, *HER2* etc.), and was easy to handle for transfection. FluoroBlok Multiwell Insert Systems with an 8- μ m pore size (Corning) were used to perform the cell migration assay for MKN74 transfectants. The cells were seeded on top of the filter inserts in 1% FBS medium. Then the inserts were placed into the lower chamber, which was loaded with 10% FBS medium. Following incubation for 48 hrs, the cells that traversed the filter were stained with calcein AM (Dojindo), and the fluorescence was read by EnVision Multilabel Reader (PerkinElmer). Stained cells were analyzed with an IX83 Inverted Microscope (Olympus) using a UPLFLN 4X PH objective lens. Photo data processing was performed by Olympus cellSens

Dimension software ver 1.15 (Olympus). For invasion, BioCoat Tumor Invasion Multiwell Plates with 8- μ m pore size (Corning) were used. Invasion plates were re-hydrated with FBS-free media at 37°C for 2 hrs. After that, the procedure was the same as the migration assay. Invasion activity was calculated according to the maker's protocol (invasion activity = mean number of invading cells/mean number of migrating cells).

Immunocytochemistry and confocal microscopy

Cells were seeded on Nunc Lab-Tek II CC2 Chamber Slide Systems (Thermo Fisher) and either siRNAs were added simultaneously or Y-27632 was added after 24 hrs incubation. 48 hrs later, cells were fixed with 4% PFA, permeabilized in 0.5% Triton X-100/PBS, and stained with Rhodamine Phalloidin (Thermo Fisher). DAPI was used for nuclear staining. Stained cells were analyzed with the A1 confocal fluorescence microscopy system (Nikon) using a CFI Apochromat Lambda S 60x Oil lens. Photo data processing was performed by NISElements software (Nikon).

Results

RHOA-siRNA treatment inhibited 3D cell survival of RHOA-mutated cell lines in a mutation-dependent manner

To identify which mutation sites contribute to cancer cell survival, I selected *RHOA*-mutated cell lines from public databases (Table 1-2) and chose 12 cell lines. In 3D culture conditions, I evaluated the inhibition efficacy of *RHOA*-siRNAs on cell survival and observed significant *RHOA*-siRNA dependent inhibition in cell lines HCC95, SW948, BT474, and OE19, which carried G17 or Y42 single mutations (Figure 1-1). On the other hand, cell survival inhibition seen in R5, Y34, E40, A61, and A69 single mutants or in R5/Y42 or R5/F39 double mutants was less clear, and cell survival of 4 *RHOA*-WT cell lines was not inhibited (Figure 1-2). These results indicated that *RHOA* mutations showed site dependent function for cell survival.

Mutated RHOA contributed cell survival, and G17V, Y42C, Y42S, and L57V mutations showed functional complementarity to G17E

Next, I investigated which types of *RHOA* contribute to cell survival in SW948 cells, which express G17E- and WT-*RHOA* heterogeneously. I used stable SW948 transfectants that expressed siRNA-resistant G17E- and WT-*RHOA*. After 48 hrs of *RHOA*-siRNA treatment, protein expression

of the siRNA-resistant RHOA was confirmed by Western blot analysis (Figure 1-3A). Because protein expression was faint, the expression of G17E/V, which was confirmed by quantitative RT-PCR (qRT-PCR) (Figure 1-3B). Then, I evaluated whether *RHOA*-siRNA continued to inhibit cell survival or not (Figure 1-4). While the introduced G17E mutation restored cell survival, the WT did not. Therefore, it was revealed that mutated-*RHOA* was dominant phenotype and *RHOA* mutations but not WT contributed to cell survival and *RHOA* mutations.

I also checked the functional complementarity with mutations that were found in clinical specimens. Because L57V-mutated cancer cell lines were unavailable commercially, I added the mutation for this experiment. The siRNA-dependent inhibition of cell survival was cancelled not only by the introduction of G17E, but also of G17V, Y42C, Y42S, and L57V; however, it was not cancelled by the R5W mutant (Figure 1-4). To negate the possibility if the expression level of introduced *RHOA* mutations were not sufficient, I also expressed abundant mutated *RHOA* transiently in SW948 (Figure 1-5A) to evaluate cell survival, and the same tendency was observed (Figure 1-5B). These results revealed that the mutations in G17, Y42, and L57 also contributed to cancer cell survival.

***RHOA*-knockdown in *RHOA*-mutated SW948 induced ROCK activation via RHOB**

To reveal the signal cascade that contributes to cell survival, I analyzed the time course of the ROCK pathway, which is one of the major RHOA signaling pathways, after *RHOA*-siRNA

treatment. I also evaluated the change in other RHO family proteins, RHOB and RHOC, and in signal molecules, ROCK1/2, MLC2, MYPT1, LIMK1/2, and CFL1. RHOA protein expression was knocked down significantly on Day 1 after *RHOA*-siRNA treatment and was almost completely depleted on Day 2 (Figure 1-6), while the expression of RHOB and RHOC proteins was accordingly elevated. *RHOA*-siRNA treatment elevated the phosphorylation of MLC2 (Thr18/Ser19). I also noted that MYPT1 (Thr696 and Thr853), which is a phosphatase of MLC2, was not phosphorylated (Figure 1-7), and LIMK1 (Thr508)/LIMK2 (Thr505) and CFL1 (Ser3) were constantly phosphorylated independently of *RHOA*-siRNA. From these results, I assumed that RHOA depletion induced ROCK-MLC2 signal activation. To clarify whether the ROCK activation induced by RHOA depletion affected the cytoskeleton or not, I stained for actin stress fiber. After *RHOA*-siRNA treatment, the formation of actin stress fiber was clearly increased and the shape was spiky (Figure 1-8). This result verified that a knockdown of *RHOA* activated ROCK and stimulated actin stress fiber formation. Next, to investigate whether the suppression of ROCK would promote cell survival or not, I evaluated the effect of a ROCK1/2 inhibitor, Y-27632, on the cell survival of SW948. I confirmed Y-27632 up to 33 μ M did not affect SW948 cell survival (Figure 1-9). After treatment with Y-27632, the survival rate of *RHOA*-siRNA treated cells recovered significantly from 24% (nontreatment) to 82% (3 μ M) and 92% (10 μ M) (Figure 1-10). Y-27632 also inhibited the phosphorylation of MLC2 (Figure 1-11). I revealed that inactivation of ROCK promoted cell survival. Overall, this series of results revealed that *RHOA*

mutations keep ROCK inactive, so their effect on ROCK is negative regulator.

I hypothesized that ROCK reactivation would be induced by RHOB and/or RHOC, because the expression of these RHO molecules was elevated after *RHOA*-siRNA treatment. To evaluate this hypothesis, I used *RHOB* and/or *RHOC*-siRNAs for a rescue study. The survival rate of *RHOA*-siRNA-treated cells increased significantly from 13% to 61% (+*RHOB*- and *RHOC*-siRNAs), 59% (+*RHOB*-siRNA) and 24% (+*RHOC*-siRNA) (Figure 1-12A). *RHOB*-siRNA inhibited the phosphorylation of MLC2 induced by *RHOA*-siRNA treatment (Figure 1-12B). These results revealed that ROCK activation was induced by RHOB in SW948.

The inhibition of cell survival by *RHOA*-siRNA was cancelled by *CLG* fusions and *GAPs*, but not by *CLDN18*

To reveal the functional relationship between *RHOA* mutations and *CLG* fusions, I treated stable SW948 transfectants that expressed *CLG* fusions with *RHOA*-siRNA. The expression was validated by qRT-PCR (Figure 1-13A, 1-13B). Utilizing these cell lines, I evaluated the effect on cell survival. The domain structures of CLDN18, GAP6, GAP26, CLG6, and CLG26 are shown in Figure 1-14A. *RHOA*-siRNA-dependent cell survival inhibition was canceled by *CLG6*, *CLG26*, *GAP6*, and *GAP26*, but not by *CLDN18* (Figure 1-14B). These results indicated that *CLG* fusions complemented *RHOA* mutations, in terms of their effect on cell survival.

Further investigation served to confirm whether survival in cells with *CLG* fusions was dependent on *GAP*, which inactivates RHOA. A published report indicated the intensity of the RHOA and GAP26 interaction by showing that mutations of K454 and R458 in GAP26 remarkably decreased the thermodynamic and kinetic scores [69]. Using 3D modeling, I confirmed that K454 and R458 are important for the interaction between GAP26 and RHOA (Figure 1-14C) because they form hydrogen bonds to D65 in RHOA. Therefore, I introduced K454A/R458E double-mutated *CLG26* into SW948 and established a stable transfectant in which GAP activity was eliminated. This double mutation in the GAP domain significantly decreased the contribution of *CLG26* to survival (Figure 1-14D). These results suggested that GAP activity was necessary for cell survival.

RHOA mutations and CLG fusions induced migration activity by inactivating ROCK

Next, I evaluated the effect of *RHOA* mutations on cell motility, which is a feature of DGC. I introduced WT, G17E, Y42C, and Y42S into MKN74. The validated expression level was shown in Figure 1-15. I used the transfectants for migration and invasion assays in a Boyden chamber. Compared with mock, G17E, Y42C, and Y42S promoted cell migration activity 1.6- to 2.0-fold, whereas WT decreased the migration activity 0.65-fold (Figure 1-16A). Representative images of the migration assay are shown in Figure 1-16B. I also evaluated the invasion activity of these transfectants with a Matrigel-coated chamber, but a clear difference was not observed (Figure 1-16C).

As for *CLG* fusion genes, I established each transfectant (Figure 1-17A, 1-17B, 1-17C). When I evaluated cell motility in *CLG* fusions, migration activity compared with mock was significantly increased by *CLG6*, *CLG26*, *GAP6*, and *GAP26*, but not by *CLDN18* (Figure 1-18A). However, when the K454A/ R458E double mutation in the GAP domain was introduced to the *CLG26* transfectant, the migration activity was diminished (Figure 1-18B). I revealed that, similarly to *RHOA* mutations, *CLG* fusions contributed to migration activity in addition to cell survival, and that this contribution was dependent on the GAP activity.

As in the cell survival assays, I clarified the relationship between cell migration and ROCK activation by staining for actin stress fiber to reveal the cytoskeleton of MKN74 transfectants (Figure 1-18C). The mock transfectant showed clear stress fiber formation localized around cell clusters; on the other hand, G17E, Y42C, and Y42S showed weaker actin stress fiber formation, and their localization around cell clusters was unclear. These cytoskeletal changes induced by *RHOA* mutations were similar to those found in Y-27632-treated cells, which indicates the possibility that the inactivation of ROCK also contributed to migration activity. To verify this hypothesis, I evaluated the migration activity of MKN74 after Y-27632 treatment. I confirmed Y-27632 up to 100 μ M did not affect MKN74 cell survival (Figure 1-18D). As a result, Y-27632 increased migration activity 2.1-fold (3 μ M) and 2.9-fold (10 μ M) compared with non-treatment (Figure 1-18E). These results revealed that the inactivation of ROCK promoted cell migration activity.

Discussion

In this study, I revealed that *RHOA* mutations promoted cancer cell survival and migration activity by inactivating ROCK. At first, the presence of several hotspot amino acids made me assume that *RHOA* mutations would be gain-of-function mutations, similar to mutations in *RAS* and *RAC* [78-81]. However, contrary to my expectations, the knockdown of *RHOA* induced ROCK activation, and a ROCK inhibitor achieved cell survival similar to that seen in *RHOA* mutations; therefore, I concluded that functional *RHOA* mutations were loss-of-function (LoF) mutations for ROCK activation. Wang et al. reported that the amount of GTP form of RHOA in Y42C and L57V was less than that in WT and G14V in a pull-down assay [44], which would support my conclusion. Although *RBI* and *VHL* are well known as tumor suppressor genes that have LoF mutations, they have no clear hotspots [82]. Despite the presence of hotspots, the *RHOA* mutations were LoF type, and cell lines acquired dominant-negative features when site-specific mutations were introduced. My analysis demonstrated that the hotspot mutations at G17, Y42, and L57 contributed to cell survival, but not those at R5 and L69. On the other hand, in Burkitt's lymphoma, R5 mutation was reported to be a hotspot and to suppress RHOA-ROCK signaling [83], which suggests that the mechanism by which *RHOA* mutations induce dominant-negative properties might vary depending on the tumor type or cell type. My next challenge will be to clarify the mechanism by which each *RHOA* mutant inactivates

ROCK signaling in DGC.

My study provided interesting insights about the mechanism of cell death by *RHOA* knockdown. Firstly, *RHOA* knockdown reactivated the ROCK pathway mainly via RHOB. I observed that the protein expression of RHOB and/or RHOC was induced in other cell lines besides SW948 (Figure 1-19), as have other groups [84], which suggests that homeostasis to keep the total amount of RHOs is generally maintained. RHOs have been previously reported to complement each other functionally [53, 85]. Mutated *RHOA* suppresses ROCK activation, but it was interesting to see that upregulated RHOB after *RHOA* knockdown revitalized ROCK signaling through this complementary mechanism. Secondly, ROCK activation induced cell death in *RHOA* mutated cancer cells. In human ES cells and iPS cells, it has been reported that the inactivation of the ROCK pathway significantly enhances recovery of cells from cryopreserved stocks in cell culture [86]. Upon dissociation, these cells become vulnerable to apoptosis via a phenomenon called apoptotic membrane blebbing. The molecular mechanism that causes apoptotic membrane blebbing would involve ROCK signaling activation [87]; that is to say, the phosphorylation of MLC2 by ROCK induces hyperactivation of actomyosin and leads to dissociation-induced apoptosis. As its name suggests, cancer cells of DGC spread from the epithelial layer and diffuse into gastric stromal tissue. Similarly to ES and iPS cells, inactivation of ROCK might protect these vulnerable cancer cells from apoptotic cell death.

The inactivation of ROCK signaling induced by *RHOA* mutations promoted not only cell

survival but also cell migration. *RHOA* mutations decreased the accumulation of actin stress fiber around cell clusters and reduced intercellular adhesion, thus loosening the aggregation of cells. These morphological changes might promote cell migration. This possibility is supported by a report that diminished cell-cell interaction by actomyosin was an important step for collective cell migration, the phenomenon by which a group of cells move in concert without completely losing their cell-cell attachment [88]. Several reports that have investigated the relationship between RHOA and cell motility showed that activation of RHOA by overexpression of WT or the constitutive active form (G14V) promoted cell migration [89, 90]. In contrast, my results showed that the introduction of WT and G14V decreased cell migration, and the dominant-negative mutation (T19N) enhanced cell migration (Figure 1-20). To find out how the different patterns of actin stress fiber accumulation affect cell migration, further time-dependent and cell-type-dependent analyses are necessary.

In this study, I revealed that *CLG* fusions and *RHOA* mutations share a functional relationship; namely, in promoting cancer cell survival and migration. My mutagenesis experiments showed that the GAP domain was critical for the function of *CLG* fusions. Originally, GAPs have a BAR domain, which works as a feedback mechanism to suppress over-activated GAP activity [69], but *CLG* fusions lose their BAR domain. So I assumed that *CLG* fusions promote hydrolysis of GTP-RHOA to GDP-RHOA and thus inactivate ROCK signaling. Since *RHOA* mutations and *CLG* fusions are both DGC-specific genetic alterations and are mutually exclusive, the inactivation of ROCK

signaling would be a key step in the development of DGC. A ROCK signaling activator might show broad therapeutic opportunities for ROCK-inactivated DGC patients.

Tables and Figures

Table 1-1: DNA and RNA oligonucleotide sequences utilized in this study

(A) siRNA sequences		
Target	sense/antisense	siRNA sequences
<i>RHOA</i>	sense	5'-cuaugauuuuuacgaugutt-3'
(s759)	antisense	5'-acaucguuuuuuucauagt-3'
<i>RHOA</i>	sense	5'-ggcuuuacuccguaacagatt-3'
(s760)	antisense	5'-ucuguuacggaguuagccct-3'
<i>RHOB</i>	sense	5'-ugauaucccuugucuguaatt-3'
(s1575)	antisense	5'-uuacagacaagggauucaag-3'
<i>RHOC</i>	sense	5'-aggacugcauuguuuuuaatt-3'
(s99)	antisense	5'-uagaaaacaauagcaguccgg-3'
<i>KIF11</i>	sense	5'-ccaucaacacugguagaatt-3'
	antisense	5'-uucuuaccaguguugauggt-3'

(B) DNA oligonucleotide sequences for RT-PCR are listed		
Target	forward/reverse	Primer sequences
<i>RHOA</i>	forward	5'-gggagctagccaagatgaag-3'
	reverse	5'-gtacccaaaagcgccaatc-3'
<i>RPS18</i>	forward	5'-gtgctgcagccatgtctct-3'
	reverse	5'-gcagtgatggcaaaggctat-3'
<i>CLDN18</i>	forward	5'-gagtgccgggctacttcac-3'
	reverse	5'-ggcaaaagatggataccaggagg-3'
<i>GAP6</i>	forward	5'-tcgtcgtcaaagtcaagggaa-3'
	reverse	5'-tgttgaatccaagttccca-3'
<i>GAP26</i>	forward	5'-gaacttcgttcacagcaggc-3'
	reverse	5'-gatgaggccagtcttccgt-3'
<i>CLG6</i>	forward	5'-ctggaggctcaaggccag-3'
	reverse	5'-ggcctgacatgctgtcca-3'
<i>CLG26</i>	forward	5'-cacagaggacgaggtctaca-3'
	reverse	5'-ctgaagccaatgctgtccaac-3'

Table 1-2: Summary of the mutation spectrum of *RHOA* in cancer cell lines

NAME	TISSUE	STATUS	Validated mutations
SK-UT-1	Uterus	Mesodermal tumor	p.R5Q
MDA PCa 2b	Prostate	Adenocarcinoma	p.R5W
KOSC-2	Head & Neck (mouth)	Squamous cell carcinoma	p.R5Q, p.E40Q
CCK-81	Colon	Adenocarcinoma	p.R5Q, p.Y42C
SNU-16	Stomach	Adenocarcinoma	p.R5W, p.F39L
SW948	Colon	Adenocarcinoma	p.G17E
BT-474	Breast	Ductal carcinoma	p.G17E
HCC95	Lung	Squamous cell carcinoma	p.G17A
NUGC-2	Stomach	Adenocarcinoma	p.G17E
NCI-H2170	Lung	Squamous cell carcinoma	p.A3V
GP2d	Colon	Adenocarcinoma	p.Y34C
CJM	Head & Neck (mouth)	Squamous cell carcinoma	p.E40Q
OE19	Esophagus	Adenocarcinoma	p.Y42S
SNU-719	Stomach	Adenocarcinoma	p.A61V
KYSE140	Esophagus	Squamous cell carcinoma	p.Y66D
QG-56	Lung	Squamous cell carcinoma	p.L69P
KNS-62	Lung	Squamous cell carcinoma	p.L69P
MOLT-16	Blood	T acute lymphoblastic leukemia	p.D120N

Mutations were investigated in public databases CCLE and COSMIC and validated by in-house sequencing of hotspot regions.

Mutations were investigated in public databases CCLE and COSMIC and validated by in-house sequencing of hotspot regions.

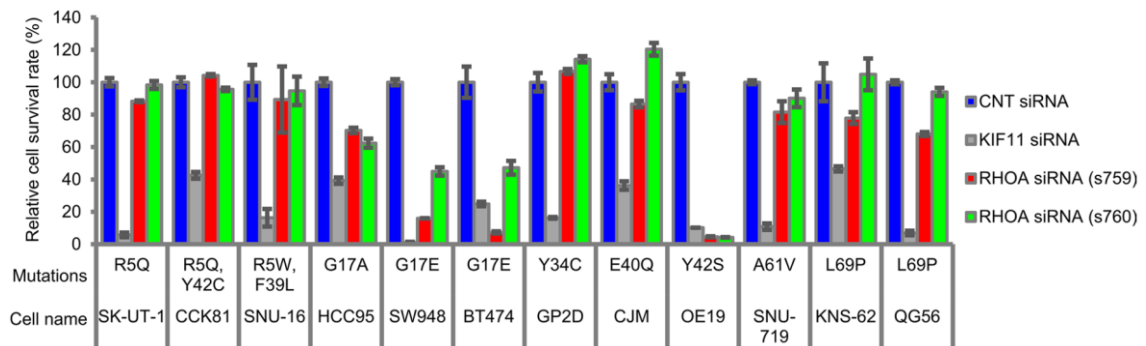


Figure 1-1: Cell survival rate of various types of cancer cell lines treated with *RHOA*-siRNAs

Endogenous *RHOA*-mutated cancer cell lines were seeded in a low attachment plate and then treated with each siRNA for 7 days. The viable cells were measured by CellTiter-Glo 3D Cell Viability Assay. Data are shown as mean \pm SD ($n = 3$). Cell selection criteria (see Materials & Methods) ensured the knockdown efficiency of siRNAs.

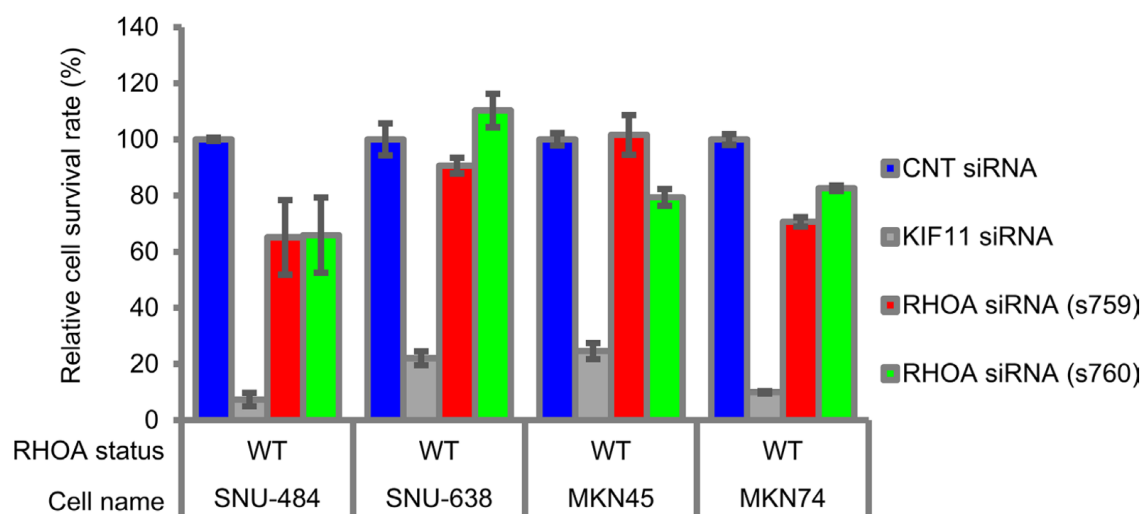


Figure 1-2: Inhibition by *RHOA*-siRNAs of cell survival in *RHOA*-WT gastric cancer cell lines

Cell lines were seeded in a low attachment plate and then treated with each siRNA for 7 days. The

viable cells were measured by a CellTiter-Glo 3D Cell Viability Assay. Data are shown as mean \pm SD

($n = 3$).

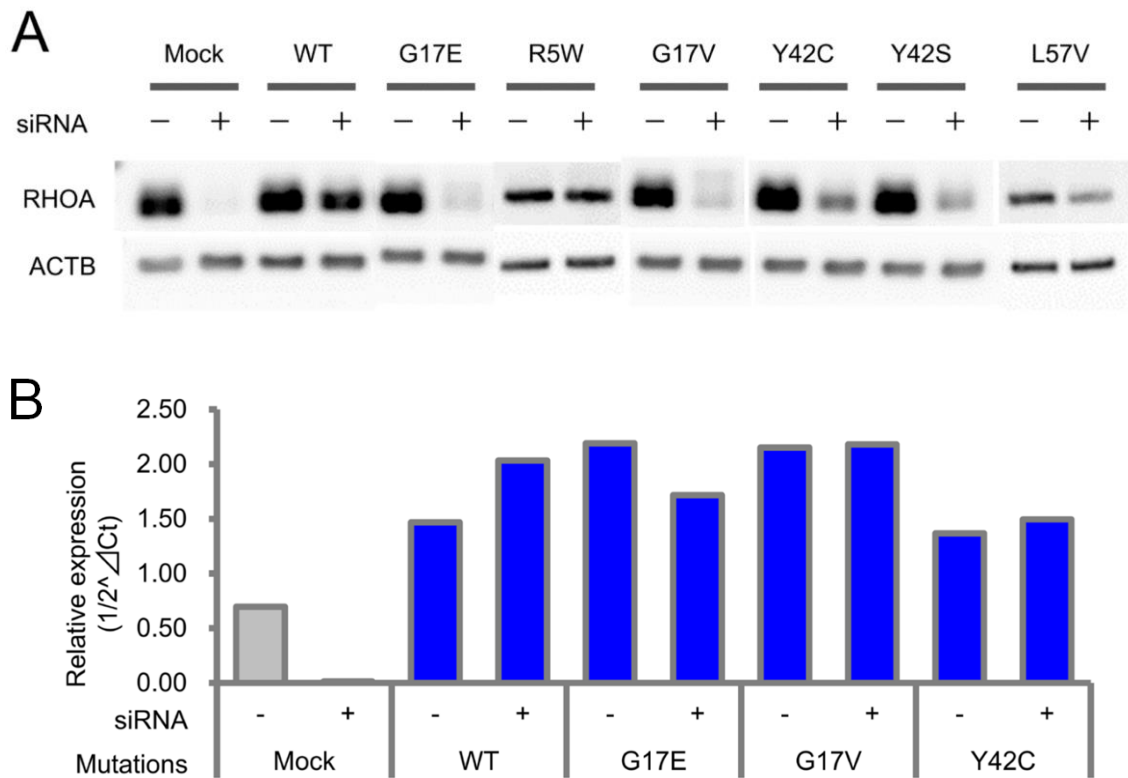


Figure 1-3: Protein (A) and mRNA (B) expression analysis of SW948 transfectants

(A) Cells were seeded in a 6-well plate and then *RHOA*-siRNA was added. Proteins were eluted on day 2, and RHOA protein expression was detected by western blotting. (B) *RHOA* mRNA expression of SW948 transfectants of WT, G17E, G17V, and Y42C by qRT-PCR. Cells were seeded in a 6-well plate and then *RHOA*-siRNA was added. After 2 days incubation, mRNA expressions were compared by qRT-PCR. The PCR condition is described in Materials and Methods. Values obtained in qRT-PCR were normalized with *RPS18*.

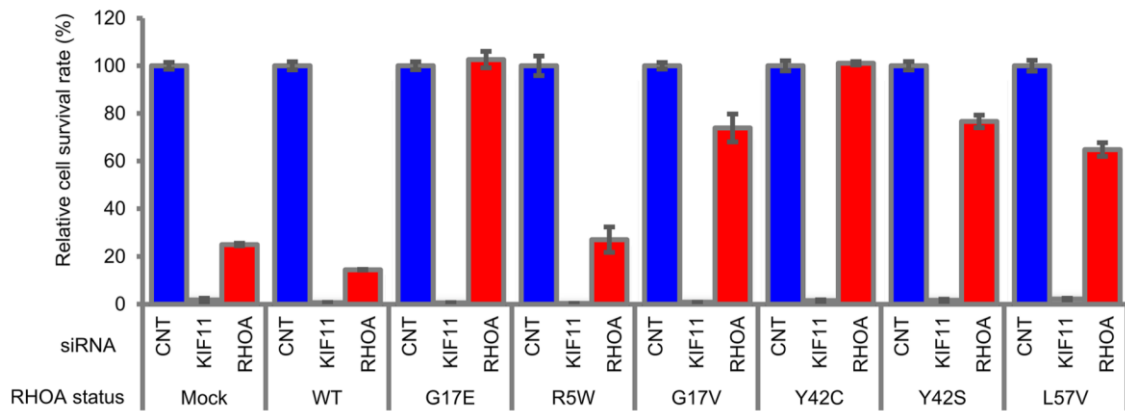


Figure 1-4: Rescue study of *RHOA*-siRNA-dependent inhibition of cell survival in SW948

SW948 was transfected with WT and each mutated *RHOA*. Cell lines were seeded in a low attachment plate and then treated with each siRNA for 7 days. The viable cells were measured by a CellTiter-Glo 3D Cell Viability Assay. siRNA ID: s759 was used for *RHOA*-siRNA. Data are shown as mean \pm SD ($n = 3$). Protein expression levels are shown in Figure 1-1A.

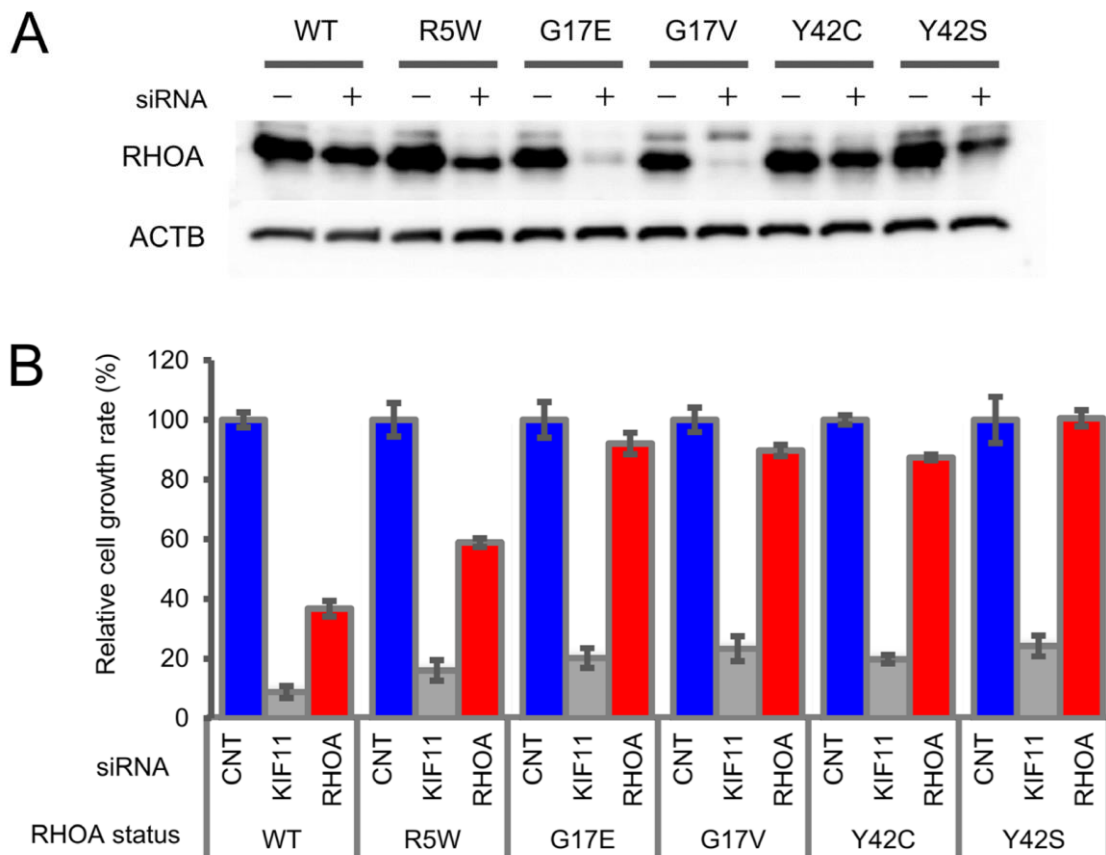


Figure 1-5: Rescue study of *RHOA*-siRNA-dependent inhibition of cell survival in SW948 cells

that had been transfected to transiently express abundant WT *RHOA* and each mutated *RHOA*

(A) Protein expression of each transfectant. Each vector plasmid was transfected into SW948 cells by

electroporation. 2 days after electroporation, cells were seeded in a 6-well plate and then *RHOA*-

siRNA was added. After 2 days incubation, proteins were eluted and *RHOA* protein expression was

detected by western blotting. (B) Each cell line was seeded in a low attachment plate and then treated

with each siRNA for 7 days. The viable cells were measured by CellTiter-Glo 3D Cell Viability Assay.

Data are shown as mean \pm SD ($n = 3$). siRNA ID: s759 was used for *RHOA*-siRNA. Data are shown

as mean \pm SD ($n = 3$).

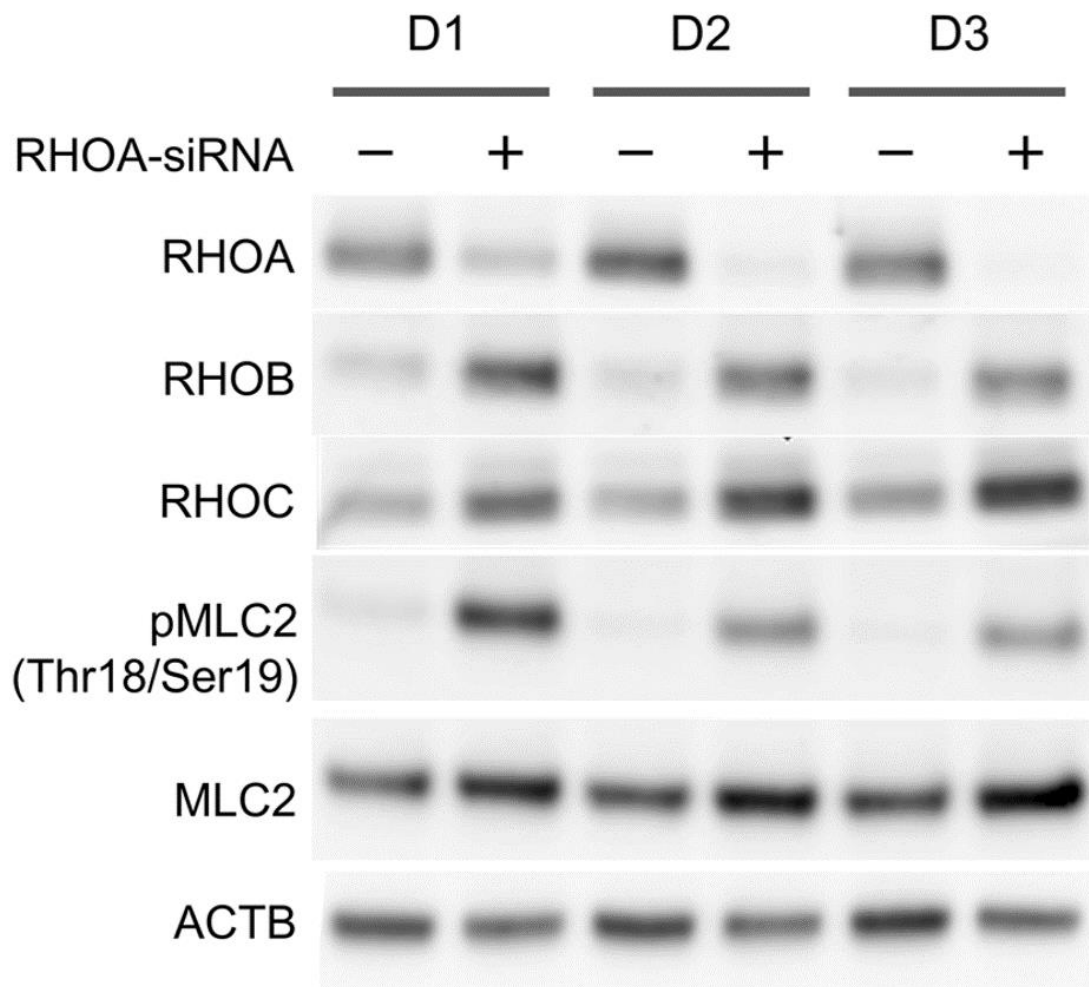


Figure 1-6: Expression analysis of RHO pathway related molecules

Expression of RHOA, RHOB, and RHOC, and phosphorylation of MLC2 in SW948 treated with 1 nM of *RHOA*-siRNA. Proteins were harvested on days 1, 2, and 3 after siRNA treatment. The protein expression levels were detected using western blotting.

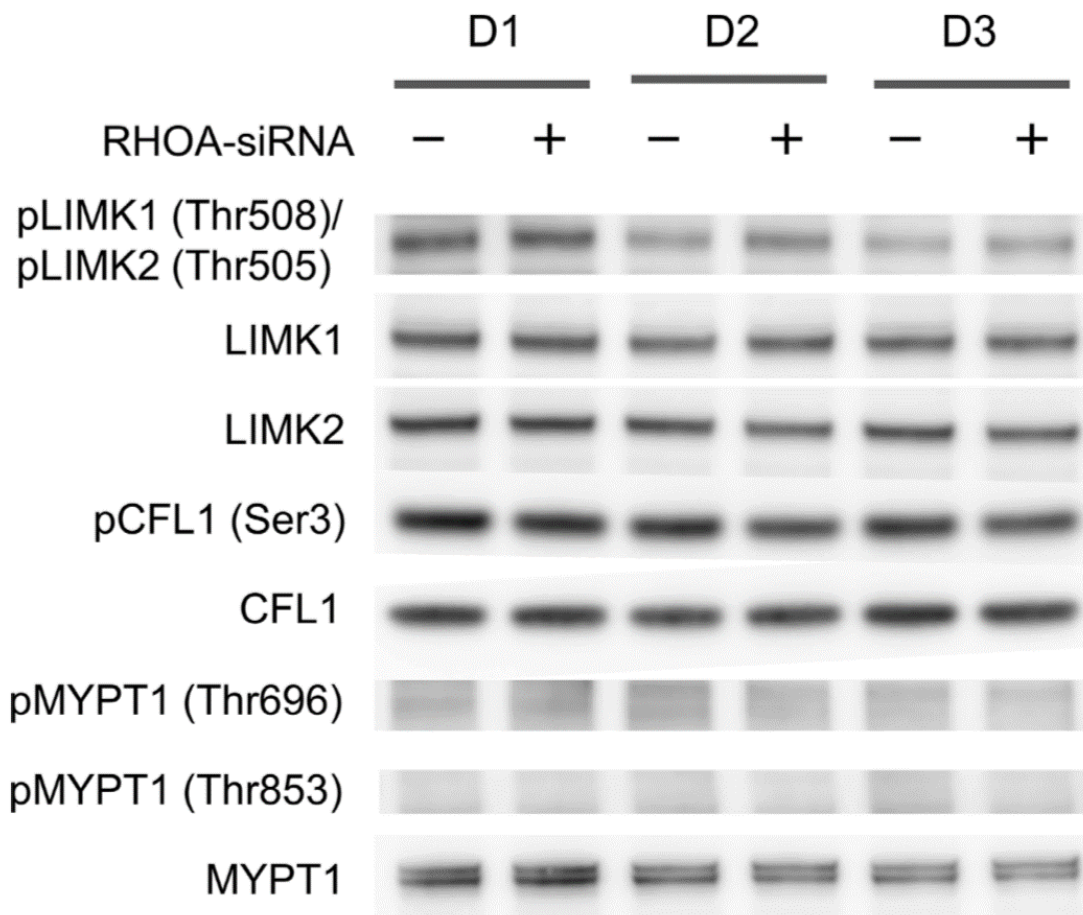


Figure 1-7: Phosphorylation of LIMK1, LIMK2, CFL1, and MYPT1 in SW948 treated with 1 nM of *RHOA*-siRNA

Proteins were harvested on days 1, 2, and 3 after siRNA treatment. The protein expression levels were detected using western blotting.

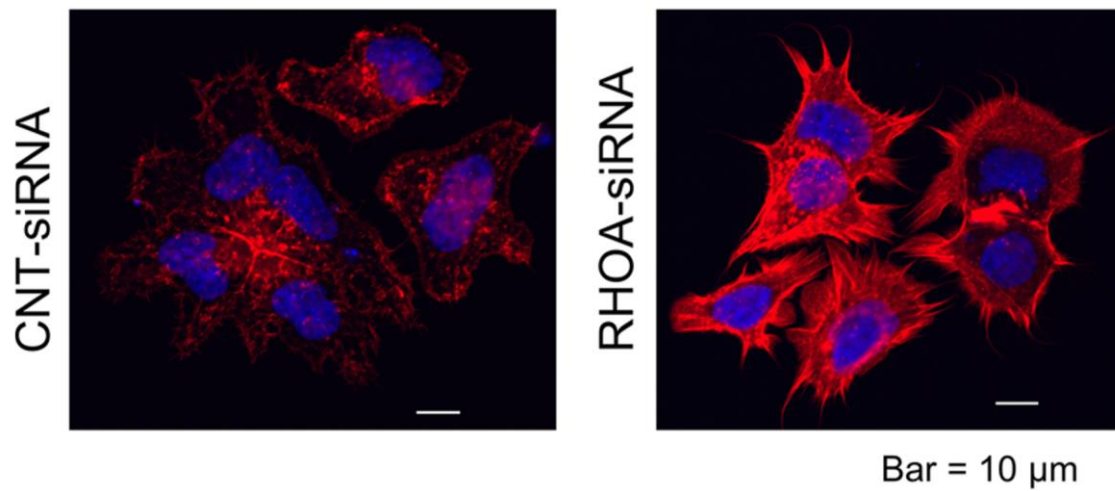


Figure 1-8: Actin stress fiber formation in SW948

Actin stress fiber of SW948 treated with 1 nM of *RHOA*-siRNA. Actin stress fibers were stained with Rhodamine Phalloidin, and DAPI was used for nuclear staining. Stained cells were analyzed with confocal fluorescence microscopy. Representative images of three independent chambers are shown. Details of immunocytochemistry are described in Materials and Methods. Scale bar shows 10 μm.

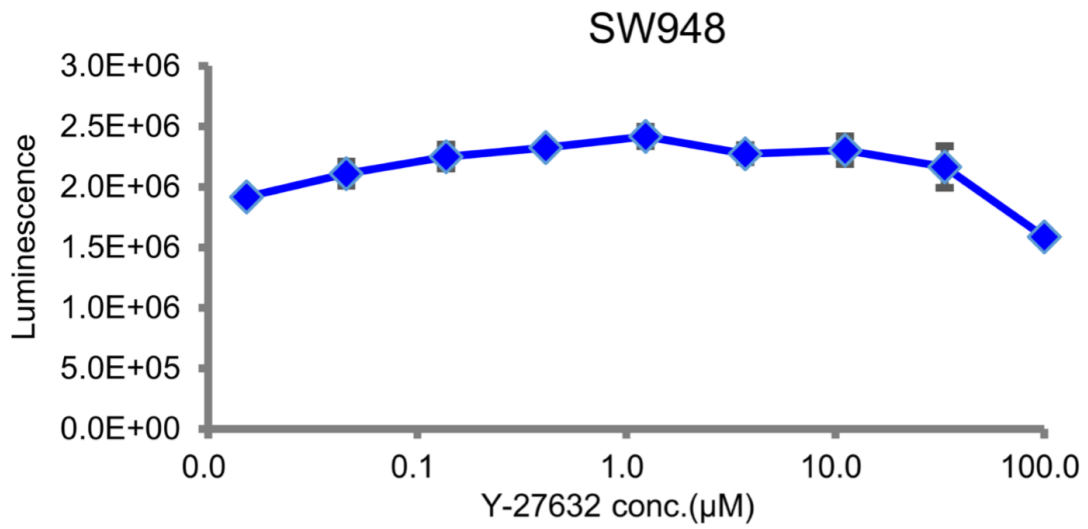


Figure 1-9: Effect of Y-27632 on cell survival on SW948

SW948 was seeded in a low attachment plate and then treated with various concentrations of Y-27632 for 7 days. The viable cells were measured by a CellTiter-Glo 3D Cell Viability Assay. Data are shown as mean \pm SD ($n = 3$).

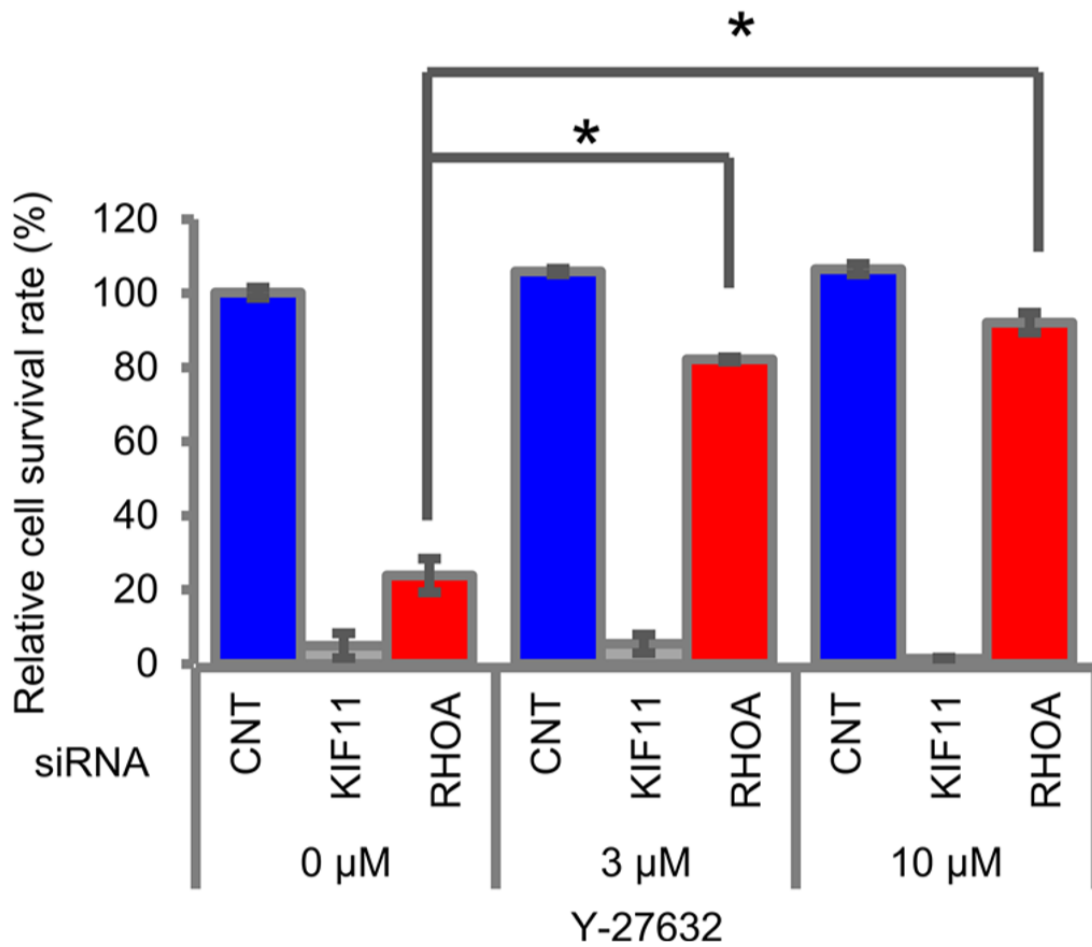


Figure 1-10: Restoration of cell survival by a ROCK inhibitor, Y-27632

SW948 was cultivated for 7 days with 3 μM or 10 μM of Y-27632. The relative cell survival rate is shown as a percentage of that in the control-siRNA-treated SW948 that was not treated with Y-27632.

Data are shown as mean ± SD ($n = 3$). Significance compared with the Y-27632 non-treated group

between *RHOA*-siRNA-treated groups was determined by Student's *t*-test. * $p < 0.05$.

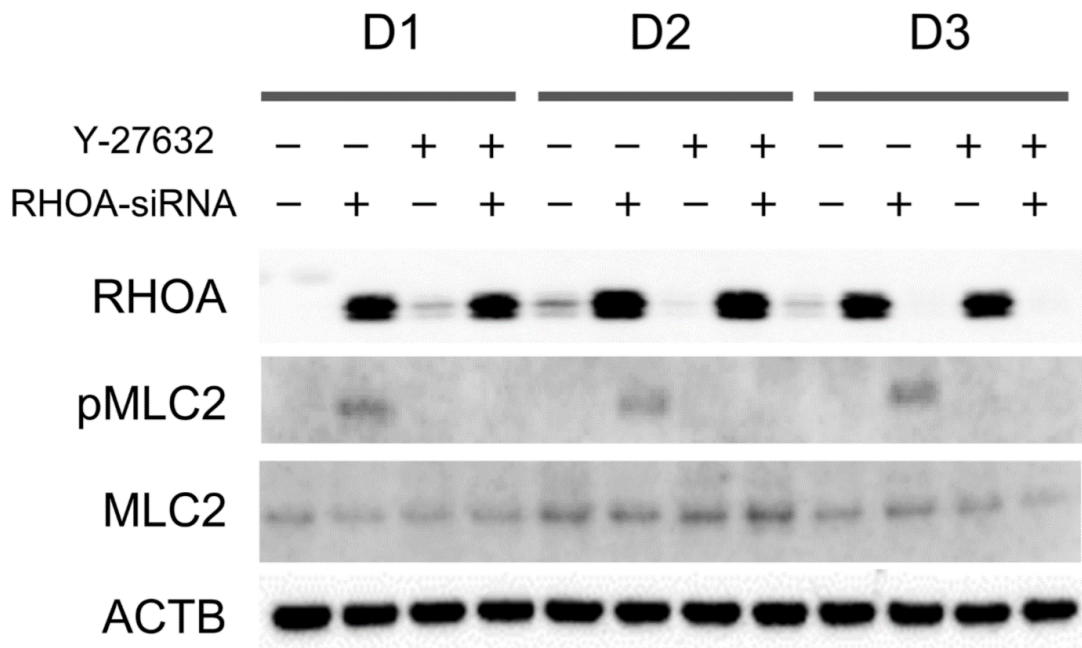


Figure 1-11: Suppression of MLC2 phosphorylation by a ROCK inhibitor

SW948 was seeded in a 6-well plate and then *RHOA*-siRNA or 10 μ M of Y-27632 was added. Proteins were harvested on days 1, 2, and 3 after siRNA treatment. The protein expression levels were detected using western blotting.

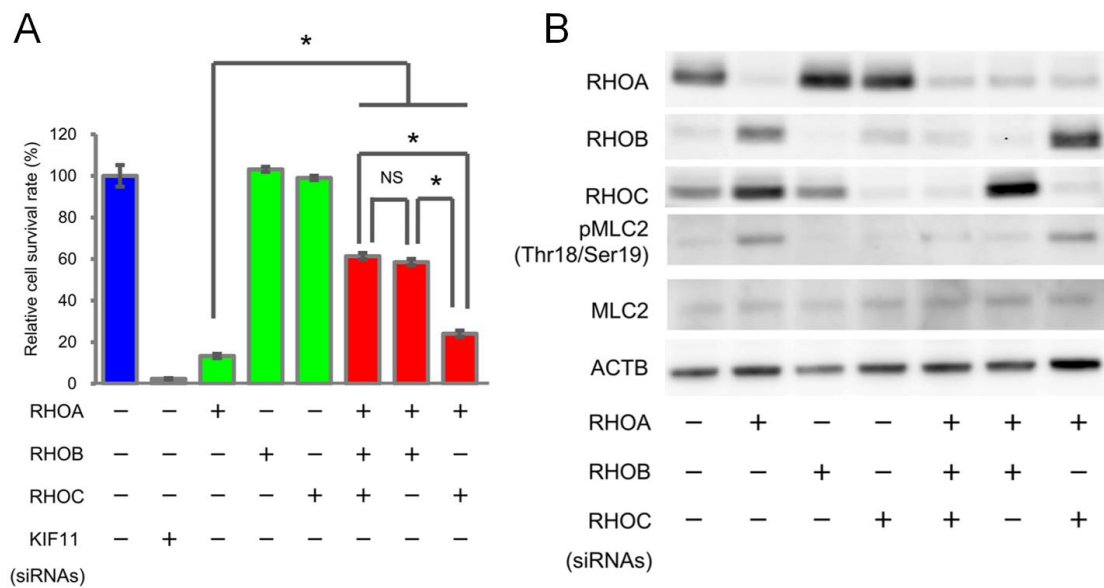


Figure 1-12: Activation of ROCK signaling by *RHOA* knockdown in SW948

(A) Restoration of cell survival by *RHOB/RHOC*-siRNAs. SW948 was cultivated for 7 days with *RHOA*-siRNA (1 μ M) and/or *RHOB*-siRNA (1 μ M) and/or *RHOC*-siRNA (0.2 μ M). Cell survival rate of obtained transfectants was evaluated as described in Figure 1-5. Data are shown as mean \pm SD ($n = 3$). Significant differences between *RHO*-siRNA-treated groups were determined by Student's *t*-test.

* $p < 0.05$. (B) Protein expression of cells tested in (A).

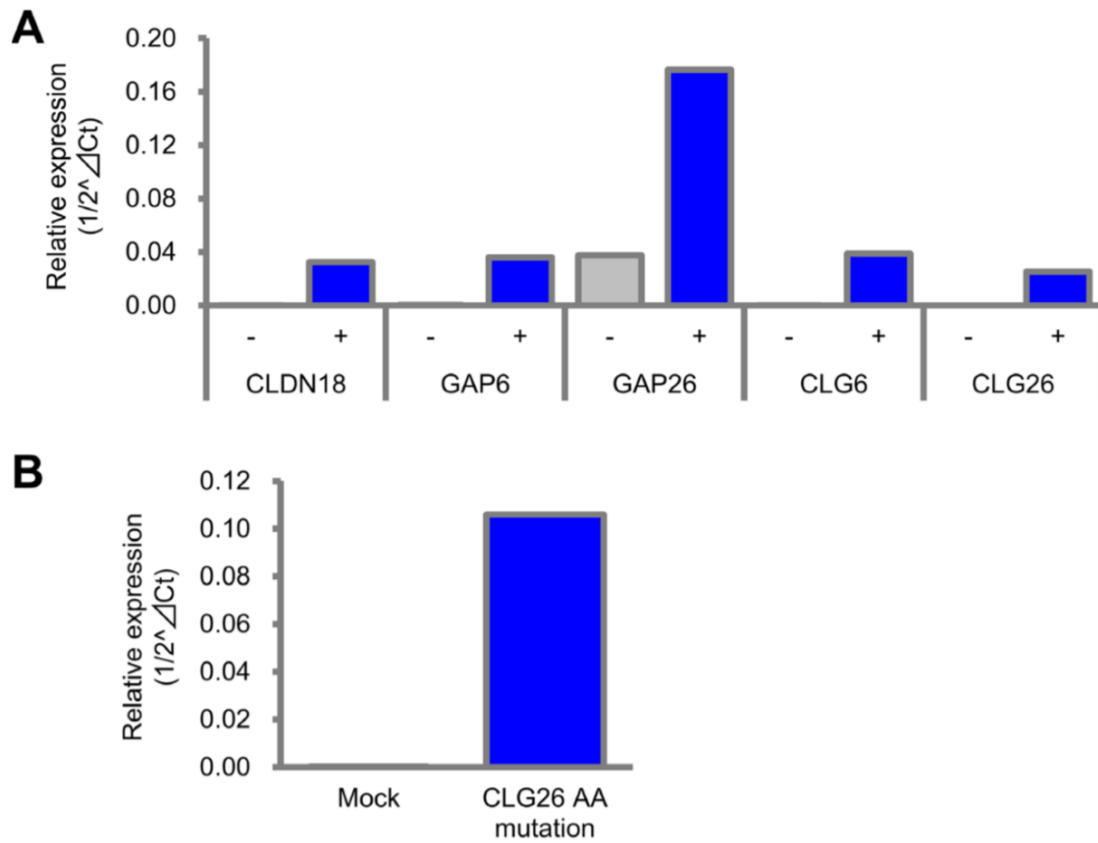


Figure 1-13: mRNA expression of each transfectant of *CLDN18*, *GAP6*, *GAP26*, *CLG6*, and *CLG26* (A) and *CLG26* with GAP domain AA mutations (B) in SW948

Cells were seeded in a 6-well plate, and after 2 days incubation, mRNAs were eluted and quantitative RT-PCR was performed using each primer. Values obtained in quantitative RT-PCR were normalized with *RPS18*.

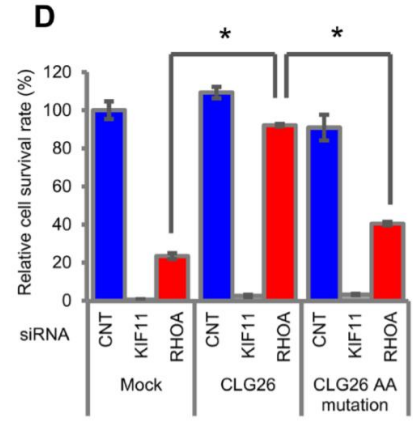
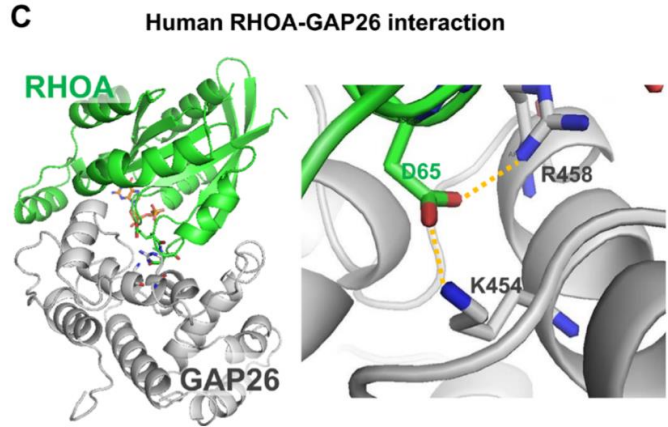
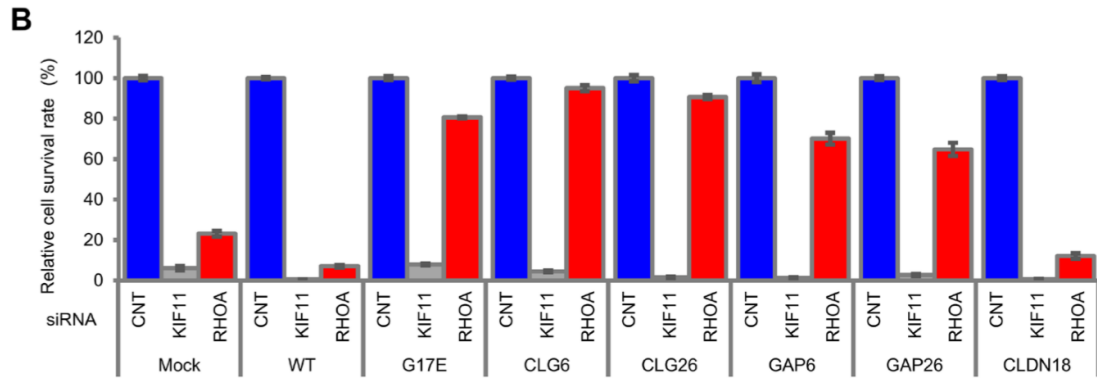
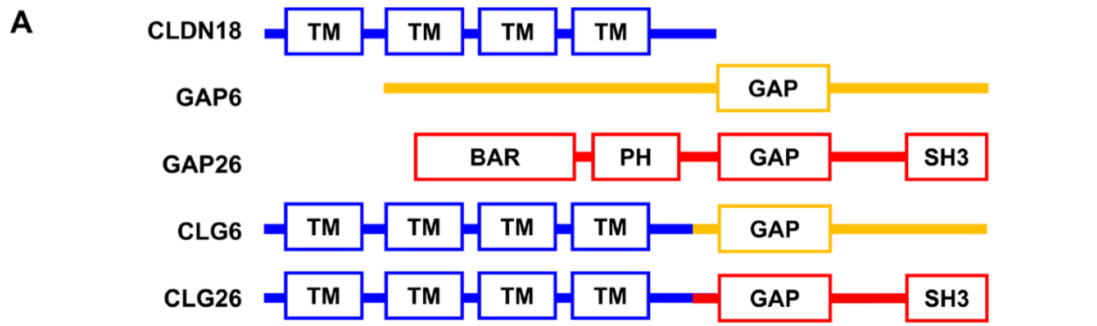


Figure 1-14: Cell survival promoted by *CLG* fusions in SW948

(A) Domain structure of *CLG* fusions. (B) Restoration of cell survival by *CLG* fusions. Cell survival rate was evaluated as described in Figure 1-8C. (C) Structure of RHOA and GAP complex inferred from homology modeling of PDB: 1TX4. RHOA in green and GAP26 in silver are shown in stick form. Hydrogen bonds are shown by an orange dotted line. A close-up (right) of hydrogen bonds in the overall model (left) is shown. (D) Reduction in cell survival activity by GAP domain AA mutations.

SW948 was transfected with K454A/R458E double-mutated *CLG26*. Cell survival rate of each obtained transfectant was evaluated as described above. The relative cell survival rate is shown as a percentage of that in the mock transfectants treated with control-siRNA. Data are shown as mean \pm SD ($n = 3$). Statistical significance of the *CLG26* group compared with *RHOA*-siRNA-treated groups was determined by Student's *t*-test. $*p < 0.05$.

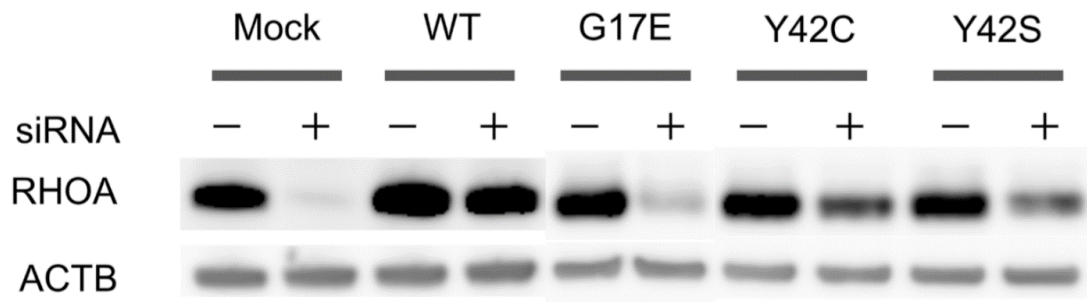


Figure 1-15: Expression analysis of MKN74 transfectants

Cells were seeded in a 6-well plate and then *RHOA*-siRNA was added. Proteins were eluted on day 2, and RHOA protein expression was detected by western blotting.

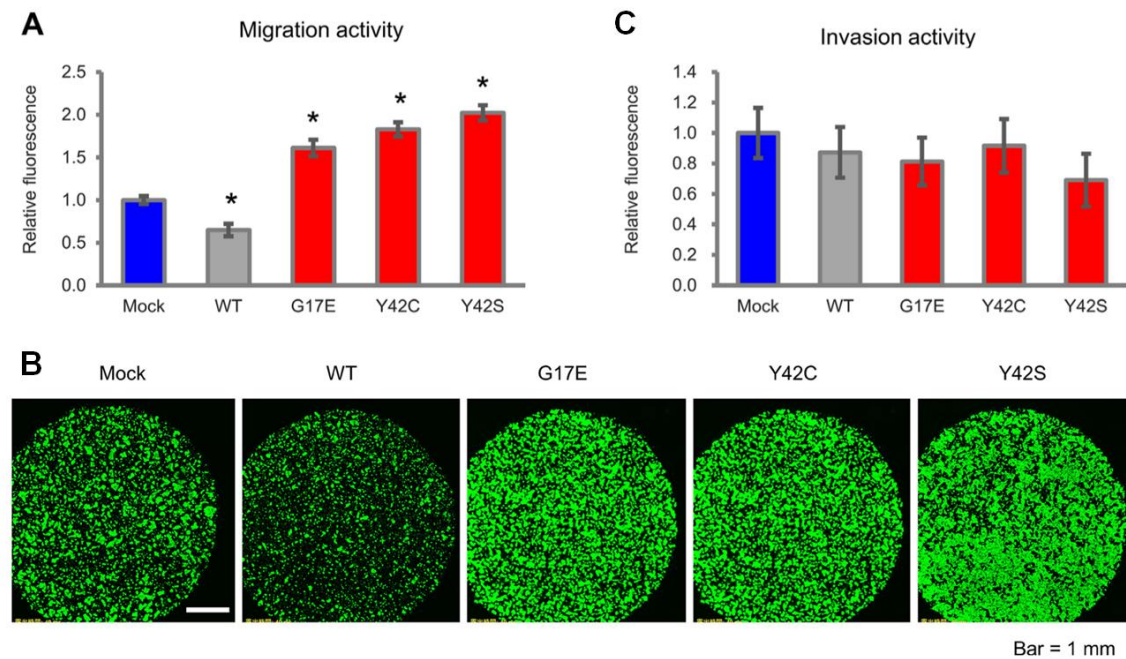


Figure 1-16: Cell motility in MKN74 cells with *RHOA* mutations

(A) Cell motility in an uncoated chamber and (C) in a Matrigel-coated chamber was measured 48 hrs after plating with MKN74 transfectants of *RHOA* mutations. The migrating cells were stained with calcein AM, and the fluorescence was measured by a plate reader. Data are shown as mean \pm SD ($n = 3$). (B) 48 hrs after cell seeding, fluorescence microscopy was used to detect calcein-incorporated migrating cells. Representative images of each transfectant ($n = 3$) are shown. Scale bar shows 1 mm. Statistical significance compared with the mock group was determined by Student's *t*-test. $*p < 0.05$. Methods of calculating invasion activity are described in Materials and Methods.

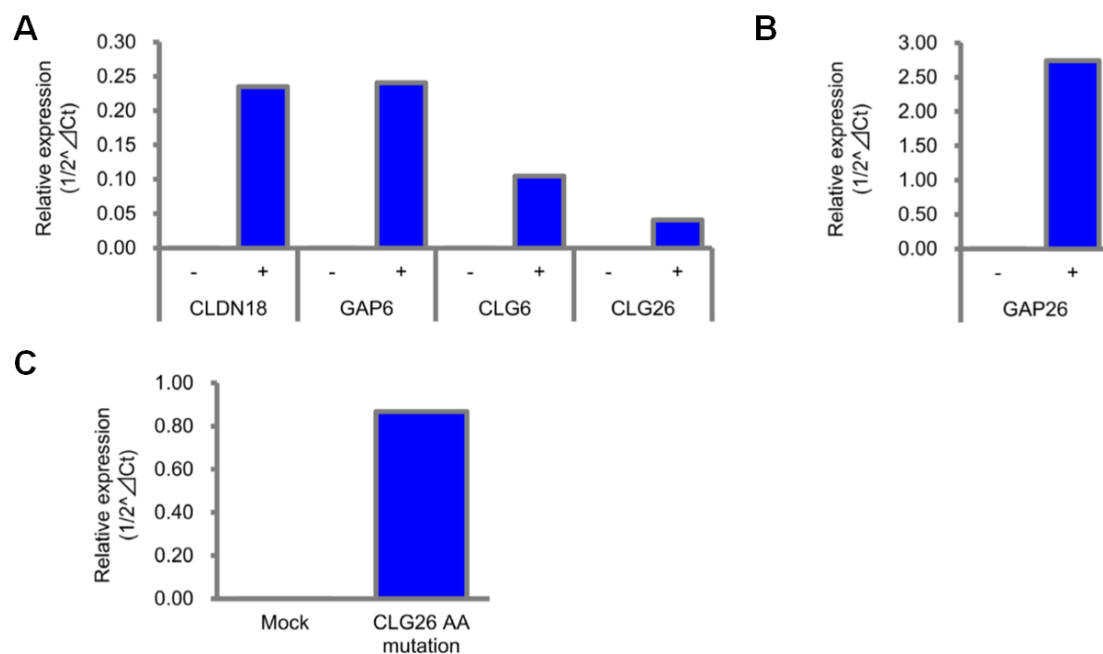


Figure 1-17: mRNA expression of each transfectant of *CLDN18*, *GAP6*, *GAP26*, *CLG6*, and

***CLG26* (A, B) and *CLG26* with GAP domain AA mutations (C) in MKN74**

Cells were seeded in a 6-well plate, and after 2 days incubation, mRNAs were eluted and quantitative

RT-PCR was performed using each primer. Values obtained in quantitative RT-PCR were normalized

with *RPS18*.

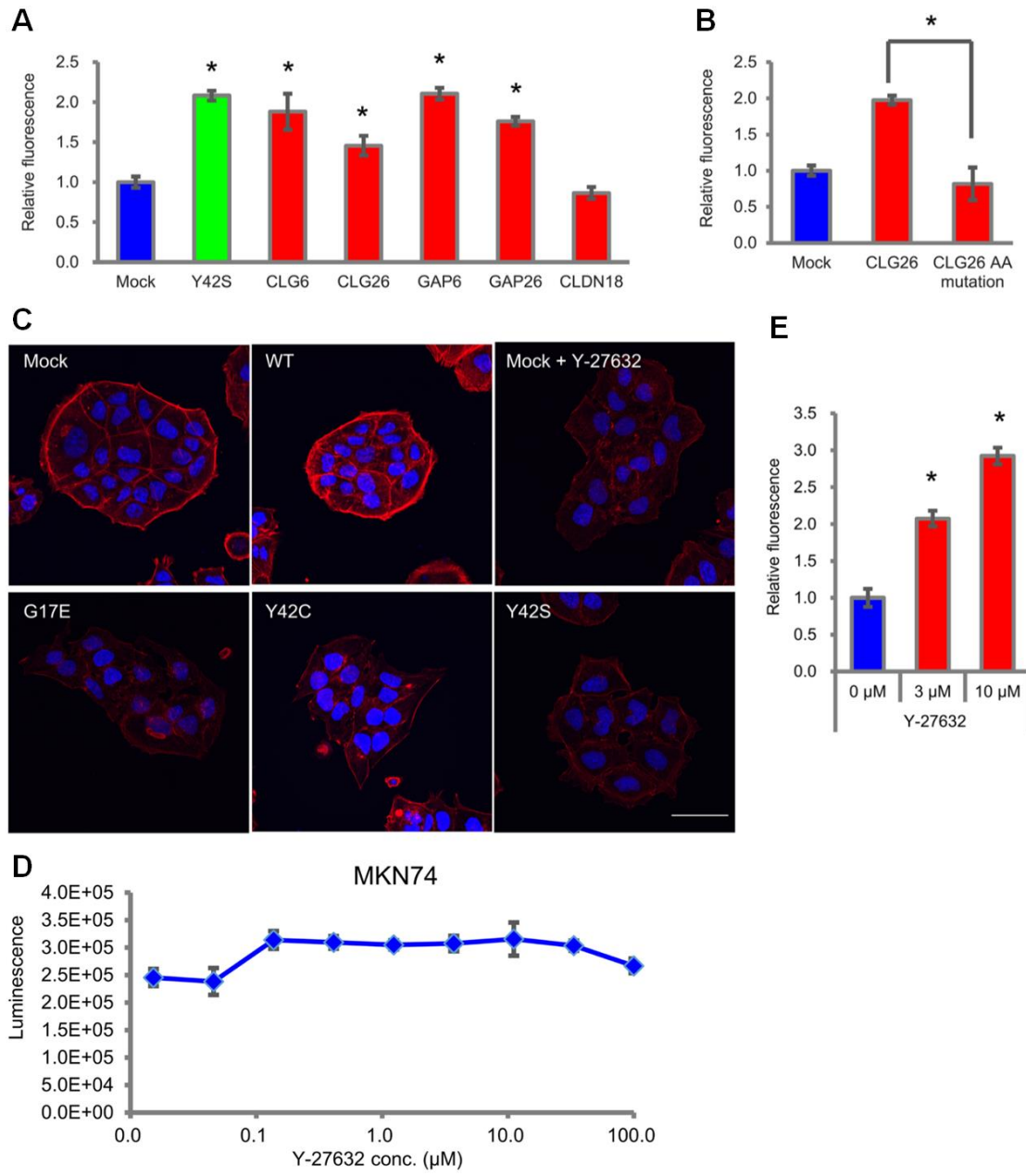


Figure 1-18: Cell motility in MKN74 cells with CLG fusions

(A) Migration activity of MKN74 transfectants with *CLG* fusions, *GAPs*, and *CLDN18*. Cells were seeded in an uncoated chamber and migrated cells were stained with calcein AM. Data are shown as mean \pm SD ($n = 3$). Statistical significance compared with the mock group was determined by Student's *t*-test. $*p < 0.05$. (B) Reduction of cell migration by GAP domain AA mutations. MKN74 was transfected with K454A/R458E double-mutated *CLG26*. Migration activity was evaluated as described above. (C) Actin stress fibers in MKN74 transfectants with *RHOA* mutations. Mock cells were treated with 10 μ M of Y-27632. Actin stress fibers were stained with Rhodamine Phalloidin, and DAPI was used for nuclear staining. Stained cells were analyzed with confocal fluorescence microscopy. Representative images from three independent fields of view are shown. Scale bar shows 50 μ m. (D) MKN74 was seeded in a cell culture plate and then treated with various concentrations of Y-27632 for 4 days. The viable cells were measured by a CellTiter-Glo 3D Cell Viability Assay. Data are shown as mean \pm SD ($n = 3$) (E) Migration activity promoted by a ROCK inhibitor in MKN74 transfectants. Cells were seeded in an uncoated chamber and cultivated for 48 hrs with 3 μ M or 10 μ M of Y-27632. Migration activity was measured as described above. Data are shown as mean \pm SD ($n = 3$). Statistical significance compared with the non-treated group was determined by Student's *t*-test. $*p < 0.05$.

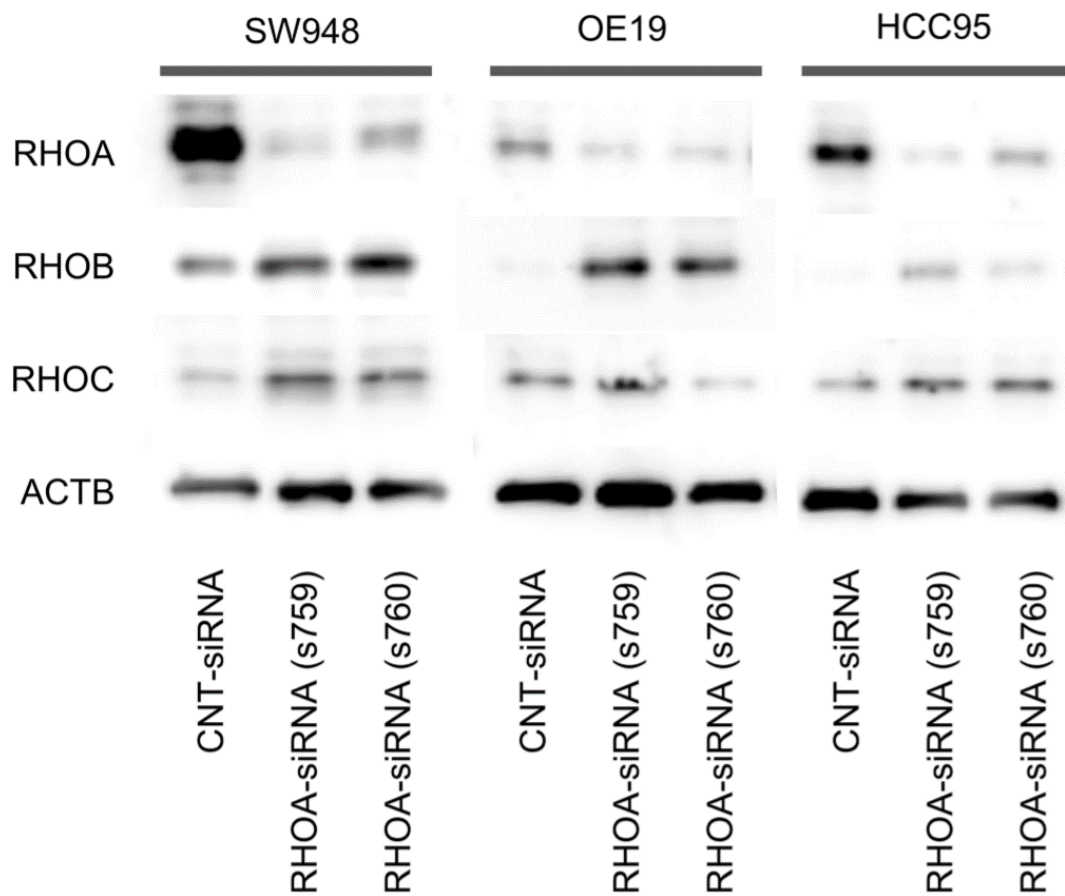


Figure 1-19: Feedback upregulation of RHOB and RHOC proteins after *RHOA* knockdown

Each cell line was seeded in a 6-well plate and then *RHOA*-siRNA was added. Proteins were harvested on day 2 after siRNA treatment. The protein expression levels were detected using western blotting.

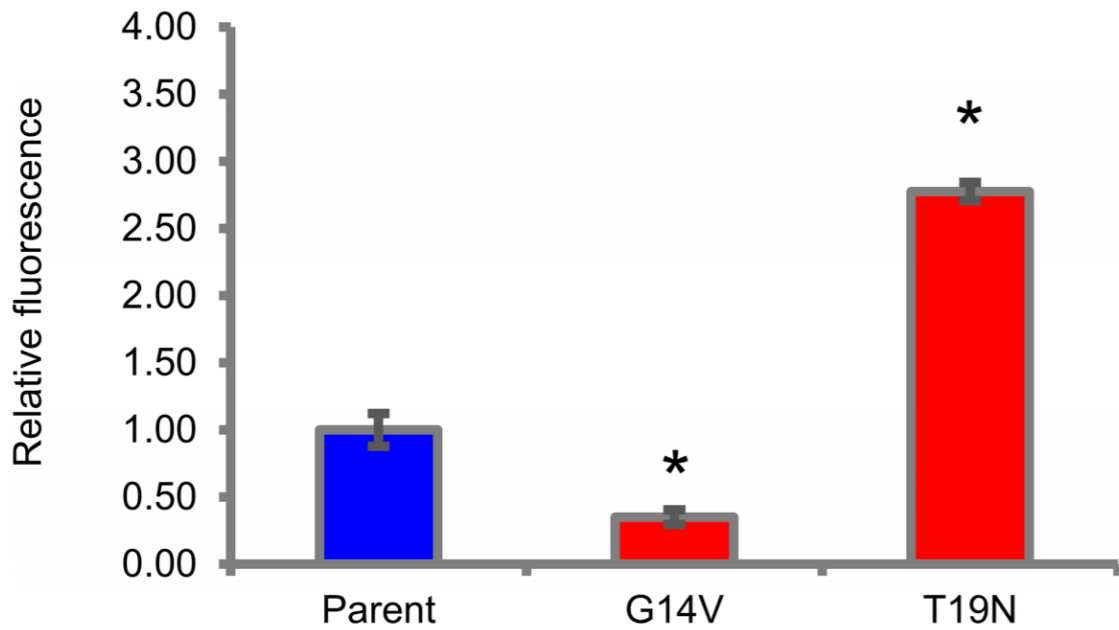


Figure 1-20: Migration activity in MKN74 transfectants of G14V (dominant-active) and T19N (dominant-negative)

Cells were seeded in an uncoated chamber and migrated cells after 48 hrs were stained with calcein

AM. Data are shown as mean \pm SD ($n = 3$). Statistical significance compared with the parent MKN74

group was determined by Student's *t*-test. * $p < 0.05$.

Chapter 2

Difference in morphology and interactome profiles between orthotopic and subcutaneous gastric cancer xenograft models

Abstract

In xenograft models, ORT engraftment is thought to provide a different tumor microenvironment compared with SC engraftment. We attempted to characterize the biological difference between OE19 (adenocarcinoma of the gastroesophageal junction) SC and ORT models by pathological analysis and CASTIN analysis, which is a novel method developed to analyze the tumor-stroma interactome framework. In SC models, SCID mice were inoculated subcutaneously with OE19 cells, and tumor tissues were sampled at 3 weeks. In ORT models, SCID mice were inoculated under the serosal membrane of the stomach wall, and tumor tissues were sampled at 3 and 6 weeks after engraftment. Results from the two models were then compared. Histopathologically, the SC tumors were well circumscribed from the adjacent tissue, with scant stroma and the formation of large ductal structures. In contrast, the ORT tumors were less circumscribed, with small ductal structures invading into abundant stroma. Then we compared the transcriptome profiles of human tumor cells with the mouse stromal cells of each model by species-specific RNA sequencing. With CASTIN analysis, we successfully identified several interactions that are known to affect the tumor microenvironment as being selectively enhanced in the ORT model. In conclusion, pathological analysis and CASTIN analysis revealed that ORT models of OE19 cells have a more invasive character and enhanced interaction with stromal cells compared with SC models.

Introduction

Cancer xenograft models are widely used to study tumorigenesis or to examine response to therapy. Xenograft models are classified as SC or ORT, and researchers select models according to the objective of a study. SC models are often used to assess antitumor activity because of their high reproducibility and ease of monitoring cancer growth. On the other hand, ORT models are thought to reproduce some aspects of the cancer microenvironment and are thought to be more clinically relevant than SC models [91-95]. ORT models emulate a number of important biological features of cancer progression [96, 97], metastasis [98-100], and sensitivity to therapy [101-103]. These differences between models might be associated with a difference in the cancer microenvironment, but detailed mechanisms are still unclear. Therefore, the comparison between SC model and ORT model in both macroscopic and microscopic aspects is necessary.

My collaborator Dr. Komura previously reported CASTIN (CAncer-STromal INteractome) analysis, a novel framework that evaluates the cancer-stromal interactome [104] and can be used to understand the relationship between a cancer and its microenvironment. As there is an approximately 15% sequence difference between human and mouse exon sequences [105], a simultaneous transcriptome analysis of cancer and stroma can be achieved using RNA sequencing data from xenografts [106]. CASTIN summarizes the interactome status between cancer and stroma by

quantitatively evaluating the ligand-receptor expression and comprehensively visualizing that expression to identify critical cancer microenvironment interactions. In a previous report, CASTIN was applied to a data set from pancreas ductal adenocarcinoma, and that individual cancer was successfully characterized in terms of its cancer-stroma relationships [104]. In this study, I histopathologically compared SC models and ORT models of a cell line that originated from adenocarcinoma of the gastroesophageal junction, OE19. Then I applied CASTIN to investigate the difference in cancer-stroma interactions.

Materials and Methods

Cell culture

OE19 [107], a cell line of adenocarcinoma from the gastric cardia/esophageal gastric junction, was purchased from the ECACC (No. 96071721). The cells were maintained in RPMI 1640 medium (Sigma-Aldrich) supplemented with heat-inactivated fetal bovine serum (FBS; Sigma-Aldrich), 10 mM HEPES (Gibco; Thermo Fisher), 1 mM sodium pyruvate (Gibco; Thermo Fisher) and 2.5 g/l D-glucose (Sigma-Aldrich), and cultured at 37°C in a 5% CO₂ incubator.

Animals

Six-week-old male C.B-17/lcr-scid/scid Jcl severe combined immune-deficient (SCID) mice were provided by CLEA Japan. All animals were housed in a specific pathogen-free environment under controlled conditions (temperature, 20°C–26°C; humidity, 30%–70%; light/dark cycle, 12/12 hr) and were allowed to acclimatize and recover from shipping-related stress for more than 7 days prior to the study. Chlorinated water and irradiated food were provided ad libitum. The health of the mice was monitored by daily observation. All animal experiments were performed at Chugai Pharmaceutical Co., Ltd. The experiments were reviewed and approved by the Institutional Animal Care and Use Committee at Chugai Pharmaceutical Co., Ltd.

Xenograft models

For the SC implantation model, 1×10^5 cells were suspended in 200 μL of RPMI 1640 medium containing 50% Matrigel (Corning) and injected subcutaneously into the right flank of mice. For the ORT implantation model, the mice were inoculated with 1×10^5 cells suspended in 20 μL of RPMI1640 medium containing 50% Matrigel. A surgical incision was made in the abdomen under isoflurane anesthesia, and the cells were inoculated under the serosal membrane of the ventral stomach wall. The tumors were sampled at 3 weeks after inoculation. For the ORT model, an additional time point was set at 6 weeks. For the SC model, no additional time points were set because there was notable necrosis in the center of the tumor after 4 weeks. At necropsy the animals were sacrificed under isoflurane inhalation anesthesia by exsanguination from the abdominal artery and grossly examined.

Tumor tissue sampling

ORT transplantation is not always successful, so it is necessary to select the cases that are appropriate for analysis. For the current study, 4 cases each were selected for both time points. Two cases were subjected to histopathology, and 2 cases were subjected to RNA analysis. For SC transplantation, 2 cases were used for histopathological examination, and 3 cases were used for RNA analysis.

Histopathological analysis

The tumor tissues were fixed in 10% neutral buffered formalin for 24 hrs and embedded into paraffin by a routine method. The tissues were sectioned at a thickness of 3–4 μm , and each tissue was subjected to hematoxylin and eosin (HE) and Masson's trichrome staining. The slides were examined under light microscopy.

Transcriptome sequencing

Tumors were embedded in O.C.T. compound (Sakura Finetek) and frozen in liquid nitrogen. Cryosections were prepared and suspended in TRIzol reagent (Thermo Fisher), and total RNA was extracted according to the manufacturer's instructions. One microgram of total RNA was used to prepare a transcriptome sequencing library for each tumor sample using a TruSeq stranded mRNA Library Prep Kit (Illumina) according to the manufacturer's directions. The libraries were sequenced in 100 bp paired-end reads on a HiSeq 2500 sequencer (Illumina). Four libraries were loaded into the single lane of an Illumina flow cell, producing more than 30 million paired-end reads for each sample. Sequenced reads were then mapped to all RefSeq transcripts of the human (hg38 coordinates) and mouse (mm10 coordinates) using Bowtie 1.1.2, allowing up to one mismatch, and reads mapped to both species or to multiple genes were discarded. The remaining reads were used to estimate the gene expression profile of human cancer cells and mouse stroma cells according to the methods in my

previous report [104].

Analysis of transcriptomic data

For unsupervised hierarchical clustering analysis, a Euclidean distance calculation and Ward's linkage were performed for the 500 most variable genes, defined by the coefficient of variation calculated across all samples using the Strand NGS software (ver. 2.6, Agilent Technologies). Differentially expressed genes (DEGs) between SC and ORT models were selected using an empirical criterion of more than 3-fold change. To gain an overview of gene pathway networks, KEGG (Kyoto Encyclopedia of Genes and Genomes) analysis was performed using an online KEGG automatic annotation server (<https://david.ncifcrf.gov/summary.jsp>). The KEGG pathways identified were ranked by *p*-value.

CASTIN analysis

Interactome profiles were visualized by a modified version of the original CASTIN [97]. In the modified version, cancer ligand dependency *X* and stromal receptor dependency *Y* for each interaction were calculated as follows:

$$X = LC / (LC + LS)$$

$$Y = RS / (RC + RS)$$

where LC , LS , RC , and RS are normalized gene expression levels of ligand gene of human (cancer), ligand gene of mouse (stroma), receptor gene of human (cancer), and receptor gene of mouse (stroma), respectively.

The signal strength of ligand H and receptor V were calculated as follows:

$$H = \ln(\max_{k \in \{C,S\}} Lk),$$

$$V = \ln(\max_{k \in \{C,S\}} Rk).$$

These four interactome evaluation indices (X , Y , H , V) were visualized for each interaction as a rhombus in the 2D-plane at position (X, Y) , and the horizontal and vertical diagonal lengths were proportional to H and V , respectively. Then each interaction falls into one of the following four zones.

- 1) C-S zone ($X \geq 0.5$ and $Y \geq 0.5$): interactions in this zone indicate that input signals are dominantly created by cancer and exclusively transmitted to stroma. Signal transduction takes place only when both cancer and stromal cells exist, and thus I call it a “mutually dependent interaction.”
- 2) S-C zone ($X < 0.5$ and $Y < 0.5$): interactions in this zone also indicate mutually dependent interactions, but the direction of signal transduction is opposite (stroma to cancer).
- 3) C-C zone ($X \geq 0.5$ and $Y < 0.5$): input signals are created by cancer and transmitted mainly to cancer itself. Thus interactions in this zone indicate cancer autoregulation.
- 4) S-S zone ($X < 0.5$ and $Y \geq 0.5$): a counterpart to the C-C zone.

Interactions in this zone indicate microenvironment autoregulation

Results and Discussion

Necropsy was performed in the SC and ORT models of OE19. In SC models, tumor formation was confirmed in all animals. In ORT models at 3 weeks, tumor formation at the inoculation site in the stomach was observed (Table 2-1). At 6 weeks, in addition to the changes at the inoculation site, there was infiltration of the tumors into other areas of the stomach and also metastasis in the pancreaticoduodenal lymph nodes, which shows that the area of tumor growth had expanded compared with that at 3 weeks (Table 2-1).

Next the area of inoculation was examined histopathologically in SC models at 3 weeks and ORT models at 3 and 6 weeks. With SC models, the SC mass was relatively well circumscribed from the surrounding tissue, and tumor growth was mainly expansive. The tumor cells formed large ductal structures with scant stroma (Figure 2-1A). The ductal wall was relatively thick, and the tumor cells were often multilayered (Figure 2-1B). With the ORT models, there was also tumor formation in the inoculation area, but the tumor cells formed smaller ducts that invaded into abundant stroma, and the growth was mainly invasive (Figure 2-1A). The ductal wall consisted of a single layer of tumor cells (Figure 2-1B). At 6 weeks in the ORT model, the monolayered small ducts were more densely packed, with less stroma than at 3 weeks (Figure 2-1A, B). Vascular invasion was noted in the surrounding tissues (Figure 2-2). Thus, there was a striking difference in growth patterns and the amount of stromal

tissues between the 2 models. In clinical DGC, small clustered tumor cells are scattering into stromal tissues, so the histopathological features of ORT model were similar to clinical DGC than that of SC model. Notably, the invasive growth in the ORT model was thought to show that there was active interaction between the tumor and stromal cells, so the OE19 ORT model was thought to be suitable for analysis of cancer-stroma interactions. There is little information concerning the difference in the amount of stroma between SC and ORT models, but I speculate that this finding is at least common among some tumors, because similar results have been described in a xenograft model of pancreatic cancer [108]. Additional studies are considered necessary to further elucidate this matter.

In order to analyze the interactions between cancer cells and their microenvironment, I performed RNA sequencing of each xenograft model and simultaneously obtained OE19 (human) and stroma (mouse) transcriptome data (Figure 2-3A). Before CASTIN analysis, I compared the gene expression profiles of OE19 cells between SC models and ORT models. Unsupervised hierarchical clustering showed that the expression profiles of SC-SC and ORT-ORT samples were consistent and clustered together into distinct groups (Figure 2-3B). The difference in expression pattern between SC and ORT models at 3 weeks is represented in the scatter plot in Figure 2-3C, for which DEGs were chosen using an empirical criterion of more than 3-fold change. Seventy-seven genes were highly expressed in SC models, and 168 genes were highly expressed in ORT models. To identify activated pathways in each model, DEGs were subjected to KEGG pathway enrichment analysis. The significant

pathways with the highest representation are shown in Table 2-2. In the SC models, I could not find significantly enhanced pathways, but in the ORT models, I found that several signaling pathways including MAPK signaling, focal adhesion, and ECM-receptor interaction were enhanced. These data confirm that the OE19 status in SC and ORT models is different not only in the pathological analysis described above but also at the transcriptome level. It was reported that ECM related components are unregulated in DGC compared with IGC [109]. Therefore, ORT model showed the features of clinical DGC, but further analysis for the downstream signaling and other pathways would be needed.

To understand the difference in cancer-stroma interaction between SC and ORT models, I applied CASTIN to the data set of each model. Interactome profiles of SC and ORT models at 3 weeks were visualized in Figure 3-3D. Each data point on the plot represents an individual interaction, and the positions indicate the role of the interaction in cancer-stroma relationships. Interactions that direct a cancer ligand to a stromal receptor were plotted in the upper right zone (C-S zone), and those that direct a stromal ligand to a cancer receptor were plotted in the bottom left zone (S-C zone). Many interactions were plotted in the C-S zone and S-C zone for both SC and ORT models. To focus on interactions that were selectively enhanced in each model, I chose ligands or receptors that were included in the DEGs designated by the OE19 expression profiles (shown in dark colors in the CASTIN plots). In the SC model, 10 ligands or receptors included in the DEGs of the OE19 expression profiles were chosen, but none of their interactions were plotted in the C-S zone or S-C zone. On the

other hand, in the ORT model, 44 ligands or receptors included in the DEGs of the OE19 expression profiles were chosen, and the interactions GAST-CCKBR, EDN1-EDNRB, CXCL3-CXCR2, CYR61-ITGB3, and DKK1-LRP6 were plotted in the C-S zone, so these interactions were thought to affect connections from cancer to stromal cells. The interaction TNFSF12-TNFRSF12A was plotted in the S-C zone and was therefore thought to affect connections from stromal to cancer cells. The ligand/receptor expression of OE19 cells in each model are compared in Figure 3-3E. Interestingly, most interactions detected in this study were well known to affect tumor migration or the microenvironment [108-116]. GAST is one of the specific interactions in ORT model, but it was reported that GAST was key regulator for the transformation of gastric enterochromaffin-like cells into DGC [117, 118]. These results indicate that CASTIN analysis could successfully identify several cancer-stroma interactions that may affect invasive growth of OE19 cells observed in the ORT model, and partial features of clinical DGC.

CASTIN provides a comprehensive view of cancer-stromal interactions and is useful to identify critical interactions in xenograft models. In this system, the expression profiles of stromal cells are obtained from whole mouse cells surrounding the xenograft tumors. Because the composition of mouse cells varied greatly between SC and ORT models in this study, it was difficult to choose interactions that affect the tumor microenvironment. By focusing on DEGs, I successfully identified several interactions that were selectively enhanced in ORT models. Even so, the accuracy of CASTIN

analysis would be maximized by combining transcriptional information of cancer and stromal cells, so now I plan to use CASTIN to analyze against gene-modified cells (overexpression or knockdown) that have been inoculated at the same site to understand the molecular function of genes in a heterogeneous cancer microenvironment.

Tables and Figures

Table 2-1: Extent of nodule formation and infiltration of tumor

Findings	Weeks after inoculation	
	3	6
Tumor, stomach		
Inoculation site	4	4
Infiltration, other areas*	0	4
Tumor, other organs		
Pancreaticoduodenal lymph node	0	2

There were 4 animals for each timepoint. Numbers indicate the number of animals with findings.

* Other areas include the small curvature and dorsal side of the stomach.

Table 2-2: Upregulated pathways in the ORT model

KEGG ID	Term	P-value	Genes
hsa04010	MAPK signaling pathway	7.52×10^{-7}	FGF19, PDGFA, CACNG4, NR4A1, HSPA1A, FLNA, DUSP5, DUSP1, JUN, HSPA6, HSPB1, RRAS, PLA2G4C, GADD45B, DUSP8
hsa04510	Focal adhesion	2.75×10^{-6}	CAV2, CAV1, LAMA3, FYN, PDGFA, JUN, TNC, COL6A1, THBS1, COL11A2, BIRC3, FLNA, MYL9
hsa05134	Legionellosis	2.86×10^{-5}	CXCL1, CXCL3, CXCL2, HSPA6, CXCL8, TLR4, HSPA1A
hsa04668	TNF signaling pathway	1.77×10^{-4}	CXCL1, CCL20, CXCL3, JUN, EDN1, CXCL2, CX3CL1, BIRC3
hsa05132	Salmonella infection	3.22×10^{-4}	CXCL1, CXCL3, JUN, CXCL2, CXCL8, TLR4, FLNA
hsa05205	Proteoglycans in cancer	1.77×10^{-3}	CAV2, CAV1, HSPG2, RRAS, TLR4, WNT11, MSN, THBS1, FLNA
hsa04512	ECM-receptor interaction	2.89×10^{-3}	LAMA3, TNC, HSPG2, COL6A1, THBS1, COL11A2
hsa04115	p53 signaling pathway	6.73×10^{-3}	BBC3, SERPINE1, SFN, THBS1, GADD45B
hsa04390	Hippo signaling pathway	6.95×10^{-3}	BMP2, CTGF, BBC3, SERPINE1, WNT11, AREG, LATS2

KEGG, Kyoto Encyclopedia of Genes and Genomes

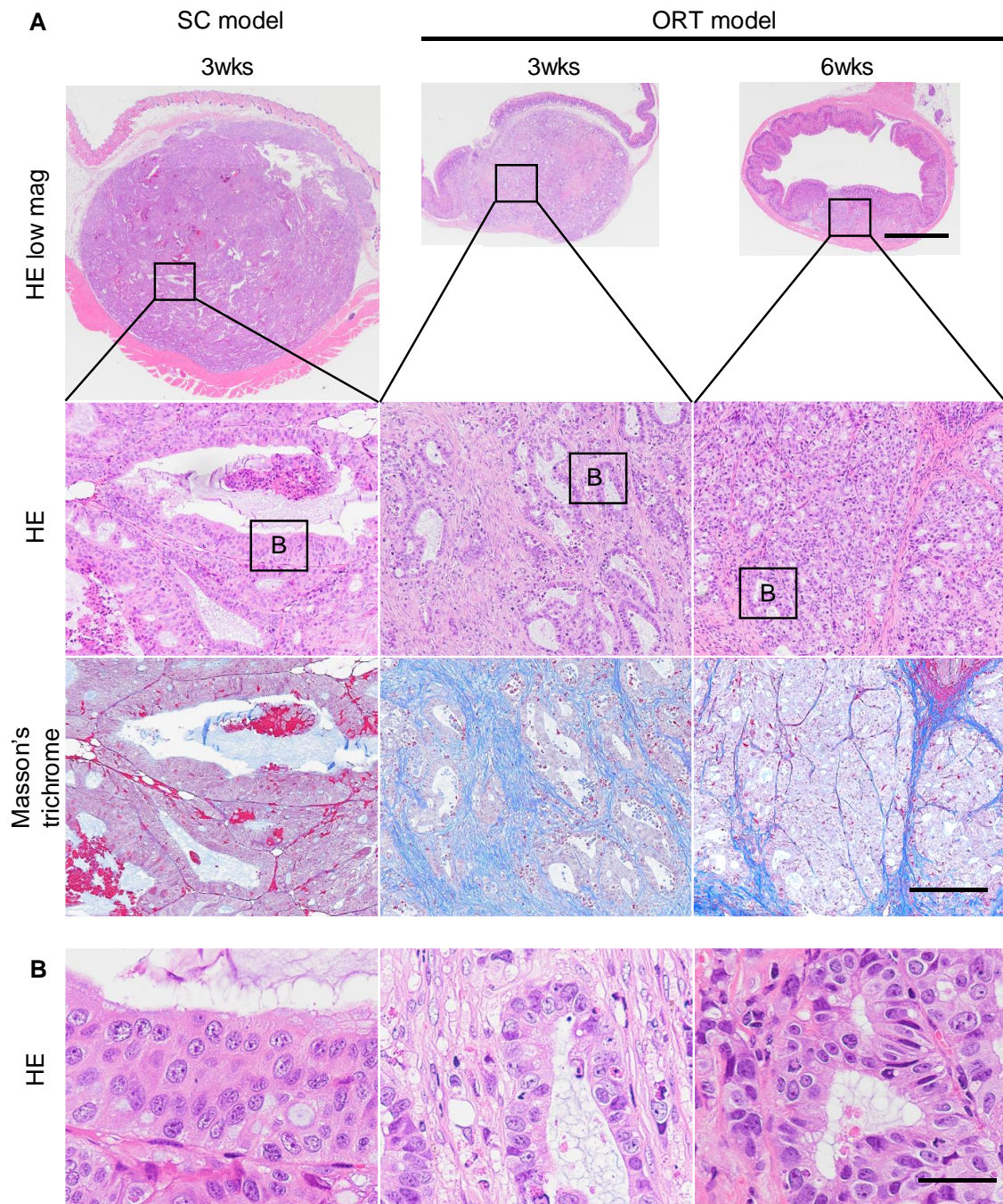


Figure 2-1: Morphological comparison of SC and ORT inoculation of OE19

(A) The images in HE low magnitude showed the whole tumor sections. The black square regions in HE low magnitude were used for HE and Masson's trichrome staining. At low magnitude, bar = 4000 μm ; in others, bar = 500 μm . (B) Analyzed area were shown in middle figures in A. Bar = 100 μm .

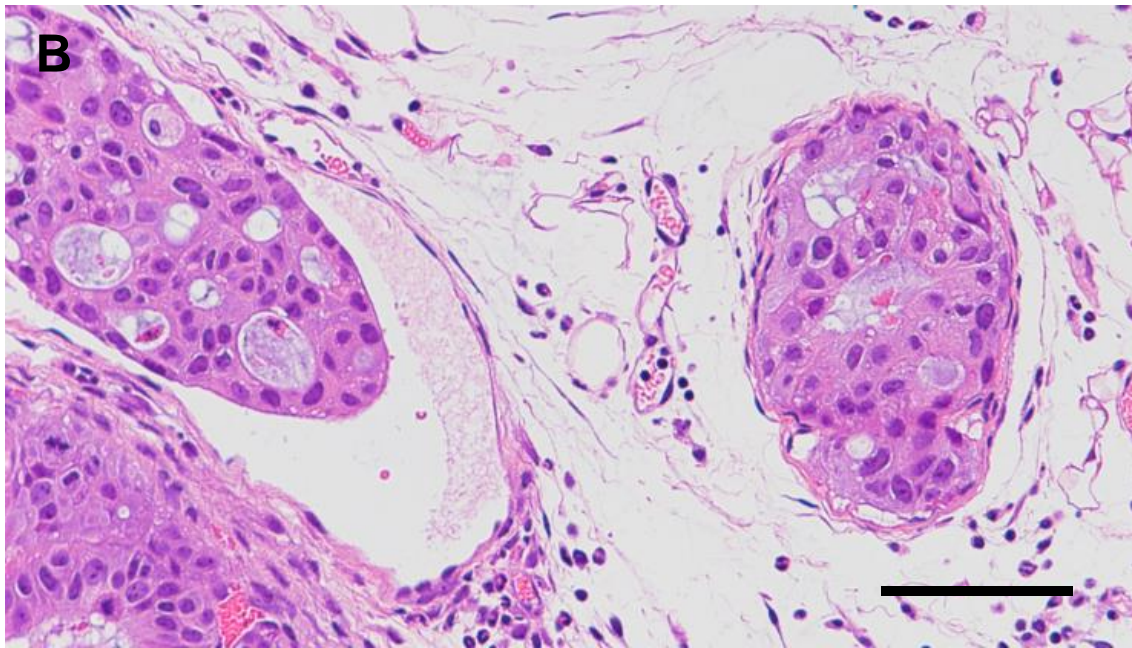
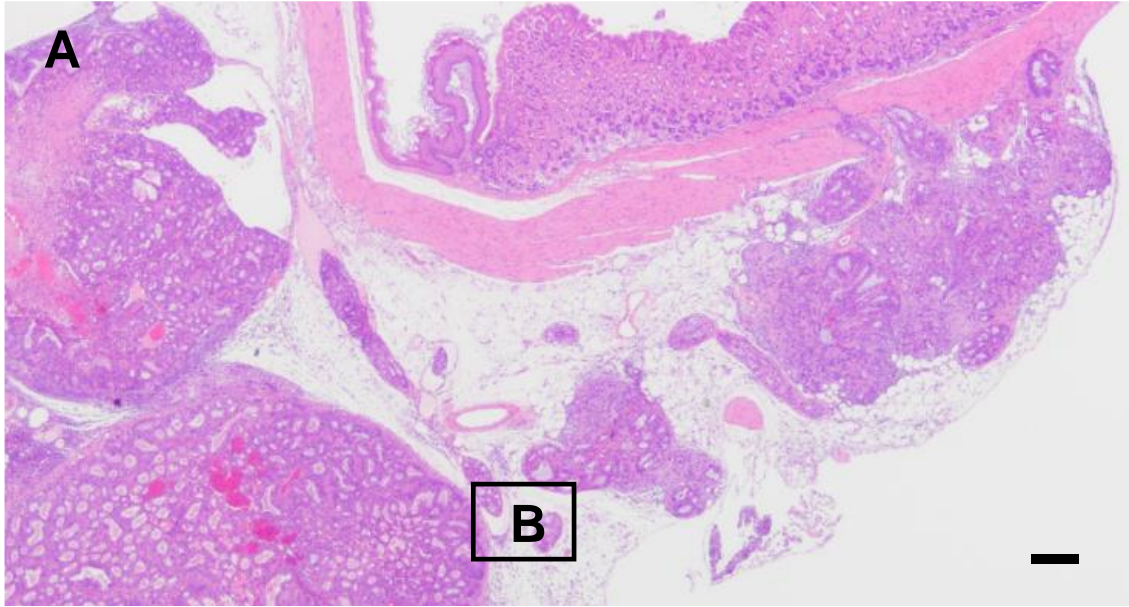


Figure 2-2: Vascular invasion of OE19 cells

The typical vascular invasion area in ORT model. B is the high magnitude image and analyzed area were shown in A as black square. HE stain. Bar = (A) 500 μm , (B) 200 μm

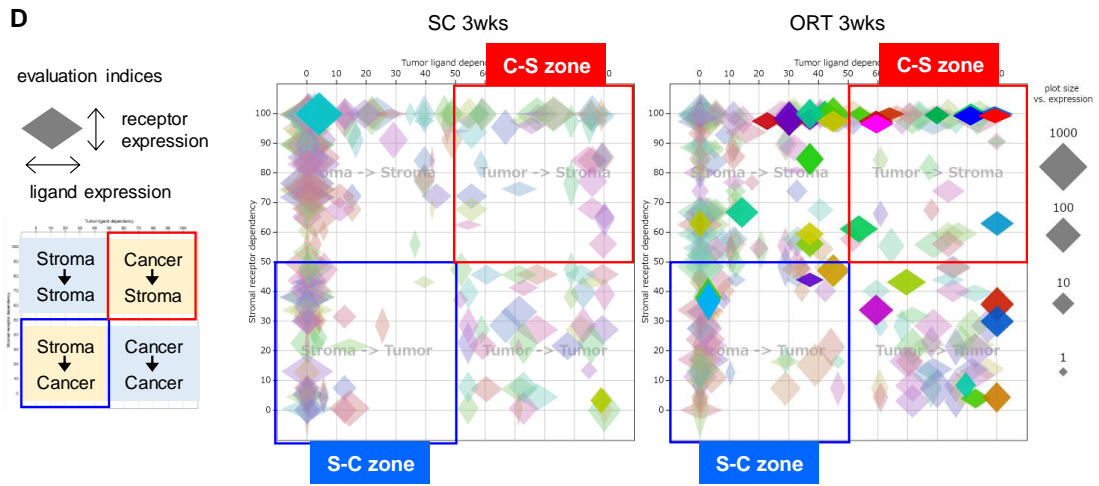
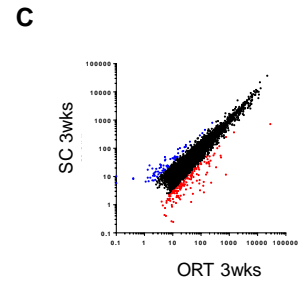
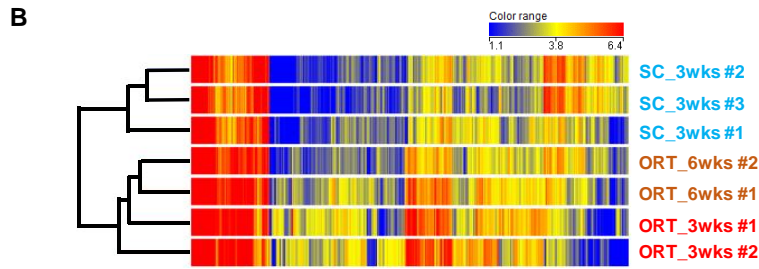
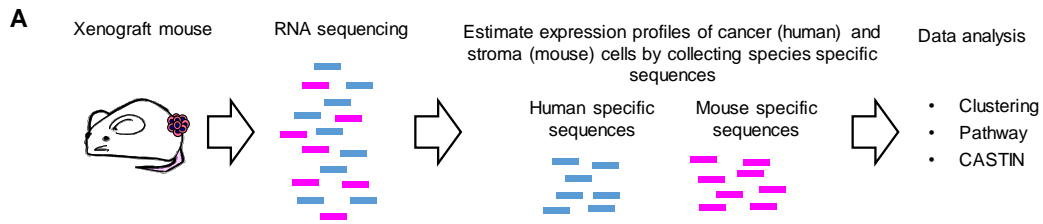


Figure 2-3: Interactome profiling of SC and ORT models

(A) Schematic workflow to estimate species-specific RNA expression profiles. (B) Hierarchical clustering of the differentially expressed genes across all samples. (C) Differentially expressed genes in SC and ORT at 3 weeks are plotted in a scatter plot. The values of the X and Y axes are the averaged normalized values in each group. Red dots indicate highly expressed genes with a fold change > 3 in the ORT model. Blue dots indicate highly expressed genes with a fold change > 3 in the SC model. (D) Interactome profiles of SC and ORT models at 3 weeks. Each data point represents an individual interaction. The size of the plot indicates the level of ligand or receptor expression. Interactions that connect a cancer ligand to a stromal receptor are plotted in the C-S zone (shown in red), while those that connect a stromal ligand to a cancer receptor are plotted in the S-C zone (shown in blue). (E) A comparison of the ligand/receptor expression of OE19. The corresponding interactions in each plot are shown in the same color.

Chapter 3

In vivo effects of mutant RHOA on tumor formation in an orthotopic inoculation model

Abstract

RHOA mutations are driver genes in DGCs, and I previously revealed that *RHOA* mutations contribute to cancer cell survival and cell migration through their dominant negative effect on ROCK signaling *in vitro*. However, how *RHOA* mutations contribute to DGC development *in vivo* is poorly understood. In the present study, the contribution of *RHOA* mutations to tumor morphology was investigated using an orthotopic xenograft model using the gastric cancer cell line MKN74, in which WT or mutated (Y42C and Y42S) *RHOA* had been introduced. When I conducted RNA sequencing to distinguish between the genes expressed in human tumor tissues from those in mouse stroma, the expression profiles of the tumors were clearly divided into a Y42C/Y42S group and a mock/WT group. Through gene set enrichment analysis, it was revealed that inflammation- and hypoxia-related pathways were enriched in the mock/WT tumors; however, cell metabolism- and cell cycle-related pathways such as Myc, E2F, oxidative phosphorylation and G2/M checkpoint were enriched in the Y42C/Y42S tumors. In addition, the gene set related to ROCK signaling inhibition was enriched in the *RHOA*-mutated group, which indicated that a series of events are related to ROCK inhibition induced by *RHOA* mutations. Histopathological analysis revealed that small tumor nests were more frequent in *RHOA* mutants than in the mock or WT group. In addition, increased blood vessel formation and infiltration of macrophages within the tumor mass were observed in the *RHOA* mutants.

Furthermore, unlike mock/WT, the *RHOA*-mutated tumor cells had little antitumor host reaction in the invasive front, which is similar to the pattern of mucosal invasion in clinical *RHOA*-mutated DGC. These transcriptome and pathological analyses revealed that mutated *RHOA* functionally contributes to the acquisition of DGC features, which will accelerate our understanding of the contribution of *RHOA* mutations in DGC biology and the development of further therapeutic strategies.

Introduction

DGCs, which are characterized by poorly differentiated adenocarcinoma that lack cell-cell adhesion and infiltrate into the stroma as single or clustered cells without glandular architecture [72, 119], show worse prognosis than the intestinal type [37, 72]. A characteristic genetic alteration of DGC is the *RHOA* missense mutation that is reported in 14-25% of DGC patients [43-45].

A previous report, which evaluated the clinicopathological features of 87 DGC patients by comparing the morphological features of *RHOA*-mutated and wild-type tumors, revealed a distinct permeative intramucosal growth pattern in the mutated tumors [120]. *RHOA* has various biological functions, such as actin stress fiber formation and cytokinesis [56, 57]. Recently, I revealed that *RHOA* mutations contribute to cancer cell survival and cell migration through their dominant negative effect on the ROCK pathway [121], but little is understood of how these functions are related to the clinicopathological features of DGC.

Thus, the present study was designed to evaluate the relationship between the features of DGC and *RHOA* mutations *in vivo*. To this end, I first considered which model was most suited for the evaluation of the DGC features. ORT inoculation is reported to be more likely to reproduce the histopathology of clinical tumors compared to a subcutaneous model [91, 95, 122]. My previous study using a *RHOA*-mutated cancer cell line supported these reports by revealing that, compared with

subcutaneous models, ORT models exhibited abundant stroma and an invasive character [123]. This information prompted me to study the effects of *RHOA* mutations *in vivo* by inoculating the tumor cells into the stomachs of SCID mice.

To understand the molecular mechanism of the effects of *RHOA* mutations, the tumor microenvironment must be analyzed, as both cancer and stromal cells play key roles in forming the tumor microenvironment [124]. Therefore, I decided to carry out a transcriptome analysis using next generation sequencing technology, which makes it possible to distinguish human (tumor cells) and mouse (stromal cells) sequences [104-106, 123]. Thus, in the present study the effects of mutant *RHOA* were evaluated by combining transcriptome analysis of the tumor and stromal components and pathological analysis using an ORT xenograft model.

Materials and Methods

Cell lines

The human gastric cancer cell line MKN74 [125] was purchased from the cell bank of the Japanese Collection of Research Bioresources (National Institutes of Biomedical Innovation, Health and Nutrition). It was cultured using RPMI-1640 medium (Sigma-Aldrich) supplemented with 10% heat-inactivated fetal bovine serum (FBS; Sigma-Aldrich), 10 mM HEPES (Gibco; Thermo Fisher), 1 mM sodium pyruvate (Gibco; Thermo Fisher) and 2.5 g/l D-glucose (Sigma-Aldrich). The cells were maintained in a humidified incubator at 37°C with 5% CO₂.

Generation of MKN74 cell lines expressing *RHOA* mutations

The methods to establish MKN74 cell lines expressing RHOA mutations were previously described [121]. In brief, the coding sequences for the RHOA mutation (NCBI RefSeq Sequence: NM_001664.3) were inserted into the pLV5IN-CMV vector (Takara). The mixture of expression vector and ViraPower Lentiviral Packaging Mix (Thermo Fisher) was introduced into Lenti-X 293T cells (Takara) using FuGENE HD Transfection Reagent (Promega). After 48 h, the culture medium was harvested and virus particles were concentrated with Lenti-X Concentrator (Takara). Prepared lentivirus was transfected into each cell line with hexadimethrine bromide (final 8 µg/ml; Sigma-

Aldrich). Hygromycin (Thermo Fisher) was added to establish stable transfectants at a final concentration of 25 µg/ml for MKN74. The *RHOA* cDNA introduced to the MKN74 cells have mutations that cause resistance to *RHOA*-siRNA.

Cell growth assays

Cells (1.0×10^3 /100 µl/well) were seeded in 96-well cell culture plates (TPP; Sigma-Aldrich) in triplicate. The viable cells were measured 1 day, 4 and 7 days after cell seeding using the CellTiter-Glo 3D Cell Viability Assay, according to the manufacturer's protocol (Promega). The luminescence was measured using a plate reader (PerkinElmer).

Animals

Seven-week-old male severe combined immune-deficient (SCID) mice (C.B-17/lcr-scid/scid Jcl) were provided by CLEA Japan. All animals were housed in a specific pathogen-free environment under controlled conditions (temperature, 20-26°C; humidity, 30-70%; light/dark cycle, 12/12 h) and were allowed to acclimatize and recover from shipping-related stress for more than 5 days prior to the study. Chlorinated water and irradiated food were provided ad libitum. The health of the mice was monitored by daily observation. The humane endpoints were deterioration of general conditions and sacrifice in the event of a body weight loss exceeding 20%. All animal experiments

were performed at Chugai Pharmaceutical Co., Ltd. The experiments were reviewed and approved by the Chugai Pharmaceutical Co., Ltd., Institutional Animal Care and Use Committee.

Orthotopic inoculation and tissue sampling

The mice were inoculated with 3×10^4 cells, suspended in 20 μ l of RPMI-1640 medium containing 50% Matrigel (Corning). Transplantation was carried out using a method based on previous studies [123, 126, 127]. Briefly, the animals were anesthetized under 2.5% isoflurane inhalation anesthesia. Then a surgical incision was made in the medial abdomen and the stomach was exposed. Next 20 μ l of cells suspended in 50% Matrigel were inoculated into the serosa of the ventral stomach. Finally, the stomach was returned to the original position, and the incision was closed. Inoculation was defined as successful when cells had been injected into the intended area with no major leakage outside of the stomach wall. For the WT and mutant groups, the procedure was performed until there were 5 mice for each group. With the mock group, 8 mice were included as controls. The total number of mice used in the study was 42 (Mock, 8; WT, 10; Y42C, 12; Y42S, 12), and the success rate for the inoculation procedure was 55% (23/42 mice: Mock, 8/8; WT, 5/10, Y42C, 5/12; Y42S, 5/12). The average body weight of each group was Mock, 25.9 ± 0.5 g; WT, 25.0 ± 1.1 g; Y42C, 26.2 ± 1.0 g; Y42S, 24.8 ± 1.4 g. The largest diameter of the tumors measured from the serosal side of the stomach was 1.0 cm. There was no difference in diameter between groups. The tumors were observed as single nodules

with no multiple tumors. The tumors were sampled at 4 weeks after inoculation. At necropsy the animals were sacrificed under isoflurane inhalation anesthesia by exsanguination from the abdominal artery and grossly examined.

RNA preparation and transcriptome sequencing

The tumor tissues were collected in Biomasher III (Fujifilm Wako Pure Chemical). I added TRIzol reagent (Thermo Fisher) into the tube and mashed the tissues with a pestle. The tissue lysate was obtained after centrifugation (12,000 x g for 2 min). Total RNA was extracted using the RNeasy mini kit (Qiagen). Total RNA (1.7-2.0 µg) was used to prepare a transcriptome sequencing library for each tumor sample using TruSeq stranded mRNA Library Prep kit (Illumina) following the manufacturer's directions. The libraries were sequenced in 100 bp paired-end reads on a HiSeq2500 sequencer (Illumina). Six libraries were loaded into the single lane of an Illumina flow cell, producing more than 50 million paired-end reads for each sample. Sequenced reads were mapped to all RefSeq transcripts of human (hg38 coordinates) and mouse (mm 10 coordinates) using bowtie 1.1.2 [128] allowing up to one mismatch, and reads mapped to both species or to multiple genes were discarded. The remaining reads were used to estimate the gene expression profile of human cancer cells and mouse stroma cells according to the methods as previously described [104].

Unsupervised clustering of gene expression profiles

After gene-wise Z -score transformation, hierarchical clustering was performed using a Euclidean distance metric on the expression of the highly and variably expressed genes across all samples (mean normalized expression >3.0 and coefficient of variation $>30\%$) using the ComplexHeatmap Bioconductor package [129].

Differential expression analysis

The DESeq2 R package [130] was used for cancer cells and stromal cells independently to detect genes that were expressed differentially between the two conditions. Raw count detected by CASTIN algorithm was used as the input for the DESeq2 software. Adjusted p -values were used to detect differentially expressed genes and \log_2 fold change shrinkage was used to rank genes for Gene Set Enrichment Analysis (GSEA).

GSEA analysis

GSEA [131, 132] was used to identify gene sets that were altered between two conditions. After sorting the genes based on the \log_2 fold change, I applied a pre-ranked GSEA with the javaGSEA desktop application (<http://software.broadinstitute.org/gsea/downloads.jsp>). As gene sets, I used hallmark gene sets in The Molecular Signature Database or genes significantly upregulated or

downregulated in the presence of a ROCK inhibitor (Y-27632) in human keratinocytes (Table 3-3A and B) [133].

Pathological sample preparation

The tumor tissues were sampled and fixed in 4% paraformaldehyde at 4°C for 24 h and embedded into paraffin using the AMeX method [134, 135]. Thin sections were prepared at a thickness of 3-4 µm, and HE stains and Sirius red stains were performed by routine methods for histopathological evaluation. Additional slides were used for immunohistochemistry for CD31 and F4/80. The primary antibodies were rabbit polyclonal antibody to CD31 (1:100 dilution; cat. no. ab28364; Abcam), and rat monoclonal antibody to mouse macrophage F4/80 antigen (1:100 dilution; clone BM8; BMA Biomedicals). Briefly, after deparaffinization, the slides were treated for antigen retrieval by autoclave heating at 120°C for 10 min for CD31, and proteinase K (Dako; Agilent Technologies) for F4/80. Then endogenous peroxidase was quenched with 1% H₂O₂ in methanol, followed by blocking with skim milk (Thermo Fisher). The primary antibodies were incubated with the slides at 4°C overnight. Finally, the secondary antibodies (LSAB2, Agilent Technologies, or N-Histofine® simple stain mouse Rat MAX-PO; Nichirei Biosciences) were applied and the reactions were visualized by 3,3'-diaminobenzidine. The slides were counterstained with hematoxylin and coverslipped for reading under a light microscope.

Histological evaluation

The slides were read and reviewed by 2 certified pathologists, and the scoring criteria were determined by discussion between the pathologists. Furthermore, scoring was carried out based on this criteria by the following methods. The ratio of the area of small nests to total tumor area was evaluated by image analysis on virtual slides scanned using the Leica Aperio ScanScope AT2 (Leica Biosystems) and analyzed with the Aperio Image Scope software (version 12.3.2.7001; Leica Biosystems). To score CD31, the density of positive vascular structures per site at x20 magnification was evaluated by the following criteria: 0, not observed; 1, >0-6 per site; 2, >6-9 per site; 3, 10 or more. For F4/80, the density of positive cells within the tumor mass was evaluated according to the following criteria: 0, not observed; 1, scattered; 2, diffuse; 3, focally dense. Additionally, the histopathological findings in the invasive front of the tumor mass were scored. Each main finding (fibrosis, inflammatory cell infiltration, necrosis of tumor cells) was graded according to the following criteria: 0, not observed; 1, occasionally observed; 2, moderately observed; 3, frequently observed. Then the sum of the 3 findings for each animal was calculated and designated as the histology score.

Statistical analysis

The statistical analysis was performed using the JMP statistical software program (version 11; SAS Institute). Analysis for the ratio of small nest area was conducted by one-way analysis of

variance (ANOVA) followed by a Dunnett's multiple comparison post hoc test. The comparisons of the histologic scores were assessed with non-parametric Steel's test. $p < 0.05$ was considered to indicate a statistically significant difference.

Results

RHOA mutants were found to be enriched in distinctly differential pathways when compared to mock/WT and showed inhibition of ROCK signaling *in vivo*

To determine the effects of *RHOA* mutations *in vivo*, I introduced WT, Y42C, and Y42S *RHOA* into the MKN74 gastric cancer cell line, which originally has WT-*RHOA*. I confirmed the expression of exogenous *RHOA* by western blot analysis after *RHOA*-siRNA treatment to eliminate endogenous *RHOA* which was hindering detection of the transgenes [121]. These cells showed comparable cell growth *in vitro* (Figure 3-1). As for other *in vitro* profiles, I reported the cell motility and actin stress fiber formation in my previous study [121] and the features are summarized in Table 3-1. I inoculated these cell lines into gastric wall (Figure 3-2A). Histopathologically, the tumors were engrafted as an extension from the submucosa to the muscular layer (Figure 3-2B). The tumors subjected to histopathology and transcriptome sequencing are listed in Table 3-2. To evaluate the expression profile of cells that had been inoculated into the mouse stomach, the RNA of each tumor tissue was eluted and sequenced to obtain tumor (human) and host (mouse) transcriptome data simultaneously. Gene expression values were normalized for cancer cells and stromal cells independently so that the sum of the expression values below the 95th percentile would be 300,000. Samples with human (cancer) reads <5% or >95% were removed for subsequent analysis (Table 3-2).

Unsupervised hierarchical clustering for human expression data showed that it was clearly divided into two groups: The Y42C/Y42S group and the mock/WT group (Figure 3-3A). I also performed unsupervised hierarchical clustering for mouse expression data, but as the groups were allocated to various clusters, differences in expression profiles between groups could not be identified (Figure 3-3B). Additionally, the level of expressional change in stroma (mouse) was much lower than that in the tumor (human) (Figure 3-3C). Next I compared the expression of endothelial (*Cd31*), macrophage (*Adgre1*, *Cd68*, *Itgax*, *Mrc1*), and fibroblast (*Coll1A1*, *Thy1*, *Acta2*, *S100a4*) markers, but there was no difference between the groups (data not shown). From this expression profile, I judged that further analysis should be focused on the expression profile of tumor cells.

To understand the state of tumor cells in mutant and non-mutant groups, I performed GSEA [131, 132]. Pathways related to hypoxia and inflammation such as interferon α/γ , TNF α , IL6-JAK-STAT3 signaling, and to inflammatory response were enriched in the mock/WT group (Figure 3-4A and 3-5A). On the other hand, Myc, E2F, oxidative phosphorylation, and G2/M checkpoint pathways, which are related to cell cycle or cell metabolism, were enriched in the Y42C/Y42S group (Figure 3-4A and 3-5B). In addition, I confirmed the ROCK signaling status in the tumor cells. To evaluate the activation status of ROCK signaling, I performed a GSEA analysis with a ROCK inhibitor-related gene set, which was selected from published data (Table 3-3A and B) [133]. As a result, genes downregulated after ROCK inhibitor treatment were significantly enriched in the mock/WT group,

whereas the upregulated genes were enriched in the Y42C/Y42S group (Figure 3-4B and 3-6). These results indicated that ROCK signaling was inhibited in *RHOA* mutants *in vivo* as well as *in vitro*.

Mutated *RHOA* contributes to a pattern of small tumor nest growth, and to changes in stromal cells

In the orthotopic model, the size of the tumor cannot be compared accurately because the size is affected by the area of inoculation. Because of this, I compared the expression of Ki-67, but there was no difference between the WT group and mutant groups. Thus, I conducted a detailed histopathological analysis and compared the morphological features of the tumor with the RNA expression profiles. Morphologically, mock and WT tumors consisted mainly of large tumor nests, but in contrast, the mutant tumors consisted mainly of small tumor nests that were circumscribed by fine collagen fibers (Figure 3-7A and B). This was further confirmed by morphometric analysis of the area for each type of tumor nest. The ratio of small tumor nest to total tumor nest area in Y42C and Y42S was significantly higher than in mock or WT (Figure 3-7C). The average ratio of small tumor nests was 0.09 in mock, 0.17 in WT, 0.46 in Y42C, and 0.46 in Y42S. Thus I found that the mutant tumors had a distinctly different growth pattern compared to the mock or WT tumors.

I speculated that the difference in the amount of small tumor nests was related to a difference in tumor-stromal interaction, and because the hypoxia signature was enriched in mock/WT but not in

RHOA mutants, I focused on tumor angiogenesis.

In order to determine the involvement of angiogenesis, I evaluated the number of CD31-positive blood vessels by immunohistochemical analysis (Figure 3-8A) and found that there were higher numbers in Y42C and Y42S than that in the mock and WT. The average scores for the number of blood vessels per site were 1.8 in Y42C, 2.6 in Y42S, 0.8 in mock, and 1.0 in WT. Tumor angiogenesis is reported to be induced by tumor associated macrophages [136, 137], thus next I evaluated macrophage (M ϕ) infiltration into tumors by immunohistochemical analysis of F4/80 (Figure 3-8B). I found that in the mock and WT tumors, the positive cells tended to be located around the tumor mass, but in mutant tumors, the macrophages tended to diffusely infiltrate the tumor mass. This was further confirmed by scoring of the positive cells infiltrating into the tumor mass. The average scores of macrophage infiltration into the tumor mass were 2.4 in Y42C and 2.6 in Y42S, which were higher than those in the mock (0.4) and WT (1.0) tumors. These results indicated that *RHOA* mutations contributed to tumor angiogenesis and the infiltration of macrophages.

Reduced host reaction in the invasive front of *RHOA* mutant tumors

Next I focused on the invasive front of the tumor mass (Figure 3-9A). In the invasive front of the mock and WT tumors, there was a desmoplastic reaction or fibrosis accompanied by inflammatory cell infiltration. Along with these findings, necrosis of tumor cells was increased. In

contrast, the host reaction was notably weaker in the mutant tumors. To further clarify the difference in host reaction, the findings were scored and statistically analyzed. I found that the total histology scores in the Y42C and Y42S tumors were significantly lower than scores in the mock/WT tumors (Figure 3-9B). The average total histology score (see Histological evaluation in Materials and Methods) of each group was 3.4 in Y42C, 3.4 in Y42S, 7.2 in mock, and 7.8 in WT. These results indicate that *RHOA*-mutant cancer cells have the ability to invade the surrounding tissue without causing a strong antitumor reaction.

Discussion

In the present study, I revealed the transcriptome and histological changes that occurred when *RHOA* mutations were introduced into MKN74 cells. Tumors in the *RHOA* mutant groups were composed mainly of small tumor nests compared to those in the non-mutant groups. A distinct feature of clinical DGC is that tumor cells exist within the stroma as single cells or small cell clusters. My current results suggest that *RHOA* mutations at least in part contribute to this poorly cohesive growth pattern, although as non-mutated clinical DGC also exhibits this feature, there may be other factors involved.

Another notable morphological finding in the present study was that, in contrast to mock and WT tumors, *RHOA*-mutated tumors had little host reaction in the invasive front of the tumor. I previously reported that in clinical DGC, *RHOA*-mutated tumors showed an intramucosal permeative growth pattern in the mucosa, which is characterized by infiltration of tumor nests between the normal pits or glands with no recognizable margin, indicating that there is little stromal reaction against the tumor. This contrasted with the expansive pattern of destructive invasion and a relatively well-defined margin seen in non-mutated tumors [120]. The lack of host reaction in the *RHOA*-mutant tumors of the present study was thought to reflect the distinctive growth pattern found in the mucosa of clinical *RHOA*-mutated DGC. Together with the effects on the size of the tumor nests, my results suggest that

RHOA mutations are likely to have a direct role in the development of the morphology that is distinctive of clinical DGC.

Since the hypoxic signature in mock/WT tumors was more enriched than that noted in the mutant tumors, I considered the involvement of angiogenesis and found that the *RHOA* mutants had higher levels of blood vessel formation and infiltration of macrophages into the tumor mass. Angiogenesis is closely related to infiltration of macrophages [138-140]. Additionally, Yin et al reported that a high density of macrophages was correlated with DGC [141]. Therefore, these results suggest that *RHOA* mutants affect tumor angiogenesis induced by macrophages in the tumor mass, and that the tumor microenvironment may be closely related to the growth pattern of DGC. Macrophages were infiltrated in mutated-*RHOA* group, but inflammation related pathways were not enriched. The character of macrophages is quite diverse and M1-type macrophage are involved in inflammation process, but M2-type are engaged in tissue repair [142-144]. Therefore, detailed characterization of macrophages or other immune cells would deepen our understanding in DGC biology.

In my previous *in vitro* study, I found that mutant *RHOA* inhibited ROCK signaling in a dominant negative manner, which caused the actin cytoskeleton to become loose and led to a change in cell-cell interactions [121]. Such changes may be related to the growth pattern of small nests *in vivo*. ROCK inhibition is also known to be related to anoikis resistance [87], which may have a role in the

maintenance of the small nest pattern. The lack of strong host reaction in the *RHOA*-mutated tumors may also be related to these mechanisms; however, since much is still unknown, further studies are necessary to elucidate the molecular mechanism of the features *in vivo*.

The dramatic histopathological difference in host reaction between *RHOA* mutants and mock/WT suggests that *RHOA* mutations affect cells such as fibroblasts, endothelial cells, and immune cells in mouse stroma. However, the level of expressional change in the stroma was much lower than that in the tumor (Figure 3-3C), and the mouse expression profiles did not reveal any difference between *RHOA* mutants and mock/WT tumors. This discrepancy between the histopathology results and the RNA expression profile may have occurred because I evaluated the expression in the whole tumor tissue. As there are several cell components in the tissue surrounding the tumor mass, local changes such as those at the invasion front were thought to be difficult to discriminate. To overcome this issue, the expression profile at the single cell level instead of in bulk is necessary. Since several reports show detailed cross-talk between tumor and components of the tumor microenvironment [145-147], I anticipate that single cell RNA sequencing will more precisely reveal the interaction between the tumor and its microenvironment and the molecular mechanisms involved.

In summary, my results from an orthotopic model in the stomach have provided the first direct evidence concerning the effects of mutated *RHOA in vivo*. Since the features of this xenograft model allow insights into the biology in human clinical cancer, these results will accelerate the

understanding of how *RHOA* mutations contribute to the disease biology of DGC and may promote the development of future therapeutic strategies.

Tables and Figures

Table 3-1: *In vitro* phenotypes of the MKN74 cells used for engraftment.

Transfected <i>RHOA</i>	Cell growth rate	Migration activity ^a	Invasion activity ^a	Actin fiber formation ^b
WT	n.s.	Low	n.s.	High
Y42C	n.s.	High	n.s.	Low
Y42S	n.s.	High	n.s.	Low

^aMigration and invasion activity were evaluated with Boyden Chamber assay. ^bActin stress fiber formation was evaluated with rhodamine phalloidin staining as previously described [121]. n.s., no significant difference

Table 3-2: The tumors subjected to histopathology and transcriptome sequencing

Introduced vector	Sample ID	Pathology	RNAseq	Good reads	Uniquely mapped	Mapping on human	Mapping on mouse	Tumor rate (%)	Criteria Passed/NG
Mock	Mock-1	x	○	43,011,502	28,508,787	3,134,260	25,374,527	11.0	Passed
	Mock-2	x	○	43,999,830	31,143,655	5,363,072	25,780,583	17.2	Passed
	Mock-3	○	○	38,741,335	26,611,010	1,410,391	25,200,619	5.3	Passed
	Mock-4	○	○	37,849,948	25,805,921	3,553,336	22,252,585	13.8	Passed
	Mock-5	○	○	42,713,195	29,903,365	8,399,729	21,503,636	28.1	Passed
	Mock-6	○	○	34,337,685	24,342,738	5,198,692	19,144,046	21.4	Passed
	Mock-7	x	○	38,776,520	27,519,748	21,766,319	5,753,429	79.1	Passed
	Mock-8	○	○	38,066,105	27,286,425	21,423,436	5,862,989	78.5	Passed
WT	WT-1	○	x	36,185,604	25,610,289	38,999	25,571,290	0.2	NG
	WT-2	○	x	31,302,357	22,875,485	1,731	22,873,754	0.0	NG
	WT-3	x	○	34,437,645	25,742,989	22,922,847	2,820,142	89.0	Passed
	WT-4	○	○	39,314,638	29,097,066	24,116,698	4,980,368	82.9	Passed
	WT-5	○	○	39,924,991	28,908,953	5,562,383	23,346,570	19.2	Passed
Y42C	42C-1	○	○	43,838,287	30,569,870	2,389,900	28,179,970	7.8	Passed
	42C-2	○	○	41,635,723	29,640,538	2,802,156	26,838,382	9.5	Passed
	42C-3	○	x	39,261,333	28,934,139	27,947,610	986,529	96.6	NG
	42C-4	○	○	36,310,887	26,376,653	14,875,311	11,501,342	56.4	Passed
	42C-5	○	○	38,904,699	28,633,340	4,316,539	24,316,801	15.1	Passed
Y42S	42S-1	○	○	36,162,514	27,125,316	25,659,264	1,466,052	94.6	Passed
	42S-2	○	○	42,985,399	31,026,475	10,277,421	20,749,054	33.1	Passed
	42S-3	○	○	47,020,636	34,180,119	17,196,435	16,983,684	50.3	Passed
	42S-4	○	○	43,348,517	31,226,955	9,002,373	22,224,582	28.8	Passed
	42S-5	○	○	50,951,030	35,974,254	10,896,740	25,077,514	30.3	Passed

WT, wild-type; ○, included in analysis; x, excluded from analysis.

Table 3-3: Downregulated (A) and upregulated (B) genes after ROCK inhibitor treatment

A	#	Gene name	#	Gene name
	1	<i>A2ML1</i>	33	<i>C6orf15</i>
	2	<i>A4GALT</i>	34	<i>C9orf169</i>
	3	<i>AAK1</i>	35	<i>CALB2</i>
	4	<i>ABCA12</i>	36	<i>CALCOCO2</i>
	5	<i>ACAP2</i>	37	<i>CALML5</i>
	6	<i>ACOT11</i>	38	<i>CARD18</i>
	7	<i>ACPP</i>	39	<i>CASP4</i>
	8	<i>ACSL1</i>	40	<i>CAST</i>
	9	<i>AGRN</i>	41	<i>CCDC132</i>
	10	<i>AHR</i>	42	<i>CCDC64B</i>
	11	<i>AKTIP</i>	43	<i>CD24</i>
	12	<i>ALDH1A3</i>	44	<i>CD82</i>
	13	<i>ANKRD22</i>	45	<i>CEACAM6</i>
	14	<i>ANKRD22</i>	46	<i>CGN</i>
	15	<i>ANKRD35</i>	47	<i>CHMP4C</i>
	16	<i>AQP9</i>	48	<i>CIB2</i>
	17	<i>ARHGEF37</i>	49	<i>CLCN3</i>
	18	<i>ARL5A</i>	50	<i>CLDN23</i>
	19	<i>ASPRV1</i>	51	<i>CLDN7</i>
	20	<i>ASS1</i>	52	<i>CLIC3</i>
	21	<i>ATMIN</i>	53	<i>CLINT1</i>
	22	<i>ATP12A</i>	54	<i>CLIP1</i>
	23	<i>ATP6V0A1</i>	55	<i>CLTB</i>
	24	<i>ATXN1</i>	56	<i>CNFN</i>
	25	<i>BPIL2</i>	57	<i>CNKSR3</i>
	26	<i>BSPRY</i>	58	<i>COBLL1</i>
	27	<i>BTG1</i>	59	<i>COL11A2</i>
	28	<i>BZW1</i>	60	<i>CPE</i>
	29	<i>C10orf116</i>	61	<i>CPM</i>
	30	<i>C10orf54</i>	62	<i>CRB3</i>
	31	<i>C15orf52</i>	63	<i>CRCT1</i>
	32	<i>C5orf46</i>	64	<i>CRISPLD2</i>

#	Gene name	#	Gene name
65	<i>CRNN</i>	100	<i>FUT3</i>
66	<i>CST6</i>	101	<i>FYTTD1</i>
67	<i>CST6</i>	102	<i>GAS6</i>
68	<i>CWH43</i>	103	<i>GAS6</i>
69	<i>CYB5R2</i>	104	<i>GCNT3</i>
70	<i>CYB5R3</i>	105	<i>GDPD3</i>
71	<i>CYP4B1</i>	106	<i>GFPT1</i>
72	<i>CYP4B1</i>	107	<i>GLRX</i>
73	<i>CYP4F22</i>	108	<i>GLTP</i>
74	<i>CYP4F3</i>	109	<i>GLTPD1</i>
75	<i>CYTH1</i>	110	<i>GPR1</i>
76	<i>DAAM1</i>	111	<i>GPR56</i>
77	<i>DBNDD1</i>	112	<i>GRHL1</i>
78	<i>DBNDD2</i>	113	<i>GRHL3</i>
79	<i>DHRS11</i>	114	<i>GSDMA</i>
80	<i>DHRS3</i>	115	<i>GSDMC</i>
81	<i>DHRS9</i>	116	<i>HAL</i>
82	<i>DIP2B</i>	117	<i>HECTD3</i>
83	<i>DLG1</i>	118	<i>HIP1R</i>
84	<i>DNAJA4</i>	119	<i>HIST1H2AC</i>
85	<i>DSC2</i>	120	<i>HIST1H2AE</i>
86	<i>ENDOD1</i>	121	<i>HIST1H2BC</i>
87	<i>EPHX3</i>	122	<i>HIST1H2BD</i>
88	<i>ERP27</i>	123	<i>HIST1H2BG</i>
89	<i>FA2H</i>	124	<i>HIST2H2AA3</i>
90	<i>FADS3</i>	125	<i>HIST2H2BE</i>
91	<i>FAM127A</i>	126	<i>HOPX</i>
92	<i>FAM129B</i>	127	<i>HPGD</i>
93	<i>FAM135A</i>	128	<i>HSPB1</i>
94	<i>FAM3D</i>	129	<i>HSPB8</i>
95	<i>FAM43A</i>	130	<i>HSPC159</i>
96	<i>FLG</i>	131	<i>ID1</i>
97	<i>FLG</i>	132	<i>IDS</i>
98	<i>FTH1P3</i>	133	<i>IDS</i>
99	<i>FUT2</i>	134	<i>IER3</i>

#	Gene name	#	Gene name
135	<i>IER5</i>	170	<i>KRT80</i>
136	<i>IGFL2</i>	171	<i>KRT80</i>
137	<i>IL1F10</i>	172	<i>KRT81</i>
138	<i>IL1F5</i>	173	<i>KRTDAP</i>
139	<i>IQSEC2</i>	174	<i>LACTB</i>
140	<i>ISG20</i>	175	<i>LAD1</i>
141	<i>ITPRIP</i>	176	<i>LAMP2</i>
142	<i>IVL</i>	177	<i>LASS3</i>
143	<i>KAT2B</i>	178	<i>LCE3D</i>
144	<i>KAZN</i>	179	<i>LCE3E</i>
145	<i>KCNK1</i>	180	<i>LCE6A</i>
146	<i>KCNK12</i>	181	<i>LCE6A</i>
147	<i>KCTD21</i>	182	<i>LCN2</i>
148	<i>KIAA0513</i>	183	<i>LGALS8</i>
149	<i>KIAA1468</i>	184	<i>LIPG</i>
150	<i>KIAA1737</i>	185	<i>LIPM</i>
151	<i>KLK11</i>	186	<i>LOC100131138</i>
152	<i>KLK12</i>	187	<i>LOC100131138</i>
153	<i>KLK13</i>	188	<i>LOC388564</i>
154	<i>KLK5</i>	189	<i>LOC441052</i>
155	<i>KLK5</i>	190	<i>LOC730081</i>
156	<i>KLK5</i>	191	<i>LOR</i>
157	<i>KLK6</i>	192	<i>LPHN2</i>
158	<i>KLK7</i>	193	<i>LPXN</i>
159	<i>KLK7</i>	194	<i>LRRC37A</i>
160	<i>KLK8</i>	195	<i>LRRC8B</i>
161	<i>KPRP</i>	196	<i>LSR</i>
162	<i>KRT1</i>	197	<i>LY6G6C</i>
163	<i>KRT10</i>	198	<i>LYPD3</i>
164	<i>KRT13</i>	199	<i>LYPD5</i>
165	<i>KRT17</i>	200	<i>LYPD5</i>
166	<i>KRT23</i>	201	<i>MAL</i>
167	<i>KRT34</i>	202	<i>MALL</i>
168	<i>KRT77</i>	203	<i>MAMDC2</i>
169	<i>KRT78</i>	204	<i>MAN2B2</i>

#	Gene name	#	Gene name
205	<i>MANSC1</i>	240	<i>OSTF1</i>
206	<i>MANSC1</i>	241	<i>OTUB2</i>
207	<i>MAP2</i>	242	<i>PCSK6</i>
208	<i>MAP2</i>	243	<i>PERP</i>
209	<i>MARCHF3</i>	244	<i>PGRMC2</i>
210	<i>MAST4</i>	245	<i>PI3</i>
211	<i>MBOAT2</i>	246	<i>PIM3</i>
212	<i>ME1</i>	247	<i>PITX1</i>
213	<i>METRNL</i>	248	<i>PLA2G4E</i>
214	<i>METRNL</i>	249	<i>PLA2G7</i>
215	<i>MFSD1</i>	250	<i>PLCD1</i>
216	<i>MFSD6</i>	251	<i>PLD5</i>
217	<i>MFSD6</i>	252	<i>PLEKHA7</i>
218	<i>MIR614</i>	253	<i>PLEKHM1</i>
219	<i>MLPH</i>	254	<i>PLOD2</i>
220	<i>MPZL2</i>	255	<i>POF1B</i>
221	<i>MSRB3</i>	256	<i>PPARD</i>
222	<i>MUC1</i>	257	<i>PPP2R2B</i>
223	<i>MUCL1</i>	258	<i>PPP3CA</i>
224	<i>MYL9</i>	259	<i>PRB1</i>
225	<i>NCCRP1</i>	260	<i>PRB2</i>
226	<i>NCCRP1</i>	261	<i>PRB4</i>
227	<i>NCF2</i>	262	<i>PRDM1</i>
228	<i>NCK2</i>	263	<i>PRICKLE2</i>
229	<i>NCRNA00087</i>	264	<i>PRKAR1A</i>
230	<i>NDRG2</i>	265	<i>PROM2</i>
231	<i>NEBL</i>	266	<i>PRRT3</i>
232	<i>NFATC4</i>	267	<i>PRSS2</i>
233	<i>NIPA1</i>	268	<i>PRSS27</i>
234	<i>NLRX1</i>	269	<i>PSG11</i>
235	<i>NPW</i>	270	<i>PSORS1C2</i>
236	<i>NRBF2</i>	271	<i>PTTG1IP</i>
237	<i>NSF</i>	272	<i>PYCARD</i>
238	<i>NUAK2</i>	273	<i>RAB11FIP1</i>
239	<i>OBFC1</i>	274	<i>RAB11FIP1</i>

#	Gene name	#	Gene name
275	<i>RAB9A</i>	310	<i>SERPINB3</i>
276	<i>RAC1</i>	311	<i>SERPINB6</i>
277	<i>RAET1E</i>	312	<i>SGPP2</i>
278	<i>RAET1G</i>	313	<i>SH2D4A</i>
279	<i>RAET1L</i>	314	<i>SH3BGRL2</i>
280	<i>RAET1L</i>	315	<i>SH3KBP1</i>
281	<i>RAP1GAP</i>	316	<i>SH3KBP1</i>
282	<i>RBM47</i>	317	<i>SHROOM3</i>
283	<i>RDH11</i>	318	<i>SIAE</i>
284	<i>RHCG</i>	319	<i>SLC12A8</i>
285	<i>RIMBP3C</i>	320	<i>SLC25A43</i>
286	<i>RNASE7</i>	321	<i>SLC37A2</i>
287	<i>RNF144B</i>	322	<i>SLC39A2</i>
288	<i>RPL21</i>	323	<i>SLC39A8</i>
289	<i>RPTN</i>	324	<i>SLC44A1</i>
290	<i>S100A11</i>	325	<i>SLC44A3</i>
291	<i>S100A4</i>	326	<i>SLC5A1</i>
292	<i>S100A4</i>	327	<i>SLC6A14</i>
293	<i>S100A7</i>	328	<i>SLPI</i>
294	<i>S100P</i>	329	<i>SMPDL3B</i>
295	<i>SAMD9</i>	330	<i>SNX2</i>
296	<i>SASH1</i>	331	<i>SNX24</i>
297	<i>SBSN</i>	332	<i>SORT1</i>
298	<i>SC4MOL</i>	333	<i>SOX21</i>
299	<i>SCEL</i>	334	<i>SPINK5</i>
300	<i>SCEL</i>	335	<i>SPINK6</i>
301	<i>SCNN1A</i>	336	<i>SPINK7</i>
302	<i>SDCBP2</i>	337	<i>SPNS2</i>
303	<i>SDCBP2</i>	338	<i>SPRR1A</i>
304	<i>SDCBP2</i>	339	<i>SPRR2C</i>
305	<i>SDR42E1</i>	340	<i>SPRR2E</i>
306	<i>SDR9C7</i>	341	<i>SPRR2E</i>
307	<i>SEC14L2</i>	342	<i>SPRR3</i>
308	<i>SERPINA3</i>	343	<i>SPRR4</i>
309	<i>SERPINB13</i>	344	<i>SPTLC3</i>

#	Gene name	#	Gene name
345	<i>SPTLC3</i>	380	<i>WSB2</i>
346	<i>STK40</i>	381	<i>XKRX</i>
347	<i>STRN</i>	382	<i>ZMIZ1</i>
348	<i>STX19</i>		
349	<i>SULT2B1</i>		
350	<i>SULT2B1</i>		
351	<i>SVIL</i>		
352	<i>TDRD7</i>		
353	<i>TIMP2</i>		
354	<i>TINAGL1</i>		
355	<i>TMEM125</i>		
356	<i>TMEM45A</i>		
357	<i>TMEM45A</i>		
358	<i>TMEM86A</i>		
359	<i>TMSL3</i>		
360	<i>TNFAIP8L3</i>		
361	<i>TNIP1</i>		
362	<i>TP53I3</i>		
363	<i>TPD52L1</i>		
364	<i>TPD52L1</i>		
365	<i>TRADD</i>		
366	<i>TRIM2</i>		
367	<i>UGT1A6</i>		
368	<i>UGT1A6</i>		
369	<i>UGT2B7</i>		
370	<i>ULBP2</i>		
371	<i>UPK1A</i>		
372	<i>UPK1B</i>		
373	<i>USP6NL</i>		
374	<i>VASN</i>		
375	<i>VPS37C</i>		
376	<i>VSIG10L</i>		
377	<i>VWA5A</i>		
378	<i>WFDC5</i>		
379	<i>WFDC5</i>		

B	#	Gene name	#	Gene name
	1	<i>ADCK5</i>	36	<i>FCER1A</i>
	2	<i>AGAP6</i>	37	<i>GALNTL4</i>
	3	<i>AMDHD2</i>	38	<i>GLDC</i>
	4	<i>ANKMY2</i>	39	<i>HERC5</i>
	5	<i>ANP32B</i>	40	<i>HMGN2</i>
	6	<i>ARHGEF12</i>	41	<i>HMGN2</i>
	7	<i>ATIC</i>	42	<i>HMGN2P46</i>
	8	<i>BANF1</i>	43	<i>HSPC157</i>
	9	<i>BNC1</i>	44	<i>IFFO2</i>
	10	<i>C10orf2</i>	45	<i>IFT27</i>
	11	<i>C11orf17</i>	46	<i>IL33</i>
	12	<i>C15orf42</i>	47	<i>IRS1</i>
	13	<i>C17orf81</i>	48	<i>JAG2</i>
	14	<i>C1orf105</i>	49	<i>KCND3</i>
	15	<i>CAV1</i>	50	<i>LOC100507358</i>
	16	<i>CBY1</i>	51	<i>LRIG2</i>
	17	<i>CDC25C</i>	52	<i>LY6H</i>
	18	<i>CDH11</i>	53	<i>MAD2L2</i>
	19	<i>CHEK2</i>	54	<i>MRPL11</i>
	20	<i>CKAP5</i>	55	<i>MRPL2</i>
	21	<i>CLK2</i>	56	<i>MSH6</i>
	22	<i>CLUAP1</i>	57	<i>MTHFSD</i>
	23	<i>CPVL</i>	58	<i>NLN</i>
	24	<i>CPVL</i>	59	<i>NUP85</i>
	25	<i>CREB5</i>	60	<i>OGG1</i>
	26	<i>DDB2</i>	61	<i>OPN5</i>
	27	<i>DDX28</i>	62	<i>PAOX</i>
	28	<i>DHX35</i>	63	<i>PGBD5</i>
	29	<i>DPP3</i>	64	<i>PHB2</i>
	30	<i>DUSP5</i>	65	<i>PISD</i>
	31	<i>ELAVL2</i>	66	<i>PLCD4</i>
	32	<i>FAM156B</i>	67	<i>POLR1E</i>
	33	<i>FAM82B</i>	68	<i>PSMB8</i>
	34	<i>FAM86C</i>	69	<i>PSME2</i>
	35	<i>FBXL6</i>	70	<i>PTTG1</i>

#	Gene name
71	<i>RFC2</i>
72	<i>RNPS1</i>
73	<i>RPA1</i>
74	<i>SDHA</i>
75	<i>SDHB</i>
76	<i>SEC22C</i>
77	<i>SEPHS2</i>
78	<i>SF3B5</i>
79	<i>SHMT1</i>
80	<i>SNORA24</i>
81	<i>SNORA61</i>
82	<i>SNORD14A</i>
83	<i>SNORD17</i>
84	<i>SNRPA</i>
85	<i>SSRP1</i>
86	<i>STAG3L3</i>
87	<i>THOC6</i>
88	<i>TMEM143</i>
89	<i>TSPAN4</i>
90	<i>TWF2</i>
91	<i>UTY</i>
92	<i>VAV2</i>
93	<i>VDAC1</i>
94	<i>WDR66</i>

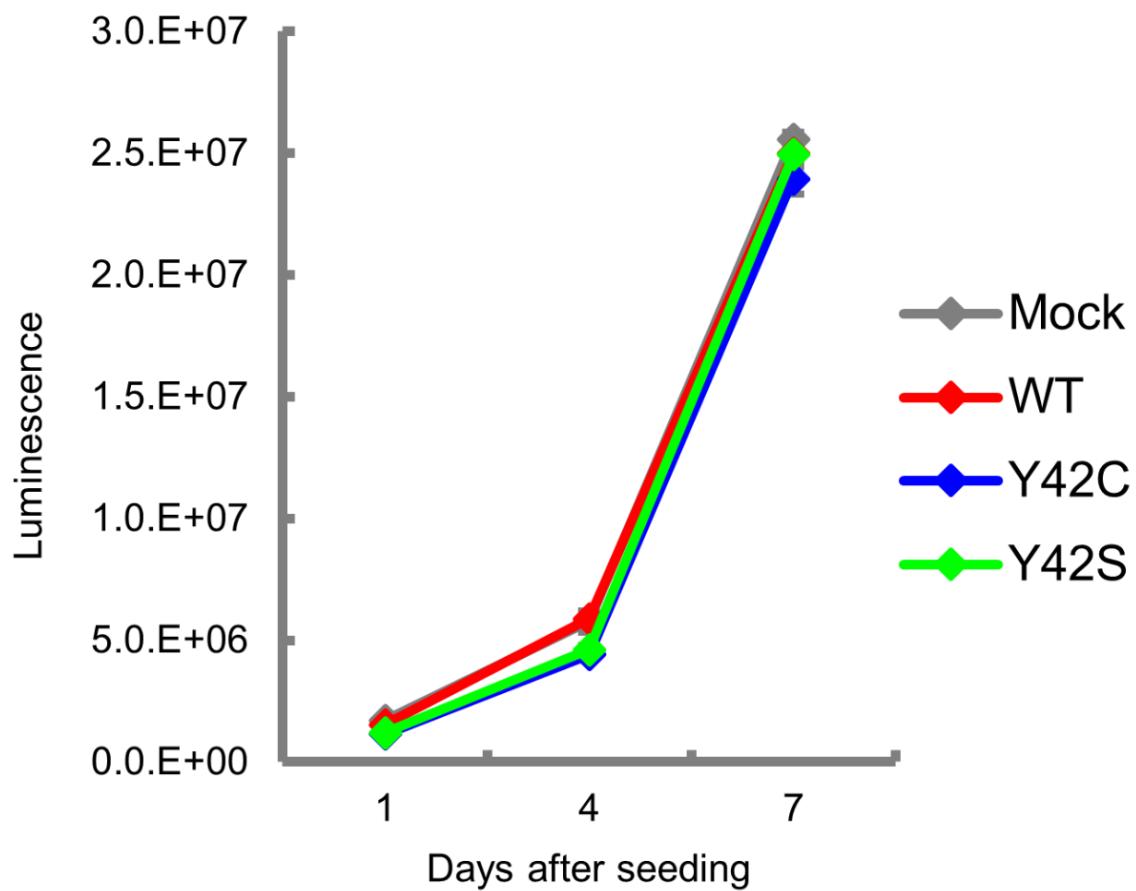
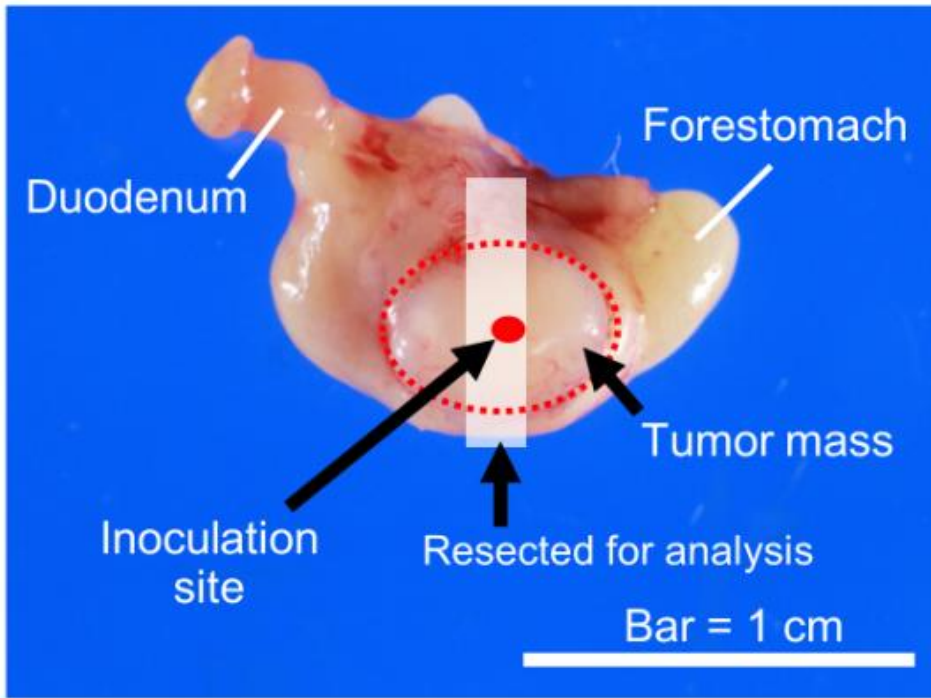


Figure 3-1: Cell growth rate of WT-, Y42C-, and Y42S-transfected MKN74 cells compared to the growth rate of the mock group

Cell lines were seeded in a cell culture plate and then incubated for 7 days. The viable cells were measured with a CellTiter-Glo 3D Cell Viability Assay on day 1, 4 and 7. Data are shown as mean \pm SD ($n=3$).

A



B

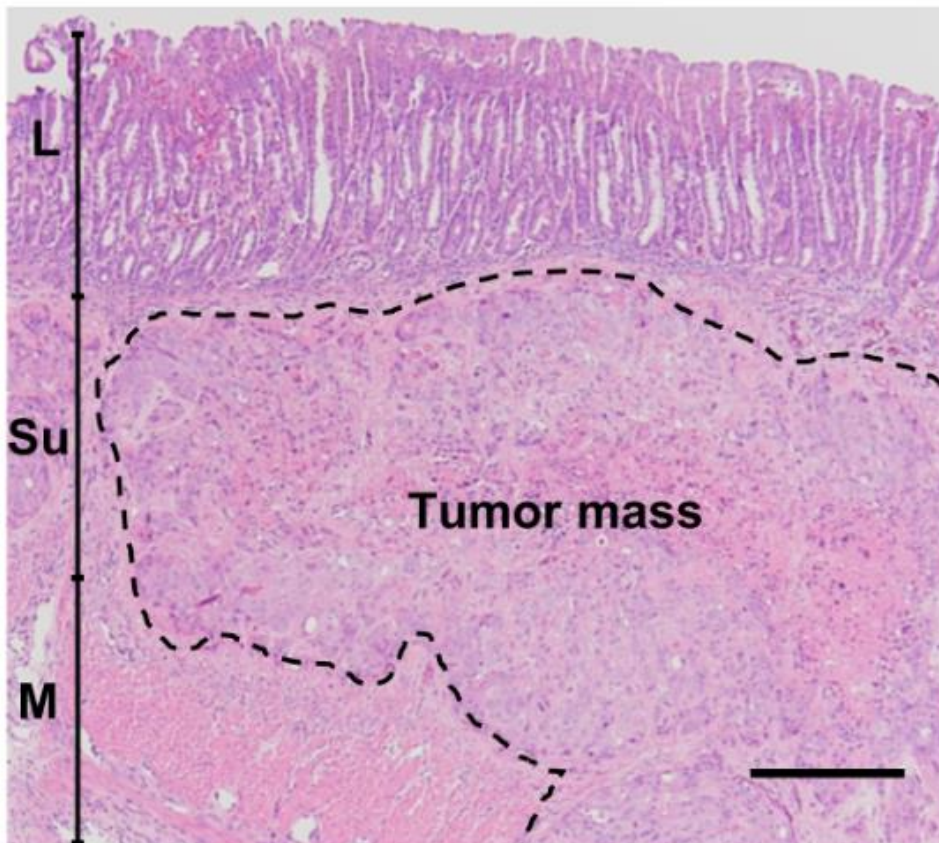


Figure 3-2:

(A) Illustration of the injection site. (B) Representative figure showing the location of engraftment. L, lamina propria mucosae; Su, submucosa; M, muscular layer. Scale bar, 250 μm .

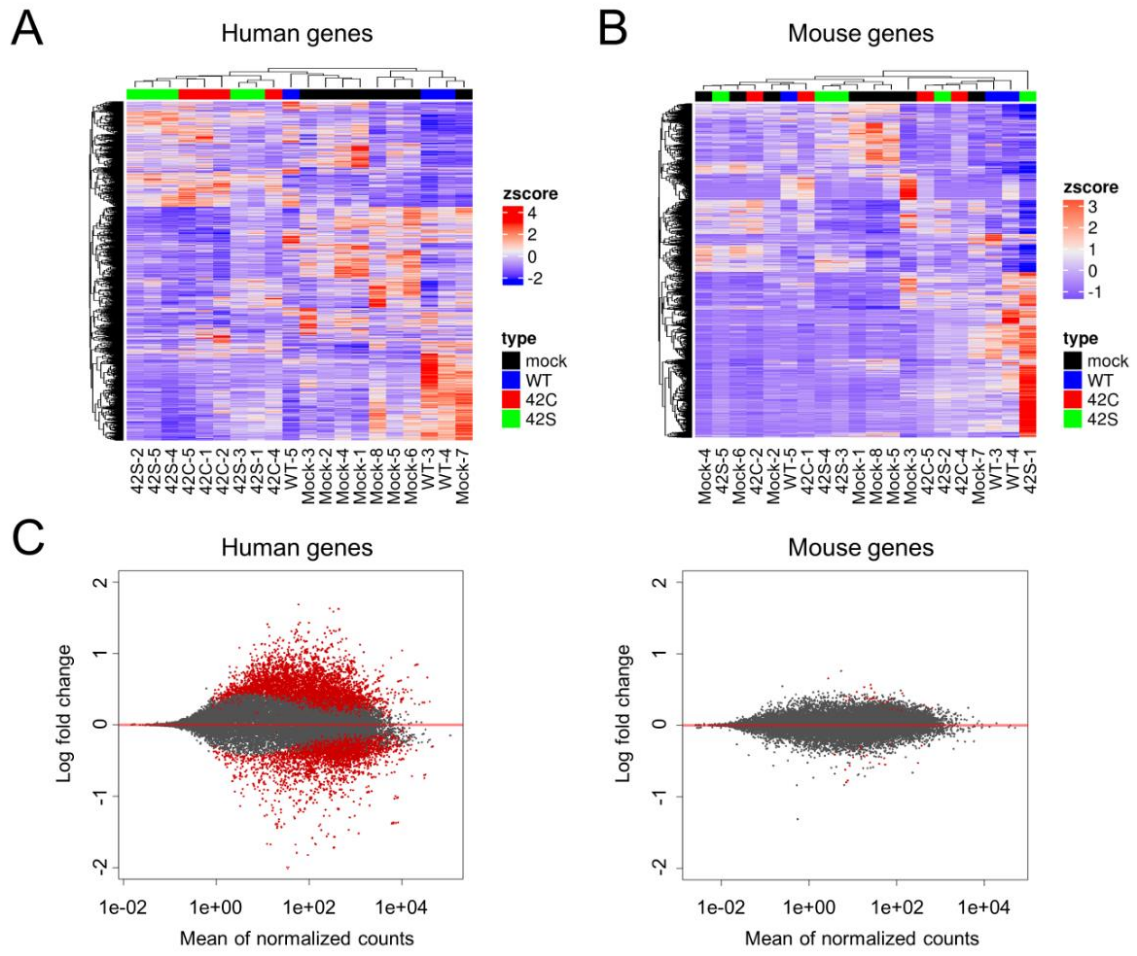
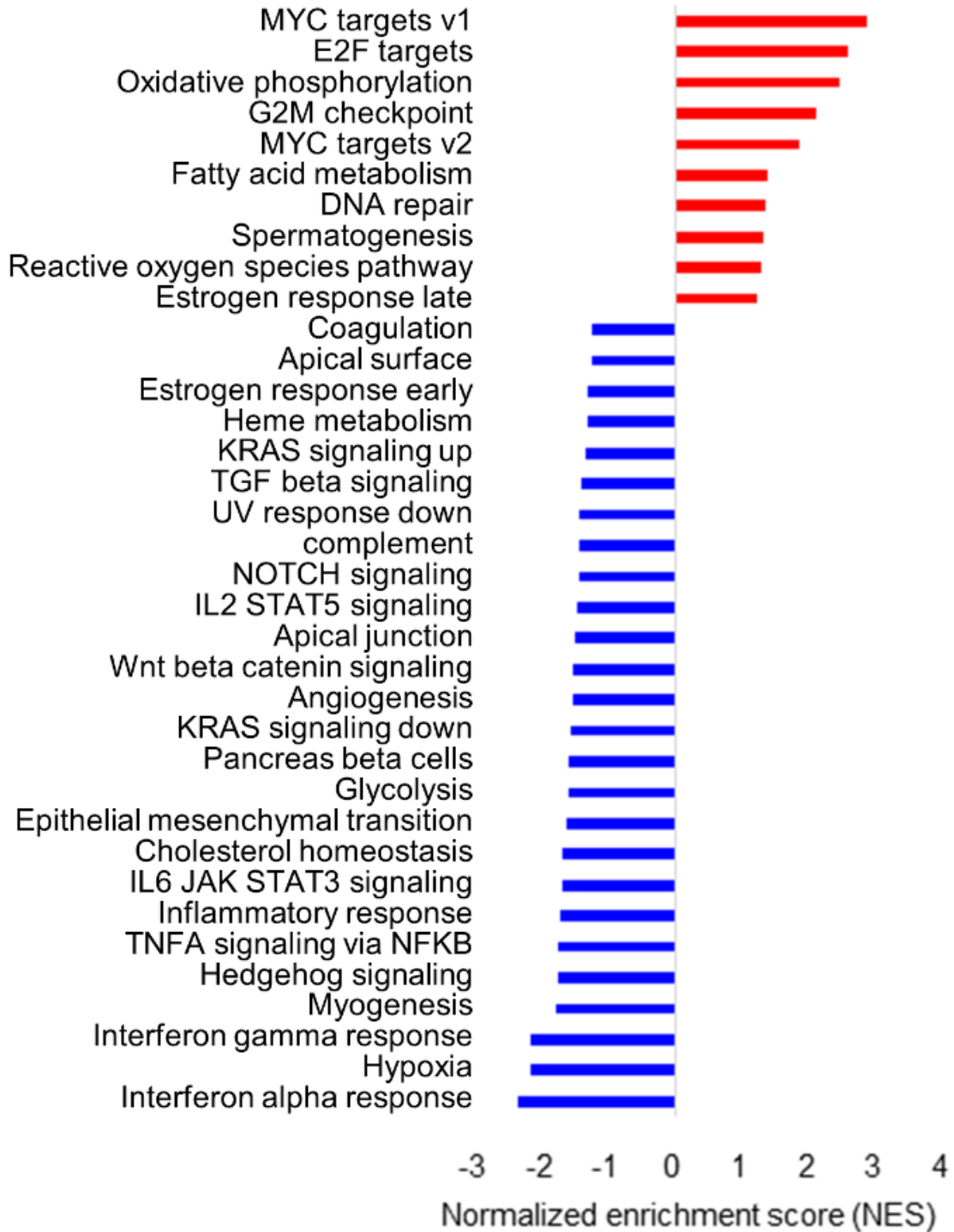


Figure 3-3: Transcriptome analysis of orthotopic inoculated tumors

Hierarchical clustering of the differentially expressed human genes (A) and mouse genes (B) across all samples is shown vertically for genes and horizontally for the tumor samples. Samples that are mock, WT, Y42C, and Y42S are indicated in black, blue, red, and green, respectively. In the matrix table, red indicates high expression and blue indicates low expression profiles. (C) MA plots of altered gene expression between the Y42C/Y42S group and mock/WT group in human genes (tumor, left panel) and mouse genes (stroma, right panel). Each dot represents a transcript. The x-axis shows normalized counts and the y-axis shows the expressional change in log scale. Transcripts with an adjusted p -value <0.1 are shown in red.

A

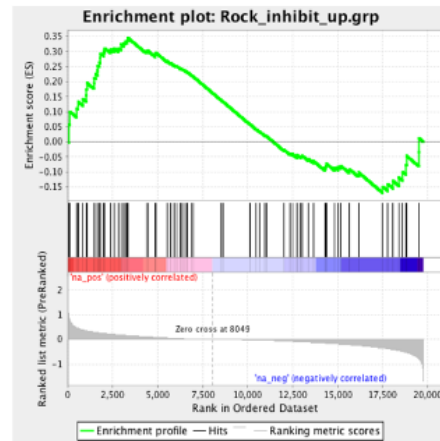
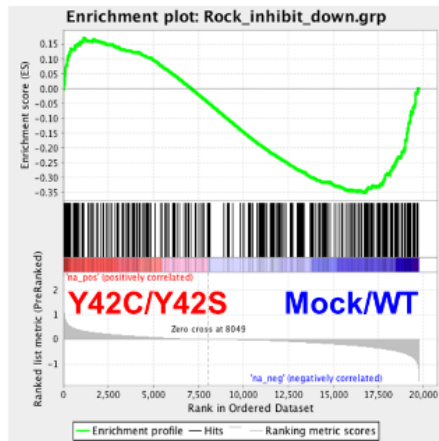
Mock/WT vs Y42C/Y42S



B

Downregulated

Upregulated



ES -0.35
Nominal p-value 0.020

0.35
0.044

Core genes

Core genes

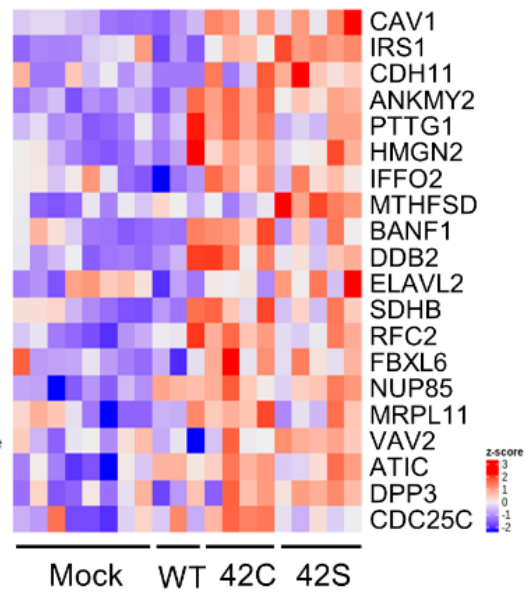
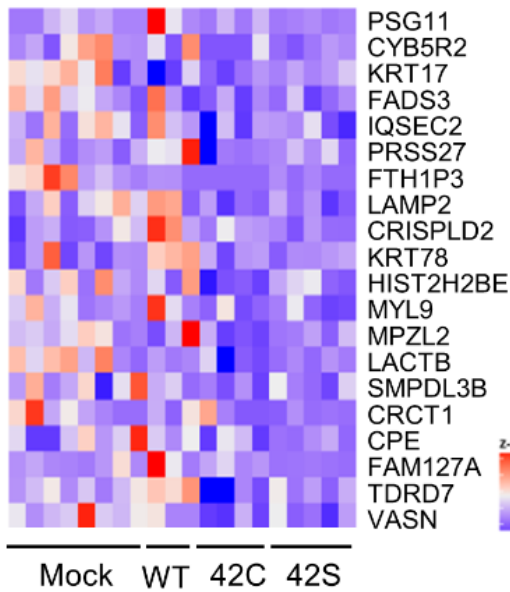


Figure 3-4: GSEA analysis of mock/WT vs. Y42C/Y42S

(A) GSEA analysis using hallmark gene sets from the Molecular Signature Database (see: <http://software.broadinstitute.org/gsea/msigdb/index.jsp>) was carried out. The statistically significant signatures were selected (FDR <0.25) and placed in order of normalized enrichment score (NES), which represents the strength of the relationship between the phenotype and gene signature. Red bars indicate the pathways enriched in the Y42C/Y42S group and blue bars indicate those enriched in the mock/WT group. (B) GSEA results of the correlation between gene sets in the two groups and the gene signatures reported after treatment with a ROCK inhibitor. The GSEA results for downregulated genes are in the left panel, and for upregulated genes in the right panel. In each enrichment plot, the green curve corresponds to the enrichment score (ES) curve, which is the running sum of the weighted ES. The nominal *p*-value estimates the statistical significance of a single gene set's enrichment score. Heat maps show the top 20 core genes (ranked by 'Rank Metric Score', which is the signal to noise ratio for each gene used to position the gene in the ranked list) that drive the enrichment score of the GSEA clusters. Heat maps of the total core genes are shown in Figure 3-6. GSEA, Gene Set Enrichment Analysis; ROCK, Rho-associated kinase.

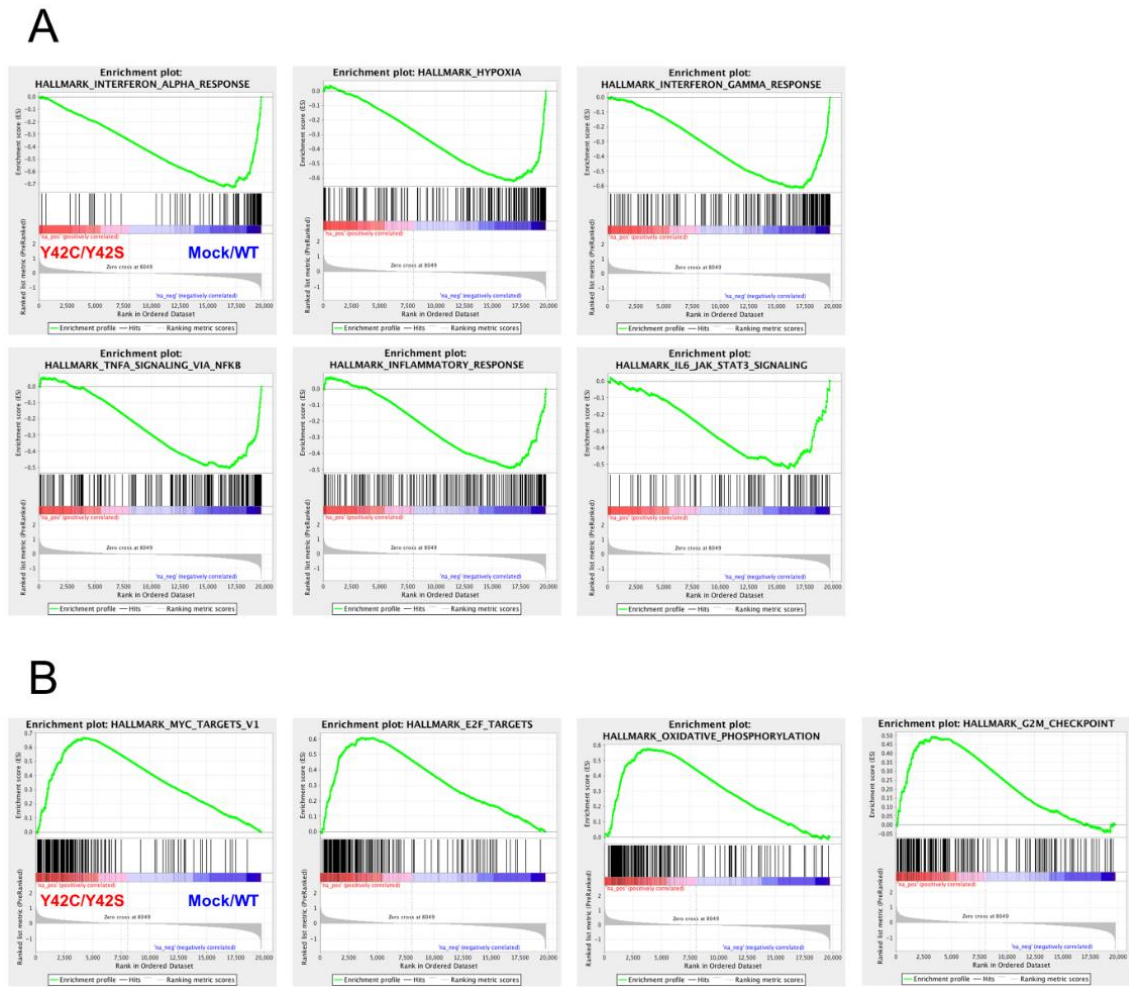


Figure 3-5: Gene Set Enrichment Analysis (GSEA) of the mock/WT cohort vs. Y42C/Y42S cohort using hallmark gene sets from the Molecular Signature Database

The enrichment plots have been categorized into those statistically significant signatures in the mock/WT group (A), and those in the Y42C/Y42S group (B). Each enrichment plot illustrates the specific gene sets associated with the difference between two cohorts.

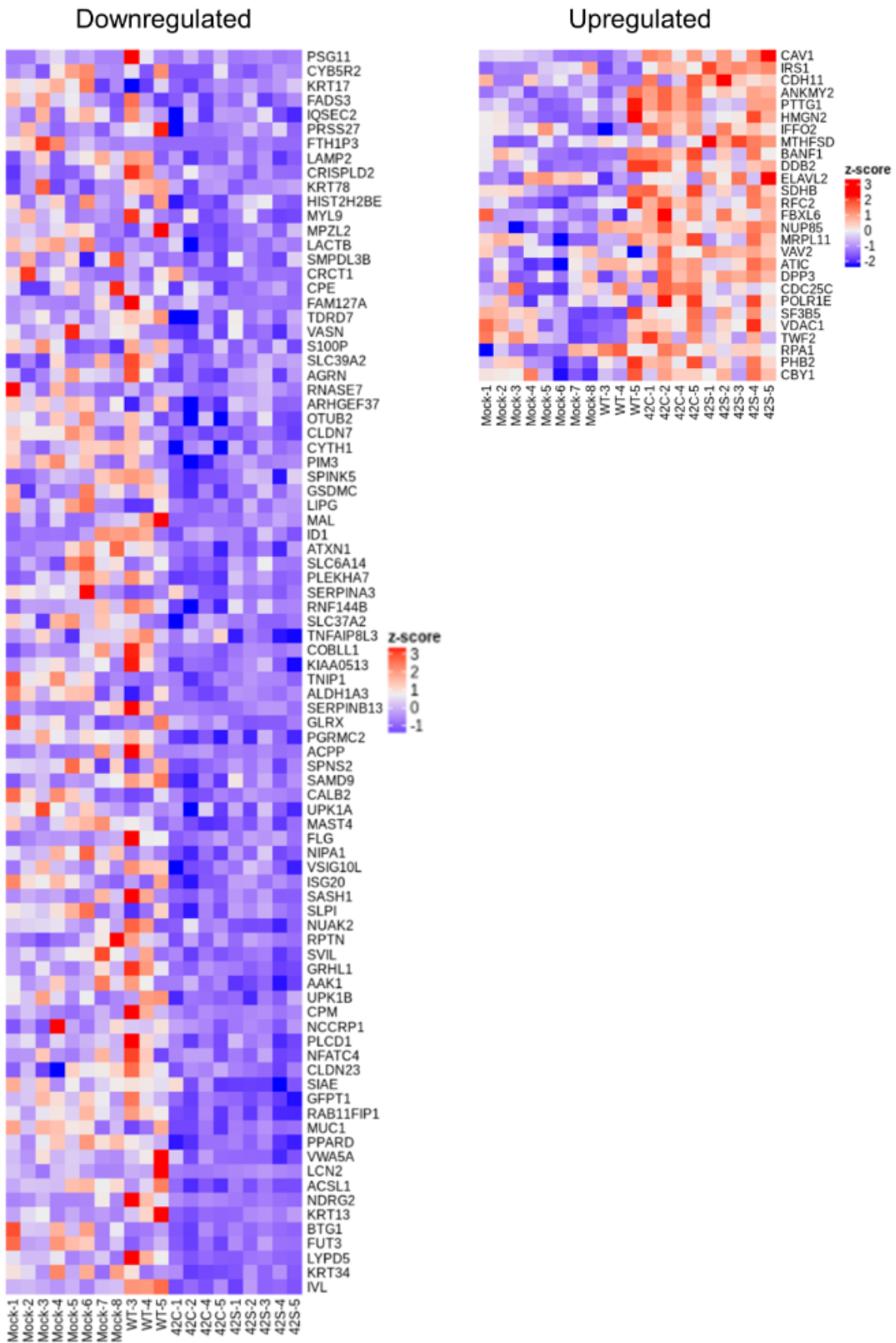


Figure 3-6: Heat maps of a GSEA of mock/WT vs. Y42C/Y42S using the gene signatures reported after treatment with a ROCK inhibitor

The genes include all the core genes that drive the enrichment score of the GSEA clusters. The results for downregulated genes are in the left panel, and for upregulated genes in the right panel.

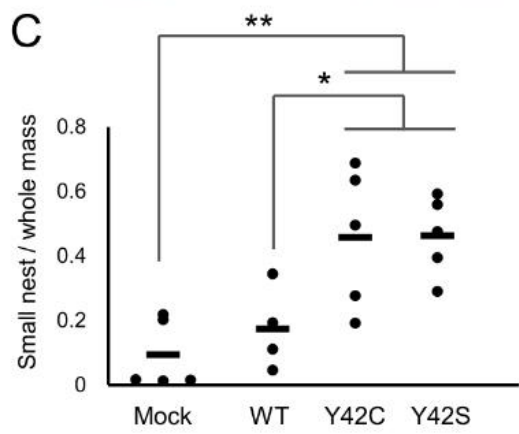
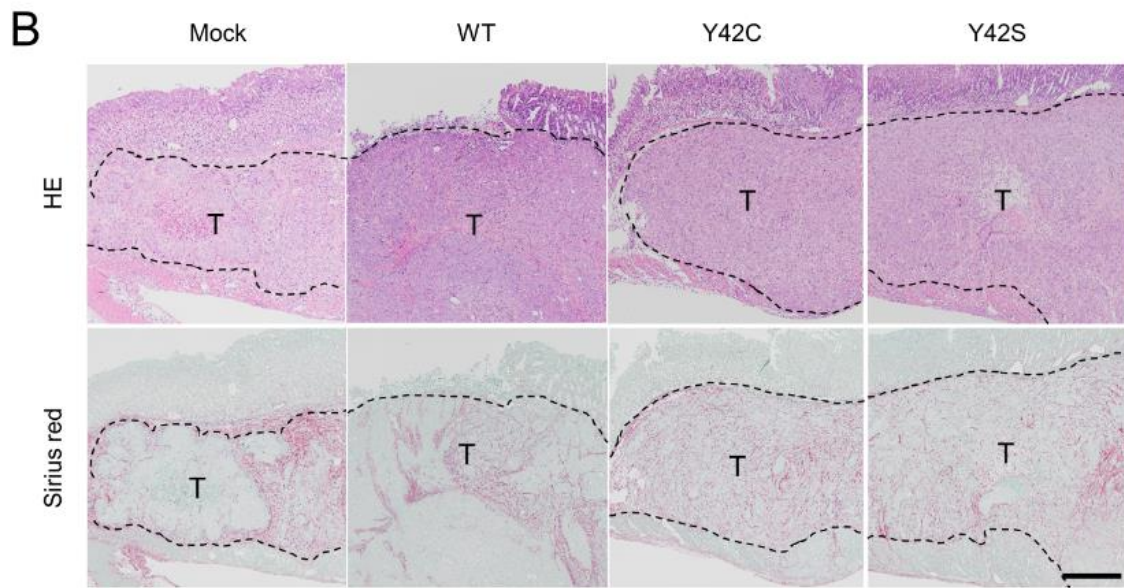
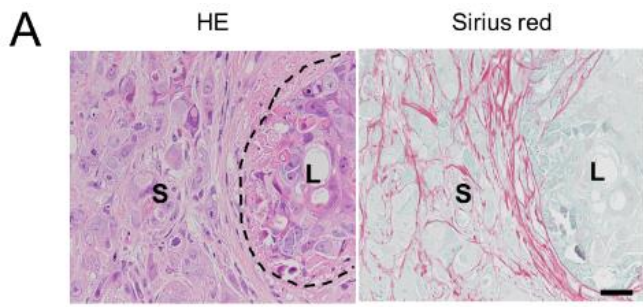


Figure 3-7: Histopathological evaluation of the formation of small tumor nests

(A) Representative images of small (S) and large (L) tumor nest areas. HE stain (left), and Sirius red stain (right). Scale bar, 100 μ m. (B) Representative images of the tissue sections in mock, WT and *RHOA* mutants. The tumor nests are circumscribed by collagen fibers. T, tumor area. Scale bar, 1 mm. HE stain (upper row), and Sirius red stain (bottom row). (C) The ratio of small tumor nest area to total tumor area. Each dot represents the ratio in a tumor tissue section from 1 animal. The bars show the average for each group. * p <0.05, ** p <0.01, one-way analysis of variance followed by a Dunnett's test.

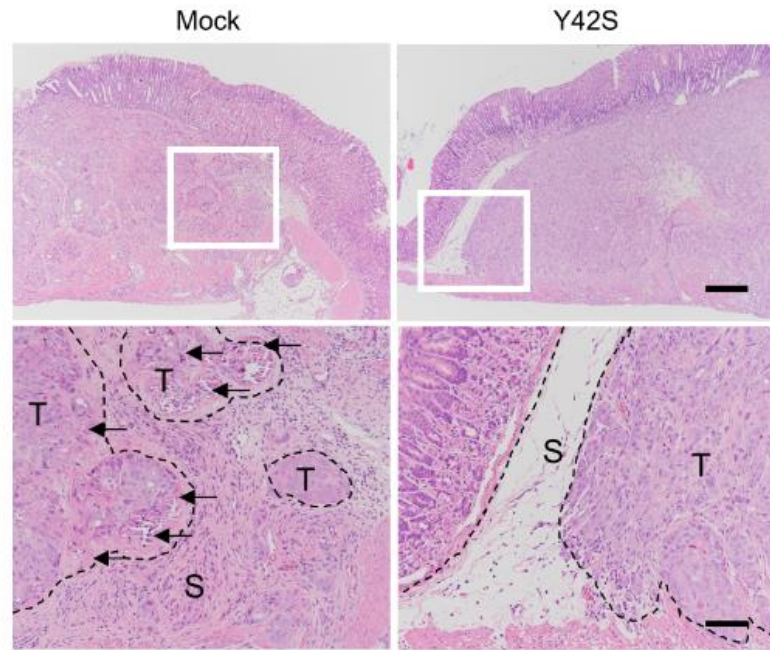
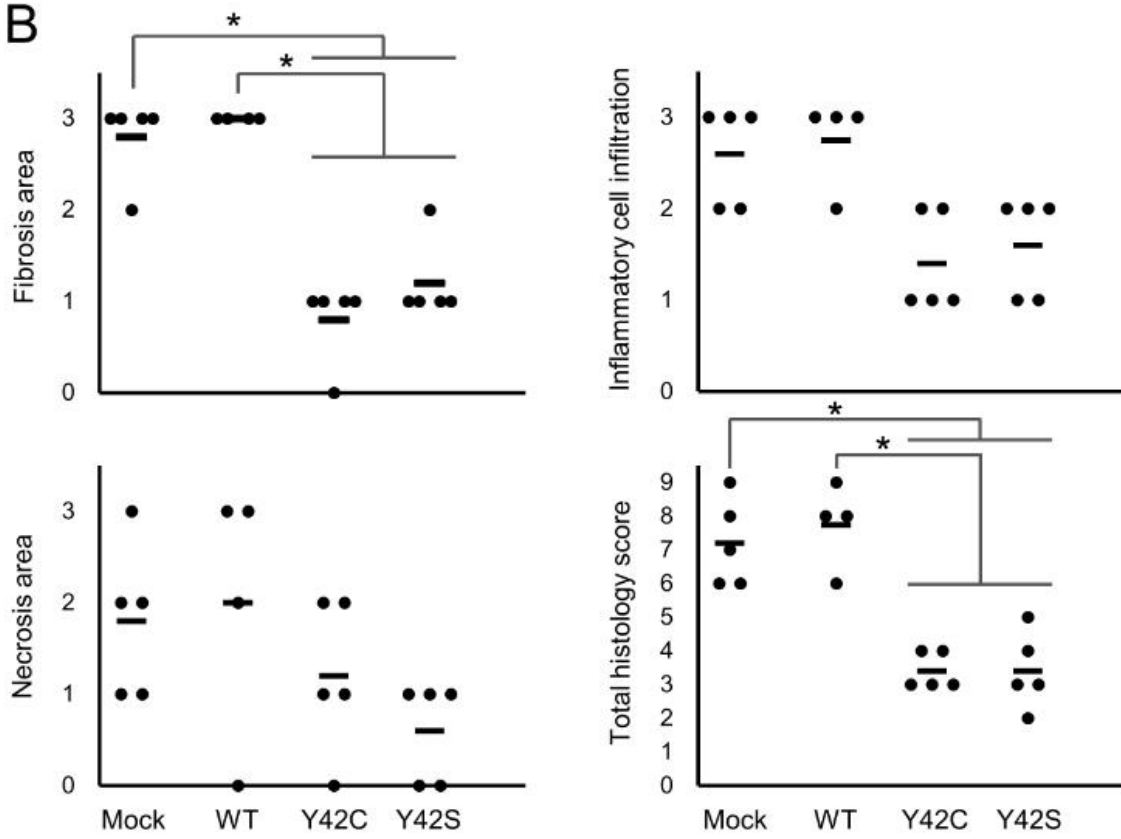
A**B**

Figure 3-9: Histological evaluation of the invasive front of tumors using HE stain

(A) Representative images of the invasive front of the tumor mass. The areas marked in squares in the upper row are shown at higher magnification in the lower row. The inflammatory cell infiltration with fibrosis observed in the stroma of the mock tumor is markedly weaker in the mutant tumor. S, stroma; T, tumor mass. Arrows show necrosis of tumor cells. Scale bar, 500 μm (upper panels) and 200 μm (lower panels). (B) Scoring for host reaction in the invasive front. Scoring criteria: 0, not observed; 1, occasionally observed; 2, moderately observed; 3, frequently observed. The total histology score is the sum of scores for the other three findings. Each dot stands for the score in a tumor tissue section from 1 animal. The bars show the average for each group. $*p < 0.05$, difference between mutant group and control group was assessed with Steel's test.

General Discussion

In this study, I evaluated the biological function of *RHOA* mutations in DGC. In chapter 1, I described that *RHOA* mutations maintained cell survival and increased cell migration through the inhibition of ROCK signaling *in vitro*. *CLG* fusions, which are mutually exclusive with *RHOA* mutations, had similar functions in cell survival and cell motility. Next, I characterized *in vivo* ORT model compared with SC model and decided that the ORT model was suitable for understanding DGC biology in chapter 2. In chapter 3, I evaluated *in vivo* functionality of *RHOA* mutations, and revealed that mutated *RHOA* induced small tumor nests, increased blood vessel formation and infiltration of macrophages within the tumor mass. Furthermore, the *RHOA*-mutated tumor cells had little antitumor host reaction in the invasive front, which is similar to the pattern of mucosal invasion in clinical *RHOA*-mutated DGC. A series of evidence indicated that *RHOA* mutations would contribute clinical DGC development and could be potential target for DGC treatment.

To obtain these results, I utilized commercially available cancer cell lines. Though I investigated DGC cell lines which have *RHOA* mutations, those cell lines are not found. DGC spread without clear polyps or ulcers, and frequently show intraperitoneal metastasis [73, 74], therefore the operable cases are limited. If tissue specimens were not obtained, it is difficult to establish DGC cell lines. Actually, some Japanese and Korean groups established cell lines from poorly differentiated gastric cancers, but they isolated cell lines from ascites fluid in most of the cases [148-152]. I substituted *RHOA* mutated cell lines from other organs, but *RHOA* mutated cell lines originated from

DGC would be more suitable for exploring DGC biology. Recent progress of endoscopic and image analysis technology has been able to detect DGC in operable stage [153-155] and would accelerate DGC research including establishment of cell line or patient derived xenograft model [156] with tissue specimens. Tumor microenvironment also critical to reveal the biology of DGC, because *RHOA* mutated cancer cells influenced host cells as shown in Chapter 3. To reduce the culture bias and retain the effects of tumor microenvironment, a three-dimensional organoid culture that enables *ex vivo* analysis of stem cell behavior and differentiation would be useful [157-161]. Seidlitz reported that human gastric cancer organoids maintained primary tumor characteristics [161]. The combination of current my evaluation model and future progress of tissue collection and culture technology would provide further understandings of DGC.

I evaluated the functions of mutated *RHOA* in DGC, but other research groups targeting different cancer types with *RHOA* mutations would provide valuable insights. Within solid tumors, esophageal squamous carcinoma is secondary frequent after DGC and *RHOA* mutations are also observed in bladder, cervical, colorectal, endometrial, and head and neck cancers [46, 162]. *RHOA* mutations in DGC were accumulated in R5, G17 and Y42, and I revealed that G17, Y42 and L57 mutations are functional but not R5 (Figure 1-1, 1-4, 1-16). Although the frequency is low, the site-specific accumulation of *RHOA* mutations like DGC was not observed in esophageal, bladder, cervical, colorectal and endometrial cancers. On the other hands, E40Q mutations were accumulated in head

and neck cancer [46]. E40 is located in effector binding region as same as Y42 [43], but the *RHOA* knockdown of E40Q mutated CJM, which is oral cavity squamous cell carcinoma cell line, did not impair cell survival (Figure 1-1). Various effector proteins interact with RHOA [58, 59], so another key molecule beside ROCK might contribute head and neck cancer development.

Apart from solid tumors, highly frequent *RHOA* mutations are observed in lymphoma such as AITL, PTCL-NOS, adult T-cell leukemia-lymphoma (ATL), Burkitt lymphoma and diffuse large B-cell lymphoma (DLBCL). The mutation spectrum is dependent on each tumor type and some mutations are common to DGC, concretely G17V in AITL and PTCL-NOS, C16R, G17V/E/R and A161P/E in ATL, R5Q/W and Y42F/H/S in Burkitt lymphoma and DLBCL [46]. RHOA is known as a key regulator of innate and adaptive immunity [163]. T cell compartment specific deletion of RhoA impaired thymocyte differentiation [164]. G17 mutations did not bind to GTP [47] and C16 locates in GTP/GDP binding site. Therefore, C16 and G17 mutations would work as dominant negative form and dysregulate the differentiation process of T cells. A161 is located in RHO-GDI binding region, so the mutations in this region might destabilize RHOA in cytoplasm [165]. As for B cell development, it is reported that the genetic deletion of RhoA in hematopoietic stem cells reduced the frequencies of B cell progenitors in the bone marrow [166]. R5 or Y42 mutations were dominant in B cell lymphoma. Because Y42 mutations would induce conformational change, it is indicated that the altered affinity to effector proteins induce RHOA signaling dysfunction. On the other hands, R5 is one of hotspot, but

not located in any functional domain. In my study, R5 mutations did not maintain cell survival and not promote cell migration (Figure 1-4, 1-16). To reveal the interaction between R5 mutants and some functional effector proteins, it would be effective to conduct an immunoprecipitation of R5 mutants compared with other mutations or WT. Fortunately, R5 mutants were relatively stable as a protein unlike G17 mutants (Figure 1-3), so this is my next challenge.

In addition to *RHOA* mutations, the genetic alterations related to TCR signaling related molecules such as *FYN*, *VAV1*, *PLCG1*, *CARD11* and *CD28* also were enriched in AITL, PTCL-NOS and ATL, and also the inactivating mutations of Gα13-dependent pathway genes including *SIPR2*, *GNAI3*, *ARHGEF1*, and *P2RY8* were accumulated in Burkitt lymphoma and DLBCL [46]. Therefore, the co-occurrence and the exclusivity against *RHOA* mutations would provide clues to identify the molecular mechanism. As I described, *RHOA* mutations and *CLG* fusions were mutually exclusive [45], so the inactivation of RHOA-ROCK signaling is one of the key pathways in DGC development. As for other genetic alterations, *CDH1* mutations were enriched in DGC but not all patients were mutually exclusive with *RHOA* mutations [43]. *CDH1* mutations are the most common germline mutations detected in hereditary diffuse gastric cancer (HDGC) syndrome [167]. It was also reported that *CDH1* and *p53* double conditional knockout mice induced DGC like carcinomas composed of poorly differentiated tumor cells and signet ring cells [168]. Because the inactivation of *CDH1* loose cell-cell interaction, I speculated that epithelial-mesenchymal transition (EMT) signaling would be

induced in *RHOA* mutated tumors. However, the gene set of EMT signaling was not enriched in ORT model (Figure 3-4). It was reported that both *RHOA* and *CDH1* involved in collective cell migration, that two or more cells retaining their cell-cell adhesion move together across the ECM [169-172]. Cancer associated fibroblasts (CAFs) have a role to lead collective migration of carcinoma cells by generating proteolytic ECM paths [173, 174]. In my study, mouse stroma cells were much invaded into *RHOA* mutated tumor mass compared with mock/WT (Figure 3-7). Therefore, the collective cell migration induced by the dysfunction of RHOA and CDH1 might be important mechanism to develop DGC.

Finally, I'd like to discuss the possibility of future therapeutics targeting the *RHOA* mutated DGC. *RHOA* does not have specific functional pocket such as kinase domain because *RHOA* is a small and a globular protein. Generally speaking, it is tough to develop the inhibitors of protein-protein interactions (PPI) such as *RHOA* and effector proteins. In the past, Shang et al. identified a Rho-specific inhibitor, Rhosin, by virtual screening [175]. Rhosin bound to the surface area sandwiching Trp58 with a submicromolar Kd and also effectively inhibited RHOA-mediated cellular function without affecting CDC42 or RAC1 signaling in cells. Although its affinity would not be sufficient in anticipation of the clinical use, virtual screening would be potential approach to develop the small molecule inhibitors targeting *RHOA* mutations. As for another approach, peptide-based inhibitors have a potential activity to inhibit PPIs [176-178]. The difficulty of peptide therapeutics is the intracellular

penetration, because their molecular size is larger than small molecule inhibitors. However, recent technologies are improving their penetration and inhibition effects [179]. Since *RHOA* mutations kept ROCK signaling inactive, the activator for ROCK signaling would be useful in *RHOA*-mutated DGC. Unfortunately, the specific activator of ROCK has not been reported. Although, I found that elevated RHOB proteins reactivated ROCK signaling and contributed cell death of the *RHOA* mutated cell line (Figure 1-6, 1-12). Some functions of RHOA are compensated by RHOB and/or RHOC in organ specific manner [53, 180, 181]. Therefore, further analysis to elucidate the activation mechanism of RHOB or RHOC would accelerate the development of therapeutics.

My studies revealed the biology of *RHOA*-mutated DGC *in vitro* and *in vivo*. I showed the histopathological similarity between *RHOA*-mutated tumors in the ORT model and clinical *RHOA*-mutated DGC. Therefore, a series of results could accelerate the understanding of clinical DGC. It is still challenging to develop effective therapeutics for DGC having *RHOA* mutations, but this is a meaningful first step to overcome *RHOA*-mutated DGC.

Acknowledgments

I am most grateful to Professor Tomoki Chiba , Professor Tetsuo Hashimoto and Assistant Professor Fuminori Tsuruta, University of Tsukuba, for their continuous guidance and valuable discussions through my doctoral program.

Further, I wish to express my sincere gratitude to Dr. Masami Suzuki, Forerunner Pharma Research Co., Ltd., for giving me the opportunity to carry out this study and for offering the appropriate advice.

Also, I am greatly indebted to Dr. Kiyotaka Nakano and Dr. Etsuko Fujii, Forerunner Pharma Research Co., Ltd., for valuable suggestions, contributions and helpful supports.

I am very thankful to Dr. Osamu Natori, Dr. Shin-ichi Funahashi and my many colleagues in Forerunner Pharma Research Co., Ltd., Chugai Pharmaceutical Co., Ltd. and Chugai Research Institute for Medical Science, Inc. for their kind cooperation and advice in my research work.

I greatly appreciate Professor Hiroyuki Aburatani, Professor Shumpei Ishikawa, Dr. Miwako Kakiuchi and Dr. Daisuke Komura, University of Tokyo, for guiding my work and valuable discussions through my studies.

Finally, I show my gratitude for my wife Yumi, and my children Haru and Sono with love for supporting my life in University of Tsukuba.

References

1. Bray F, Ferlay J, Soerjomataram I, Siegel RL, Torre LA, Jemal A. Global cancer statistics 2018: GLOBOCAN estimates of incidence and mortality worldwide for 36 cancers in 185 countries. *CA Cancer J Clin.* 68: 394-424. 2018.
2. Data source: Vital Statistics Japan-2017. Ministry of Health, Labour and Welfare. 2017
3. *Environ Health Perspect.* IARC monographs: 40 years of evaluating carcinogenic hazards to humans. 123: 507-514. 2015.
4. Pearce N, Blair A, Vineis P, Ahrens W, Andersen A, Anto JM, Armstrong BK, Baccarelli AA, Beland FA, Berrington A, Bertazzi PA, Birnbaum LS, Brownson RC, Bucher JR, Cantor KP, Cardis E, Cherrie JW, Christiani DC, Cocco P, Coggon D, Comba P, Demers PA, Dement JM, Douwes J, Eisen EA, Engel LS, Fenske RA, Fleming LE, Fletcher T, Fontham E, Forastiere F, Frentzel-Beyme R, Fritschi L, Gerin M, Goldberg M, Grandjean P, Grimsrud TK, Gustavsson P, Haines A, Hartge P, Hansen J, Hauptmann M, Heederik D, Hemminki K, Hemon D, Hertz-Picciotto I, Hoppin JA, Huff J, Jarvholm B, Kang D, Karagas MR, Kjaerheim K, Kjuus H, Kogevinas M, Kriebel D, Kristensen P, Kromhout H, Laden F, LeBailly P, LeMasters G, Lubin JH, Lynch CF, Lynge E, 't Mannetje A, McMichael AJ, McLaughlin JR, Marrett L, Martuzzi M, Merchant JA, Merler E, Merletti F, Miller A, Mirer FE, Monson R, Nordby KC, Olshan AF, Parent ME, Perera FP, Perry MJ, Pesatori AC, Pirastu R, Porta M, Pukkala E, Rice C, Richardson

- DB, Ritter L, Ritz B, Ronckers CM, Rushton L, Rusiecki JA, Rusyn I, Samet JM, Sandler DP, de Sanjose S, Schernhammer E, Costantini AS, Seixas N, Shy C, Siemiatycki J, Silverman DT, Simonato L, Smith AH, Smith MT, Spinelli JJ, Spitz MR, Stallones L, Stayner LT, Steenland K, Stenzel M, Stewart BW, Stewart PA, Symanski E, Terracini B, Tolbert PE, Vainio H, Vena J, Vermeulen R, Victora CG, Ward EM, Weinberg CR, Weisenburger D, Wesseling C, Weiderpass E, Zahm SH. A review of human carcinogens--part D: radiation. *Lancet Oncol.* 10: 751-752. 2009.
5. Diepgen TL, Islami F, Anandasabapathy, Schmitt J. Br J Dermatol. Occupational skin cancer induced by ultraviolet radiation and its prevention. *Br J Dermatol.* 167: 76-84. 2012.
 6. Shore RE. Radiation-induced skin cancer in humans. *Med Pediatr Oncol.* 36: 549-554. 2001.
 7. Liu G, Cheres P, Kamp DW. Molecular basis of asbestos-induced lung disease. *Annu Rev Pathol.* 24: 161-187. 2013.
 8. Hecht SS. Tobacco carcinogens, their biomarkers and tobacco-induced cancer. 3: 733-744. *Nat Rev Cancer.* 2003.
 9. Hitesh Singhavi, Jasjit S. Ahluwalia, Irina Stepanov, Prakash C. Gupta, Vikram Gota, Pankaj Chaturvedi, Samir S. Khariwala. Tobacco carcinogen research to aid understanding of cancer risk and influence policy. *Laryngoscope Investig Otolaryngol.* 3: 372-376. 2018.
 10. Wiencke JK. DNA adduct burden and tobacco carcinogenesis. *Oncogene.* 21: 7377391. 2002.
 11. Ewald PW, Swain Ewald HA. Infection and cancer in multicellular organisms. *Philos Trans R*

- Soc Lond B Biol Sci. 370: 20140224. 2015.
12. Stanley MA, Pett MR, Coleman N. HPV: from infection to cancer. *Biochem Soc Trans.* 35: 1456-1460. 2007.
 13. de Martel C, Maucort-Boulch D, Plummer M, Franceschi S. World-wide relative contribution of hepatitis B and C viruses in hepatocellular carcinoma. *Hepatology.* 62: 1190-1200. 2015.
 14. The EUROGAST Study Group. An international association between *Helicobacter pylori* infection and gastric cancer. *Lancet.* 341: 1359-1362. 1993.
 15. Sugiyama T, Asaka M. *Helicobacter pylori* infection and gastric cancer. *Med Electron Microsc.* 37: 149-157. 2004.
 16. Karimi P, Islami F, Anandasabapathy S, Freedman ND, Kamangar F. Gastric cancer: descriptive epidemiology, risk factors, screening, and prevention. *Cancer Epidemiol Biomarkers Prev.* 23: 700-713. 2014.
 17. Guggenheim DE, Shah MA. Gastric cancer epidemiology and risk factors. *J Surg Oncol.* 107: 230-236. 2013.
 18. Forman D, Burley VJ. Gastric cancer: global pattern of the disease and an overview of environmental risk factors. *Best Pract Res Clin Gastroenterol.* 20: 633-649. 2006.
 19. Weinstein IB. Cancer. Addiction to oncogenes--the Achilles heel of cancer. *Science.* 297: 63-64. 2002.

20. Lee EY, Muller WJ. Oncogenes and tumor suppressor genes. *Cold Spring Harb Perspect Biol.* 2: a003236. 2010.
21. Yarbrow JW. Oncogenes and cancer suppressor genes. *Semin Oncol Nurs.* 8: 30-39. 1992.
22. Orr B, Compton DA. A double-edged sword: how oncogenes and tumor suppressor genes can contribute to chromosomal instability. *Front Oncol.* 3: 164. 2013.
23. Maria Apicella, Simona Corso, Silvia Giordano. Targeted therapies for gastric cancer: failures and hopes from clinical trials. *Oncotarget.* 8: 57654-57669. 2017.
24. Bang YJ, Van Cutsem E, Feyereislova A, Chung HC, Shen L, Sawaki A, Lordick F, Ohtsu A, Omuro Y, Satoh T, Aprile G, Kulikov E, Hill J, Lehle M, Rüschoff J, Kang YK; ToGA Trial Investigators. Trastuzumab in combination with chemotherapy versus chemotherapy alone for treatment of HER2-positive advanced gastric or gastro-oesophageal junction cancer (ToGA): a phase 3, open-label, randomised controlled trial. *Lancet.* 376: 687-697. 2010.
25. Sanford M. Trastuzumab: a review of its use in HER2-positive advanced gastric cancer. *Drugs.* 73: 1605-1615. 2013.
26. Wilke H, Muro K, Van Cutsem E, Oh SC, Bodoky G, Shimada Y, Hironaka S, Sugimoto N, Lipatov O, Kim TY, Cunningham D, Rougier P, Komatsu Y, Ajani J, Emig M, Carlesi R, Ferry D, Chandrawansa K, Schwartz JD, Ohtsu A; RAINBOW Study Group. Ramucirumab plus paclitaxel versus placebo plus paclitaxel in patients with previously treated advanced gastric or

- gastro-oesophageal junction adenocarcinoma (RAINBOW): a double-blind, randomised phase 3 trial. *Lancet Oncol.* 15: 1224-1235. 2014.
27. Shitara K, Ohtsu A. Ramucirumab for gastric cancer. *Expert Rev Gastroenterol Hepatol.* 9: 133-139. 2015.
 28. *Aust Prescr.* Ramucirumab. 39: 63-64. 2016.
 29. Muro K, Chung HC, Shankaran V, Geva R, Catenacci D, Gupta S, Eder JP, Golan T, Le DT, Burtness B, McRee AJ, Lin CC, Pathiraja K, Lunceford J, Emancipator K, Juco J, Koshiji M, Bang YJ. Pembrolizumab for patients with PD-L1-positive advanced gastric cancer (KEYNOTE-012): a multicentre, open-label, phase 1b trial. *Lancet Oncol.* 17: 717-726. 2016.
 30. Kamath SD, Kalyan A, Benson AB 3rd. Pembrolizumab for the treatment of gastric cancer. *Expert Rev Anticancer Ther.* 18: 1177-1187. 2018.
 31. Kwok G, Yau TC, Chiu JW, Tse E, Kwong YL. Pembrolizumab (Keytruda). *Hum Vaccin Immunother.* 12: 2777-2789. 2016.
 32. Data source: Cancer Stat Facts: Stomach Cancer. SEER 18 2009-2015. National Cancer Institute.
 33. Lauren P. The two histological main types of gastric carcinoma: Diffuse and so-called intestinal-type carcinoma. An attempt at a histo-clinical classification. *Acta Pathol Microbiol Scand.* 64: 31-49. 1965.
 34. Polkowski W, van Sandick JW, Offerhaus GJ, ten Kate FJ, Mulder J, Obertop H, van Lanschot

- JJ. Prognostic value of Laurén classification and c-erbB-2 oncogene overexpression in adenocarcinoma of the esophagus and gastroesophageal junction. *Ann Surg Oncol.* 6: 290-297. 1999.
35. WHO Classification of Tumours of the Digestive System. Fourth Edition, IARC
36. Hu B, El Hajj N, Sittler S, Lammert N, Barnes R, Meloni-Ehrig A. Gastric cancer: Classification, histology and application of molecular pathology. *J Gastrointest Oncol.* 3: 251-261. 2012
37. Chiaravalli AM, Klersy C, Vanoli A, Ferretti A, Capella C, Solcia E. Histotype-based prognostic classification of gastric cancer. *World J Gastroenterol.* 18: 896–904. 2012.
38. Parsonnet J, Vandersteen D, Goates J, Sibley RK, Pritikin J, Chang Y. *Helicobacter pylori* infection in intestinal- and diffuse-type gastric adenocarcinomas. *J Natl Cancer Inst.* 83: 640-643. 1991.
39. Gravalos C, Jimeno A. HER2 in gastric cancer: a new prognostic factor and a novel therapeutic target. *Ann Oncol.* 19: 1523-1529. 2008.
40. Drilon A, Wang L, Arcila ME, Balasubramanian S, Greenbowe JR, Ross JS, Stephens P, Lipson D, Miller VA, Kris MG, Ladanyi M, Rizvi NA. Broad, Hybrid Capture-Based Next-Generation Sequencing Identifies Actionable Genomic Alterations in Lung Adenocarcinomas Otherwise Negative for Such Alterations by Other Genomic Testing Approaches. *Clin Cancer Res.* 21: 3631-3639. 2015.

41. He J, Abdel-Wahab O, Nahas MK, Wang K, Rampal RK, Intlekofer AM, Patel J, Krivstov A, Frampton GM, Young LE, Zhong S, Bailey M, White JR, Roels S, Deffenbaugh J, Fichtenholtz A, Brennan T, Rosenzweig M, Pelak K, Knapp KM, Brennan KW, Donahue AL, Young G, Garcia L, Beckstrom ST, Zhao M, White E, Banning V, Buell J, Iwanik K, Ross JS, Morosini D, Younes A, Hanash AM, Paietta E, Roberts K, Mullighan C, Dogan A, Armstrong SA, Mughal T, Vergilio JA, Labrecque E, Erlich R, Vietz C, Yelensky R, Stephens PJ, Miller V, van den Brink MR, Otto GA, Lipson D, Levine RL. Integrated genomic DNA/RNA profiling of hematologic malignancies in the clinical setting. *Blood*. 127: 3004-3014. 2016.
42. Li T, Kung HJ, Mack PC, Gandara DR. Genotyping and genomic profiling of non-small-cell lung cancer: implications for current and future therapies. *J Clin Oncol*. 31: 1039-1049. 2013.
43. Kakiuchi M, Nishizawa T, Ueda H, Gotoh K, Tanaka A, Hayashi A, Yamamoto S, Tatsuno K, Katoh H, Watanabe Y, Ichimura T, Ushiku T, Funahashi S, Tateishi K, Wada I, Shimizu N, Nomura S, Koike K, Seto Y, Fukayama M, Aburatani H, Ishikawa S. Recurrent gain-of-function mutations of RHOA in diffuse-type gastric carcinoma. *Nat Genet*. 46: 583-587. 2014.
44. Wang K, Yuen ST, Xu J, Lee SP, Yan HH, Shi ST, Siu HC, Deng S, Chu KM, Law S, Chan KH, Chan AS, Tsui WY, Ho SL, Chan AK, Man JL, Foglizzo V, Ng MK, Chan AS, Ching YP, Cheng GH, Xie T, Fernandez J, Li VS, Clevers H, Rejto PA, Mao M, Leung SY. Whole-genome sequencing and comprehensive molecular profiling identify new driver mutations in gastric

- cancer. *Nat Genet.* 46: 573-582. 2014.
45. Cancer Genome Atlas Research Network. Comprehensive molecular characterization of gastric adenocarcinoma. *Nature.* 513: 202-209. 2014.
46. Kataoka K, Ogawa S. Variegated RHOA mutations in human cancers. *Exp Hematol.* 44: 1123-1129. 2016.
47. Sakata-Yanagimoto M, Enami T, Yoshida K, Shiraishi Y, Ishii R, Miyake Y, Muto H, Tsuyama N, Sato-Otsubo A, Okuno Y, Sakata S, Kamada Y, Nakamoto-Matsubara R, Tran NB, Izutsu K, Sato Y, Ohta Y, Furuta J, Shimizu S, Komeno T, Sato Y, Ito T, Noguchi M, Noguchi E, Sanada M, Chiba K, Tanaka H, Suzukawa K, Nanmoku T, Hasegawa Y, Nureki O, Miyano S, Nakamura N, Takeuchi K, Ogawa S, Chiba S. Somatic RHOA mutation in angioimmunoblastic T cell lymphoma. *Nat Genet.* 46: 171-175. 2014.
48. Yoo HY, Sung MK, Lee SH, Kim S, Lee H, Park S, Kim SC, Lee B, Rho K, Lee JE, Cho KH, Kim W, Ju H, Kim J, Kim SJ, Kim WS, Lee S, Ko YH. A recurrent inactivating mutation in RHOA GTPase in angioimmunoblastic T cell lymphoma. *Nat Genet.* 46: 371-375. 2014.
49. Nagata Y, Kontani K, Enami T, Kataoka K, Ishii R, Totoki Y, Kataoka TR, Hirata M, Aoki K, Nakano K, Kitanaka A, Sakata-Yanagimoto M, Egami S, Shiraishi Y, Chiba K, Tanaka H, Shiozawa Y, Yoshizato T, Suzuki H, Kon A, Yoshida K, Sato Y, Sato-Otsubo A, Sanada M, Munakata W, Nakamura H, Hama N, Miyano S, Nureki O, Shibata T, Haga H, Shimoda K, Katada

- T, Chiba S, Watanabe T, Ogawa S. Variegated RHOA mutations in adult T-cell leukemia/lymphoma. *Blood*. 127: 596-604. 2016.
50. Manso R, Sánchez-Beato M, Monsalvo S, Gómez S, Cereceda L, Llamas P, Rojo F, Mollejo M, Menárguez J, Alves J, García-Cosío M, Piris MA, Rodríguez-Pinilla SM. The RHOA G17V gene mutation occurs frequently in peripheral T-cell lymphoma and is associated with a characteristic molecular signature. *Blood*. 123: 2893-2894. 2014.
51. Wennerberg K, Rossman KL, Der CJ. The Ras superfamily at a glance. *J Cell Sci*. 118: 843-846. 2005.
52. Cardama GA, Gonzalez N, Maggio J, Menna PL, Gomez DE. Rho GTPases as therapeutic targets in cancer (Review). *Int J Oncol*. 51: 1025-1034. 2017.
53. Wheeler AP, Ridley AJ. Why three Rho proteins? RhoA, RhoB, RhoC, and cell motility. *Exp Cell Res*. 301: 43-49. 2004.
54. Bos JL, Rehmann H, Wittinghofer A. GEFs and GAPs: critical elements in the control of small G proteins. *Cell*. 129: 865-877. 2007.
55. Hodge RG, Ridley AJ. Regulating Rho GTPases and their regulators. *Nat Rev Mol Cell Biol*. 17: 496-510. 2016
56. Stankiewicz TR, Linseman DA. Rho family GTPases: key players in neuronal development, neuronal survival, and neurodegeneration. *Front Cell Neurosci*. 8: 314. 2014.

57. Jaffe AB, Hall A. Rho GTPases: biochemistry and biology. *Annu Rev Cell Dev Biol.* 21: 247-269. 2005.
58. Bishop AL, Hall A. Rho GTPases and their effector proteins. *Biochem J.* 348: 241-255. 2000.
59. Schwartz M. Rho signalling at a glance. *J Cell Sci.* 117: 5457-5458. 2004.
60. Amano M, Nakayama M, Kaibuchi K. Rho-kinase/ROCK: A key regulator of the cytoskeleton and cell polarity. *Cytoskeleton (Hoboken).* 67: 545-554. 2010.
61. Li H, Peyrollier K, Kilic G, Brakebusch C. Rho GTPases and cancer. *Biofactors.* 40: 226-235. Dec 21. 2014.
62. Sahai E, Marshall CJ. RHO-GTPases and cancer. *Nat Rev Cancer.* 2: 133-142. 2002.
63. Fritz G, Just I, Kaina B. Rho GTPases are over-expressed in human tumors. *Int J Cancer.* 81: 682-687. 1999.
64. Tanaka A, Ishikawa S, Ushiku T, Yamazawa S, Katoh H, Hayashi A, Kunita A, Fukayama M. Frequent CLDN18-ARHGAP fusion in highly metastatic diffuse-type gastric cancer with relatively early onset. *Oncotarget.* 9: 29336-29350. 2018.
65. Shu Y, Zhang W, Hou Q, Zhao L, Zhang S, Zhou J, Song X, Zhang Y, Jiang D, Chen X, Wang P, Xia X, Liao F, Yin D, Chen X, Zhou X, Zhang D, Yin S, Yang K, Liu J, Fu L, Zhang L, Wang Y, Zhang J, An Y, Cheng H, Zheng B, Sun H, Zhao Y, Wang Y, Xie D, Ouyang L, Wang P, Zhang W, Qiu M, Fu X, Dai L, He G, Yang H, Cheng W, Yang L, Liu B, Li W, Dong B, Zhou Z, Wei Y,

- Peng Y, Xu H, Hu J. Prognostic significance of frequent CLDN18-ARHGAP26/6 fusion in gastric signet-ring cell cancer. *Nat Commun.* 9: 2447. 2018.
66. Niimi T, Nagashima K, Ward JM, Minoo P, Zimonjic DB, Popescu NC, Kimura S. claudin-18, a novel downstream target gene for the T/EBP/NKX2.1 homeodomain transcription factor, encodes lung- and stomach-specific isoforms through alternative splicing. *Mol Cell Biol.* 21: 7380-7390. 2001.
67. Sahin U, Koslowski M, Dhaene K, Usener D, Brandenburg G, Seitz G, Huber C, Türeci O. Claudin-18 splice variant 2 is a pan-cancer target suitable for therapeutic antibody development. *Clin Cancer Res.* 14: 7624-7634. 2008.
68. Yasui W, Sentani K, Motoshita J, Nakayama H. Molecular pathobiology of gastric cancer. *Scand J Surg.* 95: 225-231. 2006.
69. Eberth A, Lundmark R, Gremer L, Dvorsky R, Koessmeier KT, McMahon HT, Ahmadian MR. A BAR domain mediated autoinhibitory mechanism for RhoGAPs of the GRAF family. *Biochem J.* 417: 371-379. 2009.
70. Wu Y, Xu M, He R, Xu K, Ma Y. ARHGAP6 regulates the proliferation, migration and invasion of lung cancer cells. *Oncol Rep.* 41: 2281-2888. 2019.
71. Wangxia LV, Fang Y, Liu Y, Zhao Y, Shi Z, Zhong H. Circular RNA ARHGAP26 is over-expressed and its downregulation inhibits cell proliferation and promotes cell apoptosis in gastric

- cancer cells. *Saudi J Gastroenterol.* 25: 119-125. 2019.
72. Chen YC, Fang WL, Wang RF, Liu CA, Yang MH, Lo SS, Wu CW, Li AF, Shyr YM, Huang KH. Clinicopathological variation of lauren classification in gastric cancer. *Pathol Oncol Res.* 22: 197-202. 2016.
73. Lazăr DT, Sporea I, Dema A, Cornianu M, Lazăr E, Goldiș A, Vernic C. Gastric cancer: correlation between clinicopathological factors and survival of patients. II. *Rom J Morphol Embryol.* 50: 185-194. 2009.
74. Piazuolo MB. Gastric cancer: overview. *Colomb Med.* 44: 192-201. 2013.
75. Tönges L, Koch JC, Bähr M, Lingor P. ROCKing Regeneration: Rho kinase inhibition as molecular target for neurorestoration. *Front Mol Neurosci.* 4: 39. 2011.
76. O'Connor K, Chen M. Dynamic functions of RhoA in tumor cell migration and invasion. *Small GTPases.* 4: 141-147. 2013.
77. Jelen F, Lachowicz P, Apostoluk W, Mateja A, Derewenda ZS, Otlewski J. Dissecting the thermodynamics of GAPRhoA interactions. *J Struct Biol.* 165: 10-18. 2009.
78. Pylayeva-Gupta Y, Grabocka E, Bar-Sagi D. RAS oncogenes: weaving a tumorigenic web. *Nat Rev Cancer.* 11: 761-774. 2011.
79. Prior IA, Lewis PD, Mattos C. A comprehensive survey of Ras mutations in cancer. *Cancer Res.* 72: 2457-2467. 2012.

80. Kawazu M, Ueno T, Kontani K, Ogita Y, Ando M, Fukumura K, Yamato A, Soda M, Takeuchi K, Miki Y, Yamaguchi H, Yasuda T, Naoe T, et al. Transforming mutations of RAC guanosine triphosphatases in human cancers. *Proc Natl Acad Sci USA*. 110: 3029-3034. 2013.
81. Watson IR, Li L, Cabeceiras PK, Mahdavi M, Gutschner T, Genovese G, Wang G, Fang Z, Tepper JM, Stemke-Hale K, Tsai KY, Davies MA, Mills GB, Chin L. The RAC1 P29S hotspot mutation in melanoma confers resistance to pharmacological inhibition of RAF. *Cancer Res*. 74: 4845-4852. 2014.
82. Vogelstein B, Papadopoulos N, Velculescu VE, Zhou S, Diaz LA Jr, Kinzler KW. Cancer genome landscapes. *Science*. 339: 1546-1558. 2013.
83. O'Hayre M, Inoue A, Kufareva I, Wang Z, Mikelis CM, Drummond RA, Avino S, Finkel K, Kalim KW, DiPasquale G, Guo F, Aoki J, Zheng Y, et al. Inactivating mutations in GNA13 and RHOA in Burkitt's lymphoma and diffuse large B-cell lymphoma: a tumor suppressor function for the Galpha13/RhoA axis in B cells. *Oncogene*. 35: 3771-3780. 2016.
84. Ho TT, Merajver SD, Lapiere CM, Nusgens BV, Deroanne CF. RhoA-GDP regulates RhoB protein stability. Potential involvement of RhoGDIalpha. *J Biol Chem*. 283: 21588-21598. 2008.
85. Simpson KJ, Dugan AS, Mercurio AM. Functional analysis of the contribution of RhoA and RhoC GTPases to invasive breast carcinoma. *Cancer Res*. 64: 8694-8701. 2004.
86. Claassen DA, Desler MM, Rizzino A. ROCK inhibition enhances the recovery and growth of

- cryopreserved human embryonic stem cells and human induced pluripotent stem cells. *Mol Reprod Dev.* 76: 722-732. 2009.
87. Ohgushi M, Matsumura M, Eiraku M, Murakami K, Aramaki T, Nishiyama A, Muguruma K, Nakano T, Suga H, Ueno M, Ishizaki T, Suemori H, Narumiya S, et al. Molecular pathway and cell state responsible for dissociation-induced apoptosis in human pluripotent stem cells. *Cell Stem Cell.* 7: 225-239. 2010.
88. Hidalgo-Carcedo C, Hooper S, Chaudhry SI, Williamson P, Harrington K, Leitinger B, Sahai E. Collective cell migration requires suppression of actomyosin at cell-cell contacts mediated by DDR1 and the cell polarity regulators Par3 and Par6. *Nat Cell Biol.* 13: 49-58. 2011.
89. Cho SG, Li D, Stafford LJ, Luo J, Rodriguez-Villanueva M, Wang Y, Liu M. KiSS1 suppresses TNF α -induced breast cancer cell invasion via an inhibition of RhoA-mediated NF- κ B activation. *J Cell Biochem.* 107: 1139-1149. 2009.
90. Murray D, Horgan G, Macmathuna P, Doran P. NET1-mediated RhoA activation facilitates lysophosphatidic acid-induced cell migration and invasion in gastric cancer. *Br J Cancer.* 99: 1322-1329. 2008.
91. Bibby MC. Orthotopic models of cancer for preclinical drug evaluation: advantages and disadvantages. *Eur J Cancer.* 40: 852-857. 2004.
92. Loi M, Di Paolo D, Becherini P, Zorzoli A, Perri P, Carosio R, Cilli M, Ribatti D, Brignole C,

- Pagnan G, Ponzoni M, Pastorino F. The use of the orthotopic model to validate antivascular therapies for cancer. *Int J Dev Biol.* 55: 547-555. 2011.
93. Zhan B, Wen S, Lu J, Shen G, Lin X, Feng J, Huang H. Identification and causes of metabonomic difference between orthotopic and subcutaneous xenograft of pancreatic cancer. *Oncotarget.* 8: 61264-61281. 2017.
94. Hiroshima Y, Zhang Y, Zhang N, Uehara F, Maawy A, Murakami T, Mii S, Yamamoto M, Miwa S, Yano S, Momiyama M, Mori R, Matsuyama R, Chishima T, Tanaka K, Ichikawa Y, Bouvet M, Endo I, Hoffman RM. Patient-derived orthotopic xenograft (PDOX) nude mouse model of soft-tissue sarcoma more closely mimics the patient behavior in contrast to the subcutaneous ectopic model. *Anticancer Res.* 35: 697-701. 2015.
95. Killion JJ, Radinsky R, Fidler IJ. Orthotopic models are necessary to predict therapy of transplantable tumors in mice. *Cancer Metastasis Rev.* 17: 279-284. 1998.
96. Igarashi K, Kawaguchi K, Kiyuna T, Murakami T, Miwa S, Nelson SD, Dry SM, Li Y, Singh A, Kimura H, Hayashi K, Yamamoto N, Tsuchiya H, Eilber FC, Hoffman RM. Patient-derived orthotopic xenograft (PDOX) mouse model of adult rhabdomyosarcoma invades and recurs after resection in contrast to the subcutaneous ectopic model. *Cell Cycle.* 16: 91-94. 2017.
97. Dai L, Lu C, Yu XI, Dai LJ, Zhou JX. Construction of orthotopic xenograft mouse models for human pancreatic cancer. *Exp Ther Med.* 10: 1033-1038. 2015.

98. Du Q, Jiang L, Wang XQ, Pan W, She FF, Chen YL. Establishment of and comparison between orthotopic xenograft and subcutaneous xenograft models of gallbladder carcinoma. *Asian Pac J Cancer Prev.* 15: 3747-3752. 2014.
99. Zhang Y, Toneri M, Ma H, Yang Z, Bouvet M, Goto Y, Seki N, Hoffman RM. RealTime GFP Intravital Imaging of the Differences in Cellular and Angiogenic Behavior of Subcutaneous and Orthotopic Nude-Mouse Models of Human PC-3 Prostate Cancer. *J Cell Biochem.* 117: 2546-2551. 2016.
100. Furukawa T, Kubota T, Watanabe M, Kitajima M, Hoffman RM. Orthotopic transplantation of histologically intact clinical specimens of stomach cancer to nude mice: correlation of metastatic sites in mouse and individual patient donors. *Int J Cancer.* 53: 608-612. 1993.
101. Fung AS, Lee C, Yu M, Tannock IF. The effect of chemotherapeutic agents on tumor vasculature in subcutaneous and orthotopic human tumor xenografts. *BMC Cancer.* 15: 112. 2015.
102. Song C, Hong BJ, Bok S, Lee CJ, Kim YE, Jeon SR, Wu HG, Lee YS, Cheon GJ, Paeng JC, Carlson DJ, Kim HJ, Ahn GO. Real-time Tumor Oxygenation Changes After Single High-dose Radiation Therapy in Orthotopic and Subcutaneous Lung Cancer in Mice: Clinical Implication for Stereotactic Ablative Radiation Therapy Schedule Optimization. *Int J Radiat Oncol Biol Phys.* 95: 1022-1031. 2016.
103. Fidler IJ, Wilmanns C, Staroselsky A, Radinsky R, Dong Z, Fan D. Modulation of tumor cell

- response to chemotherapy by the organ environment. *Cancer Metastasis Rev.* 13: 209-222. 1994.
104. Komura D, Isagawa T, Kishi K, Suzuki R, Sato R, Tanaka M, Katoh H, Yamamoto S, Tatsuno K, Fukayama M, Aburatani H, Ishikawa S. CASTIN: a system for comprehensive analysis of cancer-stromal interactome. *BMC Genomics.* 17: 899. 2016.
105. Makalowski W, Zhang J, Boguski MS. Comparative analysis of 1196 orthologous mouse and human full-length mRNA and protein sequences. *Genome Res.* 6: 846-857. 1996.
106. Bainer R, Frankenberger C, Rabe D, An G, Gilad Y, Rosner MR. Gene expression in local stroma reflects breast tumor states and predicts patient outcome. *Sci Rep.* 6: 39240. 2016.
107. Rockett JC, Larkin K, Darnton SJ, Morris AG, Matthews HR. Five newly established oesophageal carcinoma cell lines: phenotypic and immunological characterization. *Br J Cancer.* 75: 258-263. 1997.
108. Hoover M, Adamian Y, Brown M, Maawy A, Chang A, Lee J, Gharibi A, Katz MH, Fleming J, Hoffman RM, Bouvet M, Doebler R, Kelber JA. A novel method for RNA extraction from FFPE samples reveals significant differences in biomarker expression between orthotopic and subcutaneous pancreatic cancer patient-derived xenografts. *Oncotarget.* 8: 5885-5894. 2017.
109. Jinawath N, Furukawa Y, Hasegawa S, Li M, Tsunoda T, Satoh S, Yamaguchi T, Imamura H, Inoue M, Shiozaki H, Nakamura Y. Comparison of gene-expression profiles between diffuse- and intestinal-type gastric cancers using a genome-wide cDNA microarray. *Oncogene.* 23: 6830-6844.

2004.

110. Smith JP, Nadella S, Osborne N. Gastrin and Gastric Cancer. *Cell Mol Gastroenterol Hepatol.* 4: 75-83. 2017.

111. Rosano L, Spinella F, Bagnato A. Endothelin 1 in cancer: biological implications and therapeutic opportunities. *Nat Rev Cancer.* 13: 637-651. 2013.

112. See AL, Chong PK, Lu SY, Lim YP. CXCL3 is a potential target for breast cancer metastasis. *Curr Cancer Drug Targets.* 14: 294-309. 2014.

113. Wells JE, Howlett M, Cole CH, Kees UR. Deregulated expression of connective tissue growth factor (CTGF/CCN2) is linked to poor outcome in human cancer. *Int J Cancer.* 137: 504-511. 2015.

114. Li J, Ye L, Owen S, Weeks HP, Zhang Z, Jiang WG. Emerging role of CCN family proteins in tumorigenesis and cancer metastasis (Review). *Int J Mol Med.* 36: 14511463. 2015.

115. Zhuang X, Zhang H, Li X, Li X, Cong M, Peng F, Yu J, Zhang X, Yang Q, Hu G. Differential effects on lung and bone metastasis of breast cancer by Wnt signalling inhibitor DKK1. *Nat Cell Biol.* 19: 1274-1285. 2017.

116. Hu G, Zeng W, Xia Y. TWEAK/Fn14 signaling in tumors. *Tumour Biol.* 39: 1010428317714624. 2017.

117. Waldum HL, Sagatun L, Mjones P. Gastrin and Gastric Cancer. *Front Endocrinol (Lausanne).* 8:

1. 2017.
118. Waldum HL1, Brenna E, Sandvik AK. Relationship of ECL cells and gastric neoplasia. *Yale J Biol Med.* 71: 325-335. 1998.
119. Ma J, Shen H, Kapesa L, Zeng S. Lauren classification and individualized chemotherapy in gastric cancer. *Oncol Lett.* 11: 2959-2964. 2016.
120. Ushiku T, Ishikawa S, Kakiuchi M, Tanaka A, Katoh H, Aburatani H, Lauwers GY, Fukayama M. RHOA mutation in diffuse-type gastric cancer: a comparative clinicopathology analysis of 87 cases. *Gastric cancer.* 19: 403-411. 2016.
121. Nishizawa T, Nakano K, Harada A, Kakiuchi M, Funahashi SI, Suzuki M, Ishikawa S, Aburatani H. DGC-specific RHOA mutations maintained cancer cell survival and promoted cell migration via ROCK inactivation. *Oncotarget.* 9: 23198-23207. 2018.
122. Cespedes MV, Casanova I, Parreno M, Mangués R. Mouse models in oncogenesis and cancer therapy. *Clin Transl Oncol.* 8: 318-329. 2006.
123. Nakano K, Nishizawa T, Komura D, Fujii E, Monnai M, Kato A, Funahashi SI, Ishikawa S, Suzuki M. Difference in morphology and interactome profiles between orthotopic and subcutaneous gastric cancer xenograft models. *J Toxicol Pathol.* 31: 293-300. 2018.
124. Junttila MR, de Sauvage FJ. Influence of tumour micro-environment heterogeneity on therapeutic response. *Nature.* 501: 346-354. 2013.

125. Motoyama T, Hojo H, Watanabe H. Comparison of seven cell lines derived from human gastric carcinomas. *Acta Pathol Jpn.* 36: 65-83. 1986.
126. Busuttill RA, Liu DS, Di Costanzo N, Schroder J, Mitchell C, Boussioutas A. An orthotopic mouse model of gastric cancer invasion and metastasis. *Sci Rep.* 8: 825. 2018.
127. Yanagihara K, Takigahira M, Tanaka H, Komatsu T, Fukumoto H, Koizumi F, Nishio K, Ochiya T, Ino Y, Hirohashi S. Development and biological analysis of peritoneal metastasis mouse models for human scirrhous stomach cancer. *Cancer Sci.* 96: 323-332. 2005.
128. Gu Z, Eils R, Schlesner M. Complex heatmaps reveal patterns and correlations in multidimensional genomic data. *Bioinformatics.* 32: 2847-2849. 2016.
129. Langmead B, Trapnell C, Pop M, Salzberg SL. Ultrafast and memory-efficient alignment of short DNA sequences to the human genome. *Genome Biol.* 10: R25. 2009.
130. Love MI, Huber W, Anders S. Moderated estimation of fold change and dispersion for RNA-seq data with DESeq2. *Genome Biol.* 15: 550. 2014.
131. Subramanian A, Tamayo P, Mootha VK, Mukherjee S, Ebert BL, Gillette MA, Paulovich A, Pomeroy SL, Golub TR, Lander ES, Mesirov JP. Gene set enrichment analysis: a knowledge-based approach for interpreting genome-wide expression profiles. *Proc Natl Acad Sci USA.* 102: 15545-15550. 2005.
132. Mootha VK, Lindgren CM, Eriksson KF, Subramanian A, Sihag S, Lehar J, Puigserver P,

- Carlsson E, Ridderstråle M, Laurila E, Houstis N, Daly MJ, Patterson N, Mesirov JP, Golub TR, Tamayo P, Spiegelman B, Lander ES, Hirschhorn JN, Altshuler D, Groop LC. PGC-1alpha-responsive genes involved in oxidative phosphorylation are coordinately downregulated in human diabetes. *Nat Genet.* 34: 267-273. 2003.
133. Chapman S, McDermott DH, Shen K, Jang MK, McBride AA. The effect of Rho kinase inhibition on long-term keratinocyte proliferation is rapid and conditional. *Stem Cell Res Ther.* 5: 60. 2014.
134. Suzuki M KK, Adachi K, Ogawa Y, Yorozu K, Fujii E, Misawa Y, Sugimoto T. Combination of fixation using PLP fixative and embedding in paraffin by the AMeX method is useful for histochemical studies in assessment of immunotoxicity. *J Toxicol Sci.* 27: 165-172. 2002.
135. Sato Y, Mukai K, Watanabe S, Goto M, Shimosato Y. The AMeX method. A simplified technique of tissue processing and paraffin embedding with improved preservation of antigens for immunostaining. *Am J Pathol.* 125: 431-435. 1986.
136. Corliss BA, Azimi MS, Munson JM, Peirce SM, Murfee WL. Macrophages: An Inflammatory Link Between Angiogenesis and Lymphangiogenesis. *Microcirculation.* 23: 95-121. 2016.
137. Squadrito ML, De Palma M. Macrophage regulation of tumor angiogenesis: implications for cancer therapy. *Mol Aspects Med.* 32: 123-145. 2011.
138. Madeddu C, Gramignano G, Kotsonis P, Coghe F, Atzeni V, Scartozzi M, Macciò A. Microenvironmental M1 tumor-associated macrophage polarization influences cancer-related

- anemia in advanced ovarian cancer: key role of interleukin-6. *Haematologica*. 103: e388-e391. 2018.
139. Mantovani A, Allavena P. The interaction of anticancer therapies with tumor-associated macrophages. *J Exp Med*. 212: 435-445. 2015.
140. Quatromoni JG, Eruslanov E. Tumor-associated macrophages: function, phenotype, and link to prognosis in human lung cancer. *Am J Transl Res*. 4: 376-389. 2012.
141. Yin S, Huang J, Li Z, Zhang J, Luo J, Lu C, Xu H, Xu H. The Prognostic and Clinicopathological Significance of Tumor-Associated Macrophages in Patients with Gastric Cancer: A Meta-Analysis. *PloS One*. 12: e0170042. 2017.
142. Sainz B Jr, Carron E, Vallespinós M, Machado HL. Cancer Stem Cells and Macrophages: Implications in Tumor Biology and Therapeutic Strategies. *Mediators Inflamm*. 2016: 9012369. 2016.
143. Domschke G, Gleissner CA. CXCL4-induced macrophages in human atherosclerosis. *Cytokine*. 122: 154141. 2019.
144. Chávez-Galán L, Olleros ML, Vesin D, Garcia I. Much More than M1 and M2 Macrophages, There are also CD169(+) and TCR(+) Macrophages. *Front Immunol*. 6: 263. 2015.
145. Chung W, Eum HH, Lee HO, Lee KM, Lee HB, Kim KT, Ryu HS, Kim S, Lee JE, Park YH, Kan Z, Han W, Park WY. Single-cell RNA-seq enables comprehensive tumour and immune cell

- profiling in primary breast cancer. *Nat Commun.* 8: 15081. 2017.
146. Azizi E, Carr AJ, Plitas G, Cornish AE, Konopacki C, Prabhakaran S, Nainys J, Wu K, Kiseliovas V, Setty M, Choi K, Fromme RM, Dao P, McKenney PT, Wasti RC, Kadaveru K, Mazutis L, Rudensky AY, Pe'er D. Single-Cell Map of Diverse Immune Phenotypes in the Breast Tumor Microenvironment. *Cell.* 174: 1293-1308 e1236. 2018.
147. Lambrechts D, Wauters E, Boeckx B, Aibar S, Nittner D, Burton O, Bassez A, Decaluwé H, Pircher A, Van den Eynde K, Weynand B, Verbeken E, De Leyn P, Liston A, Vansteenkiste J, Carmeliet P, Aerts S, Thienpont B. Phenotype molding of stromal cells in the lung tumor microenvironment. *Nat Med.* 24: 1277-1289. 2018.
148. Kubo T. Establishment and characterization of a new gastric cancer cell line (OCUM-1), derived from Borrmann type IV tumor. *Nihon Geka Gakkai Zasshi.* 92: 1451-1460. 1991.
149. Yashiro M, Chung YS, Nishimura S, Yamada N, Sawada T, Kubo T, Nakata B, Sowa M. Establishment of a new scirrhous gastric cancer cell line OCUM-2M from a primary gastric tumor. *Nihon Shokakibyō Gakkai Zasshi.* 92: 199-205. 1995.
150. Park JG, Yang HK, Kim WH, Chung JK, Kang MS, Lee JH, Oh JH, Park HS, Yeo KS, Kang SH, Song SY, Kang YK, Bang YJ, Kim YH, Kim JP. Establishment and characterization of human gastric carcinoma cell lines. *Int J Cancer.* 70: 443-449. 1997.
151. Park JG. SNU cell lines and their application for cancer research. *Gan To Kagaku Ryoho.* 29: 89-

98. 2002.
152. Yashiro M, Matsuoka T, Ohira M. The significance of scirrhous gastric cancer cell lines: the molecular characterization using cell lines and mouse models. *Hum Cell*. 31: 271-281. 2018.
153. Yao K. Clinical Application of Magnifying Endoscopy with Narrow-Band Imaging in the Stomach. *Clin Endosc*. 48: 481-490. 2015.
154. Kim JW. Usefulness of Narrow-Band Imaging in Endoscopic Submucosal Dissection of the Stomach. *Clin Endosc*. 51: 527-533. 2018.
155. Horiuchi Y, Aoyama K, Tokai Y, Hirasawa T, Yoshimizu S, Ishiyama A, Yoshio T, Tsuchida T, Fujisaki J, Tada T. Convolutional Neural Network for Differentiating Gastric Cancer from Gastritis Using Magnified Endoscopy with Narrow Band Imaging. *Dig Dis Sci*. 2019.
156. Kuwata T, Yanagihara K, Iino Y, Komatsu T, Ochiai A, Sekine S, Taniguchi H, Katai H, Kinoshita T, Ohtsu A. Establishment of Novel Gastric Cancer Patient-Derived Xenografts and Cell Lines: Pathological Comparison between Primary Tumor, Patient-Derived, and Cell-Line Derived Xenografts. *Cells*. 8: E585. 2019.
157. Weeber F, Ooft SN, Dijkstra KK, Voest EE. Tumor Organoids as a Pre-clinical Cancer Model for Drug Discovery. *Cell Chem Biol*. 24: 1092-1100. 2017.
158. Lin M, Gao M, Cavnar MJ, Kim J. Utilizing gastric cancer organoids to assess tumor biology and personalize medicine. *World J Gastrointest Oncol*. 11: 509-517. 2019.

159. Steele NG, Chakrabarti J, Wang J, Biesiada J, Holokai L, Chang J, Nowacki LM, Hawkins J, Mahe M, Sundaram N, Shroyer N, Medvedovic M, Helmrath M, Ahmad S, Zavros Y. An Organoid-Based Preclinical Model of Human Gastric Cancer. *Cell Mol Gastroenterol Hepatol.* 7: 161-184. 2019.
160. Yan HHN, Siu HC, Law S, Ho SL, Yue SSK, Tsui WY, Chan D, Chan AS, Ma S, Lam KO, Bartfeld S, Man AHY, Lee BCH, Chan ASY, Wong JWH, Cheng PSW, Chan AKW, Zhang J, Shi J, Fan X, Kwong DLW, Mak TW, Yuen ST, Clevers H, Leung SY. A Comprehensive Human Gastric Cancer Organoid Biobank Captures Tumor Subtype Heterogeneity and Enables Therapeutic Screening. *Cell Stem Cell.* 23: 882-897. 2018.
161. Seidlitz T, Merker SR, Rothe A, Zakrzewski F, von Neubeck C, Grützmann K, Sommer U, Schweitzer C, Schölch S, Uhlemann H, Gaebler AM, Werner K, Krause M, Baretton GB, Welsch T, Koo BK, Aust DE, Klink B, Weitz J, Stange DE. Human gastric cancer modelling using organoids. *Gut.* 68: 207-217. 2019.
162. Lawrence MS, Stojanov P, Mermel CH, Robinson JT, Garraway LA, Golub TR, Meyerson M, Gabriel SB, Lander ES, Getz G. Nature. Discovery and saturation analysis of cancer genes across 21 tumour types. 505: 495-501. 2014.
163. Bros M, Haas K, Moll L, Grabbe S. RhoA as a Key Regulator of Innate and Adaptive Immunity. *Cells.* 8: E733. 2019.

164. Zhang S., Konstantinidis D.G., Yang J.Q., Mizukawa B., Kalim K., Lang R.A., Kalfa T.A., Zheng Y., Guo F. Gene targeting RhoA reveals its essential role in coordinating mitochondrial function and thymocyte development. *J. Immunol.* 193: 5973-5982. 2014.
165. Boivin D, Bilodeau D, Béliveau R. Regulation of cytoskeletal functions by Rho small GTP-binding proteins in normal and cancer cells. *Can J Physiol Pharmacol.* 74: 801-810. 1996.
166. Zhang S, Zhou X, Lang RA, Guo F. RhoA of the Rho family small GTPases is essential for B lymphocyte development. *PLoS ONE.* 7: e33773. 2012.
167. Luo W, Fedda F, Lynch P, Tan D. CDH1 Gene and Hereditary Diffuse Gastric Cancer Syndrome: Molecular and Histological Alterations and Implications for Diagnosis And Treatment. *Front Pharmacol.* 9: 1421. 2018.
168. Shimada S, Mimata A, Sekine M, Mogushi K, Akiyama Y, Fukamachi H, Jonkers J, Tanaka H, Eishi Y, Yuasa Y. Synergistic tumour suppressor activity of E-cadherin and p53 in a conditional mouse model for metastatic diffuse-type gastric cancer. *Gut.* 61: 344-353. 2012.
169. Zegers MM, Friedl P. Rho GTPases in collective cell migration. *Small GTPases.* 5: e28997. 2014.
170. Ilina O, Friedl P. Mechanisms of collective cell migration at a glance. *J Cell Sci.* 122: 3203-3208. 2009.
171. Hwang S, Zimmerman NP, Agle KA, Turner JR, Kumar SN, Dwinell MB. E-cadherin is critical for collective sheet migration and is regulated by the chemokine CXCL12 protein during

- restitution. *J Biol Chem.* 287: 22227-22240. 2012.
172. Elisha Y, Kalchenko V, Kuznetsov Y, Geiger B. Dual role of E-cadherin in the regulation of invasive collective migration of mammary carcinoma cells. *Sci Rep.* 8: 4986. 2018.
173. Gaggioli C, Hooper S, Hidalgo-Carcedo C, Grosse R, Marshall JF, Harrington K, Sahai E. Fibroblast-led collective invasion of carcinoma cells with differing roles for RhoGTPases in leading and following cells. *Nat Cell Biol.* 9: 1392-1400. 2007.
174. Calvo F, Ege N, Grande-Garcia A, Hooper S, Jenkins RP, Chaudhry SI, Harrington K, Williamson P, Moeendarbary E, Charras G, Sahai E. Mechanotransduction and YAP-dependent matrix remodelling is required for the generation and maintenance of cancer-associated fibroblasts. *Nat Cell Biol.* 15: 637-646. 2013.
175. Shang X, Marchioni F, Sipes N, Evelyn CR, Jerabek-Willemsen M, Duhr S, Seibel W, Wortman M, Zheng Y. Rational design of small molecule inhibitors targeting RhoA subfamily Rho GTPases. *Chem Biol.* 19: 699-710. 2012.
176. Fosgerau K, Hoffmann T. Peptide therapeutics: current status and future directions. *Drug Discov Today.* 20: 122-128. 2015.
177. Wójcik P, Berlicki Ł. Peptide-based inhibitors of protein-protein interactions. *Bioorg Med Chem Lett.* 26: 707-713. 2016.
178. Ali AM, Atmaj J, Van Oosterwijk N, Groves MR, Dömling A. Stapled Peptides Inhibitors: A New

Window for Target Drug Discovery. *Comput Struct Biotechnol J.* 17: 263-281. 2019.

179. Hoffmann K, Milech N, Juraja SM, Cunningham PT, Stone SR, Francis RW, Anastasas M, Hall CM, Heinrich T, Bogdawa HM, Winslow S, Scobie MN, Dewhurst RE, Florez L, Ong F, Kerfoot M, Champain D, Adams AM, Fletcher S, Viola HM, Hool LC, Connor T, Longville BAC, Tan YF, Kroeger K, Morath V, Weiss GA, Skerra A, Hopkins RM, Watt PM. A platform for discovery of functional cell-penetrating peptides for efficient multi-cargo intracellular delivery. *Sci Rep.* 8: 12538. 2018.
180. Melendez J, Stengel K, Zhou X, Chauhan BK, Debidda M, Andreassen P, Lang RA, Zheng Y. RhoA GTPase is dispensable for actomyosin regulation but is essential for mitosis in primary mouse embryonic fibroblasts. *J Biol Chem.* 286: 15132-15137. 2011.
181. Leslie JR, Imai F, Zhou X, Lang RA, Zheng Y, Yoshida Y. RhoA is dispensable for axon guidance of sensory neurons in the mouse dorsal root ganglia. *Front Mol Neurosci.* 5: 67. 2012.